UNIVERSITI TEKNOLOGI MARA

MULTILEVEL THRESHOLDING FUZZY C-MEANS (MTFCM) HYBRID METHOD FOR OSTEOSARCOMA NECROSIS EXTRACTION IN MAGNETIC RESONANCE IMAGING

MOHAMAD HAIZAN BIN OTHMAN

MSc

June 2026

UNIVERSITI TEKNOLOGI MARA

MULTILEVEL THRESHOLDING FUZZY C-MEANS (MTFCM) HYBRID METHOD FOR OSTEOSARCOMA NECROSIS EXTRACTION IN MAGNETIC RESONANCE IMAGING

MOHAMAD HAIZAN BIN OTHMAN

Thesis submitted in fulfilment
of the requirements for the degree of
Master of Science
(Electrical Engineering)

Faculty of Electrical Engineering

June 2026

CONFIRMATION BY PANEL OF EXAMINERS

I certify that a Panel of Examiners has met on 18 November 2025 to conduct the final examination of Mohamad Haizan Bin Othman on his Master of Science thesis entitled "Multilevel Thresholding Fuzzy C-means (MTFCM) hybrid method for Osteosarcoma necrosis extraction in Magnetic Resonance Imaging" in accordance with Universiti Teknologi MARA Act 1976 (Akta173). The Panel of Examiner recommends that the student be awarded the relevant degree. The Panel of Examiners was as follows:

Mohamad Fahmi Hussin @ Mohamad
Associate Professor
Faculty of Electrical Engineering
Universiti Teknologi MARA
(Chairman)

Adi Izhar Che Ani
Senior Lecturer
Faculty of Electrical Engineering
Universiti Teknologi MARA
(Internal Examiner)

Fathinul Syahir Ahmad Sa'ad
Associate Professor
Faculty of Engineering & Technology
Electric
University Malaysia Perlis (UniMAP)
(External Examiner)

PROFESSOR DR HJH ZURAEDA IBRAHIM
Dean
Institute of Postgraduate Studies
Universiti Teknologi MARA
Date: 8 June 2026

AUTHOR'S DECLARATION

I declare that the work in this thesis was carried out in accordance with the regulations of Universiti Teknologi MARA. It is original and is the results of my own work, unless otherwise indicated or acknowledged as referenced work. This thesis has not been submitted to any other academic institution or non-academic institution for any degree or qualification.

I, hereby, acknowledge that I have been supplied with the Academic Rules and Regulations for Postgraduate, Universiti Teknologi MARA, regulating the conduct of my study and research.

Name of Student	:	Mohamad Haizan Bin Othman
Student ID. No.	:	2021613816
Programme	:	Master of Science (Electrical Engineering)–CEE750
Faculty	:	Electrical Engineering
Thesis Title	:	Multilevel thresholding fuzzy c-means (MTFCM) hybrid method for Osteosarcoma necrosis extraction in Magnetic Resonance Imaging
Signature of Student	:	……..
Date	:	June 2026

ABSTRACT

Osteosarcoma (OS) is a malignant bone tumor primarily affecting adolescents and young adults. Tumor necrosis, indicative of dead tumor cells, plays a critical role in determining prognosis and guiding treatment strategies. MRI is a vital imaging tool for evaluating necrosis due to its high resolution and ability to distinguish soft tissue details. Manual interpretation of MRI images is labor-intensive, subjective, and time-consuming, requiring radiologists to compare multiple sequences such as T1, T2, and T1 GADO. Intensity inhomogeneity refers to uneven signal intensity distribution in MRI images, which produces ambiguous boundaries and can adversely affect image interpretation during diagnosis. Digital image processing offers an alternative approach to assist manual interpretation. Traditional image processing algorithms, such as Fuzzy C-Means (FCM) and Multilevel Thresholding (MT), are widely used but come with specific limitations. FCM is effective in clustering regions based on intensity but struggles with overlapping intensities and computational demands, while MT offers efficient segmentation but lacks precision in handling complex tissue boundaries. In this study, two methods are proposed: the Adaptive Disk Structure Element Morphological (ADSEM) method for correcting intensity inhomogeneity and extracting fat regions, and the integrated Multilevel Thresholding Fuzzy C-Means (MTFCM) method for necrosis extraction using T1, T2, and T1 GADO sequences. The ADSEM method compensates for intensity variations in the T1 sequence and enables subsequent fat suppression in T2. The MTFCM method combines the strengths of MT and FCM to improve segmentation accuracy in regions with overlapping intensities. Total number of data includes 223 MRI slices. Validation was performed across multiple MRI slices, where the method was assessed consistently against radiologist-annotated ground truth. The ADSEM method achieved an accuracy of 89.73%, precision of 87.56%, recall of 70.76%, F1 score of 77.35%, and a Dice Similarity Coefficient (DSC) of 85.94% in fat extraction, while MTFCM delivered enhanced results in necrosis extraction with an accuracy of 99.03%, precision of 85.62%, recall of 62.30%, F1 score of 71.57%, and a Pearson correlation of 91.51% with the radiologists' ground truth. In addition, boxplot analysis demonstrates a relatively narrow data range with concentrated distributions, indicating stable performance and consistent alignment with the radiologists' ground truth across the evaluated MRI slices.

ACKNOWLEDGEMENT

First and foremost, I wish to express my deepest gratitude to God for granting me the opportunity to pursue my MSc and for guiding me through this long and challenging journey to its successful completion. My heartfelt thanks go to my supervisors, Dr. Belinda Chong Chiew Meng as the main supervisor, Prof Madya Ir Dr. Nor Salwa Binti Damanhuri, and Prof Madya Dr. Mohd Ezane bin Aziz.

I am also grateful to the Ministry of Education Malaysia for the Fundamental Research Funding Grant (FRGS/1/2021/TK0/UITM/02/39), Universiti Teknologi MARA, Cawangan Pulau Pinang, and Hospital USM in Kelantan for providing the necessary research facilities to conduct this study. Special thanks to my colleagues and friends for their invaluable assistance and support throughout this project.

Lastly, I dedicate this thesis to my father, my mother and my wife for their vision and determination in educating me. Alhamdulillah.

TABLE OF CONTENTS

LIST OF TABLES

LIST OF FIGURES

LIST OF SYMBOLS

Symbols

Fβ	Variant of F1 Score
r	Pearson correlation coefficient measures the linear correlation between predicted and ground truth necrotic area

LIST OF ABBREVIATIONS

Abbreviations

2D	Two-Dimensional
ADSEM	Adaptive Disk Structure Element Morphological
AFCM	Adaptive FCM
ATRIH_Otsu	Adaptive Trapezoid Region Intercept Histogram-based Otsu
BCFCM	Bias-Compensated FCM
BCEFCM	Bias-Correction Embedded FCMs
BRATS	Brain Tumor Segmentation
CNNs	Convolutional Neural Networks
CT	Computed Tomography
CIBERSORT	Cell Type Identification By Estimating Relative Subsets Of RNA Transcripts
DSC	Dice Similarity Coefficient
EM	Expectation-Maximization
FCM	Fuzzy C-Means
FCM_SICM	FCMs With Spatial Intensity Constraint Membership
FN	False Negative
FODPSO	Fractional Order Darwinian Particle Swarm Optimization
FP	False Positive
GVF	Gradient Vector Flow
GINC	Global Inhomogeneous Intensity Clustering

IoU	Intersection Over Union
IQR	Narrower Interquartile Range
IRGs	Immune-Related Genes
LASSO	Least Absolute Shrinkage And Selection Operator
MLOT	Multi-level Otsu Thresholding
MRI	Magnetic Resonance Imaging
MT	Multi-level Thresholding
MTFCM	Multi-Level Thresholding Fuzzy C-Means
NMR	Nuclear Magnetic Resonance
N4ITK	N4Insight Segmentation and Registration Toolkit
OS	Osteosarcoma
OLoG	Optimized Laplacian of Gaussian
PFLSCM	Patch-Based Fuzzy Local Similarity C-Means
ROI	Region of Interest
RSF	Region-Scalable Fitting
SE	Structural Element
ssGSEA	Single-Sample Gene Set Enrichment Analysis
SEER	Surveillance, Epidemiology, and End Results
ST-AL	Sooty Tern Ant Lion Optimization
SLICs+MTh	Simple Linear Iterative Clustering Supervoxels and Otsu Multilevel Thresholding
SMA	Slime Mould Algorithm

T1 Gado sequence	T1 With Gadolinium Contrast
T1 Sequence	Longitudinal Relaxation Time
T2 Sequence	Transverse Relaxation Time
TN	True Negative
TP	True Positive
VHPR	Very Hyperintense

CHAPTER 1
INTRODUCTION

1.1 Research Background: Osteosarcoma

Osteosarcoma (OS) is a mesenchymal-derived, osteoid-producing tumor and represents the most common primary malignancy of bone in children and adolescents. This high-grade tumor can be fatal. Over the past decade, the incidence of bone cancer has increased by 0.3 percent per year, as reported by the National Cancer Institute's SEER (Surveillance, Epidemiology, and End Results) program [1,2]. OS is more prevalent in males than females. In Malaysia, the Malaysia National Cancer Registry report indicates that the lifetime risk of males developing cancer is 1 in 10, while the risk among females is 1 in 91 [3]. Sarcomas are rare, constituting only 1% of all malignancies. However, they are the second most common type of solid tumor in children. Despite advances in treatment, the 5-year survival rate shover around 60%, even with combination therapies [4,5].

In Malaysia, approximately 3% of children, or about 800 annually, are diagnosed with OS [6]. The World Health Organization classifies OS into three main categories which are central, intramedullary, and surface tumors. Central OS, the most common type, affects the central part of the bone, accounting for 80% of all cases. Intramedullary tumors occur within the bone marrow, while surface tumors develop on the outer surface of the bone [7].

Figure 1.1 shows the most common site for OS. The anatomical distribution of OS reveals that the lower body is more vulnerable than the upper body [8], with the most common sites being around the knee and the pelvis. Although OS can develop in any bone in the body, these areas are particularly susceptible [9].

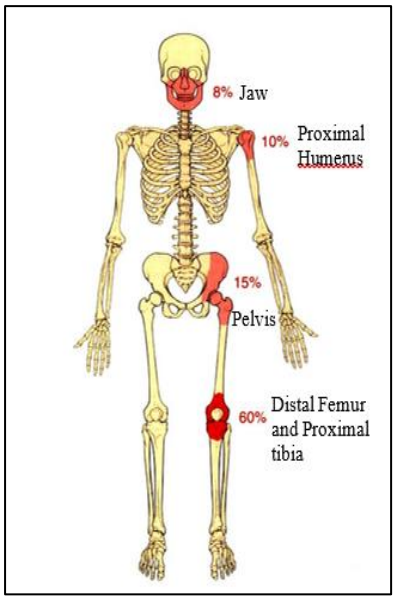

Figure 1.1 Most Common Site of OS [10]

Specifically, 18% of OS cases are found in the upper body (8% in the jaw and 10% in the proximal humerus), whereas the lower body accounts for 75% of cases (15% in the pelvis and 60% in the distal femur and proximal tibia). The remaining 7% are distributed across other bones, including the skull, ribs, lower arm, hand, spine, and sternum [11].

Long bones are rigid and dense structures that offer strength, support, and mobility. Unfortunately, the risk of OS in long bones, particularly in the lower body, is higher compared to other parts of the skeleton. This increased vulnerability is attributed to the size and activity level of these bones, as they bear significant weight and undergo constant stress, especially during growth phases. Interestingly, OS frequently affects the femur and tibia, which are the primary long bones in the lower body. Long bones contain yellow and red bone marrow, the latter of which is responsible for blood cell production [7]. OS primarily affects the metaphysis of long bones, accounting for approximately 90% of cases. The diaphysis is involved in 8–10% of cases, while the epiphysis is affected in only about 1%. These proportions reflect the tumor's preference for areas of rapid bone growth [10]. Figure 1.2 (a) and Figure 1.2 (b) shows the example of a long bone which are femur and tibia.

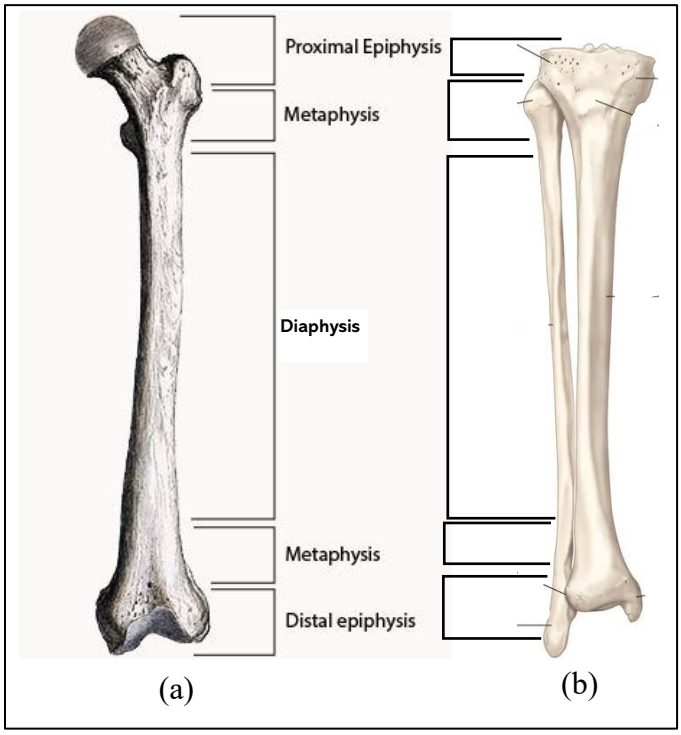

Figure 1.2 (a) Femur [12] (b) Tibia [10]

1.2 Osteosarcoma Treatment Strategies and Management

The standard treatment for OS patients involves a combination of surgery, six cycles of chemotherapy, and two MRI scans [13]. Neoadjuvant chemotherapy plays a critical role in improving surgical outcomes and overall survival by reducing tumor burden before surgery, increasing the chances of achieving clear margins during resection, and serving as a prognostic indicator based on the tumor's initial response to therapy. Following surgery, adjuvant chemotherapy is administered to eliminate remaining cancer cells that were not removed during surgery, targeting microscopic tumor cells that may have spread to other body parts, thereby reducing the risk of metastasis and recurrence. The effectiveness of adjuvant chemotherapy depends on how well the tumor responded to neoadjuvant therapy, with regimens often tailored accordingly. Patients who respond well to neoadjuvant chemotherapy, showing significant tumor necrosis, tend to have higher survival rates compared to poor responders.

Chemotherapeutic agents target rapidly dividing cancer cells, leading to their death and inducing necrosis within the tumor. Necrotic is the premature death of cells and tissues caused by conditions that disrupt their ability to maintain homeostasis. Necrosis can arise from various mechanisms. One primary cause is ischemia, where

reduced blood flow to the tumor area leads to cell death due to a lack of oxygen and essential nutrients. This deprivation causes tumor cells to die and form necrotic tissue. Tumors can trigger significant inflammatory reactions within the body, leading to cell damage and death. The inflammatory environment around the tumor can exacerbate cell death, contributing to necrotic regions [7].

Necrosis is a critical indicator of chemotherapy effectiveness, as higher levels of necrosis often correlate with better treatment responses. These mechanisms are crucial for developing targeted therapies and improving patient outcomes in OS [14]. Evaluating necrosis helps in assessing the effectiveness of treatment and predicting patient outcomes.

1.3 The Role of Imaging

OS diagnosis employs various imaging modalities, including X-rays, Computed Tomography (CT) scans, and Magnetic Resonance Imaging (MRI). X-rays are commonly used for initial detection, focusing on structural bone changes, but they lack the detail needed to assess soft tissues. Although CT scans provide more detailed imaging than X-rays and are valuable for evaluating bones and detecting lung metastases, they do not deliver adequate soft tissue contrast. MRI, with its superior soft tissue contrast, remains the preferred method for evaluating both bone and surrounding tissues, offering a comprehensive assessment of tumor extent and spread.

MRI stands out as the best modality for assessing soft tissue components, clearly visualizing surrounding tissues, vessels, and nerves, and the intramedullary extension of the tumor. This comprehensive soft tissue visualization is essential for planning safe and effective surgery. MRI scans cover the entire affected bone and neighboring joints to avoid missing skip lesions, which are intramedullary tumor nodules that do not directly contact the primary lesion. This level of detail and accuracy makes MRI superior to other imaging techniques in managing OS.

Serial MRI scans are valuable for monitoring the tumor's response to chemotherapy, with necrosis serving as a key indicator of treatment effectiveness. By comparing pre and post-treatment images, radiologists can assess the extent of tumor necrosis, which is crucial for evaluating the success of chemotherapy and guiding further treatment decisions.

MRI images can be acquired in three anatomical planes which are sagittal, axial, and coronal. Figure 1.3 illustrates the three anatomical planes of human body from MRI.

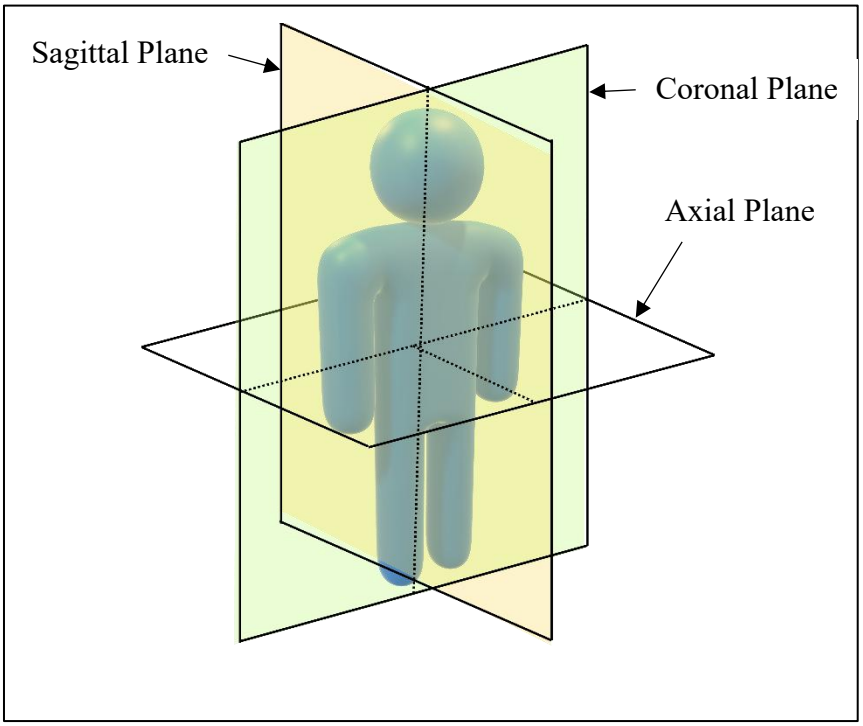

Figure 1.3 Anatomical Plane of Human Body

The sagittal plane divides the body into left and right sections, providing a side view of structures. The axial (transverse) plane divides the body into upper and lower sections, offering a cross-sectional view that is useful for assessing the spread and depth of tumors. The coronal plane divides the body into front and back sections, which is beneficial for viewing the anterior and posterior aspects of structures. These three anatomical planes allow for a comprehensive evaluation of the tumor and surrounding tissues from multiple perspectives, ensuring a detailed and accurate assessment crucial for effective treatment planning.

Besides, MRI imaging technique uses multiple sequences to visualize different aspects of tissues. In diagnosing OS, the most frequently used sequences are Longitudinal Relaxation Time (T1 sequence), Transverse Relaxation Time (T2 sequence), and T1 with gadolinium contrast (T1 GADO sequence). T1 sequences are produced based on the recovery of longitudinal magnetization. They provide high-resolution images that depict anatomical detail, showing fat as bright and water as dark. T2 sequence images are based on the decay of transverse magnetization. These images are excellent for highlighting fluid and edema, showing water as bright, making them useful for detecting abnormalities such as inflammation or tumors. Both sequences are

critical in the assessment of OS, with T1 sequence providing detailed structural information and T2 highlighting pathological changes.

Gadolinium is a contrast agent used in MRI to enhance the visibility of certain tissues. When injected, gadolinium highlights lesions and other abnormalities by making them appear differently on the images. Specifically, in T1 sequence images with gadolinium (T1 GADO sequence), this agent makes necrotic areas within tumors appear hypo-intense, or darker, compared to the surrounding enhanced tissues. This contrast helps in accurately assessing the extent and nature of tumors, improving the detection of various diseases and the precision of diagnostic evaluations. The variability introduced by gadolinium-enhanced imaging is crucial for detailed and accurate tumor assessment.

Interpreting MRI sequences is critical for diagnosing OS. This is because each MRI sequence offers distinct information about tissue characteristics. Figure 1.4 shows the different contrast and brightness of MRI sequences in the axial plane. Each sequence provides unique information regarding tissue characteristics.

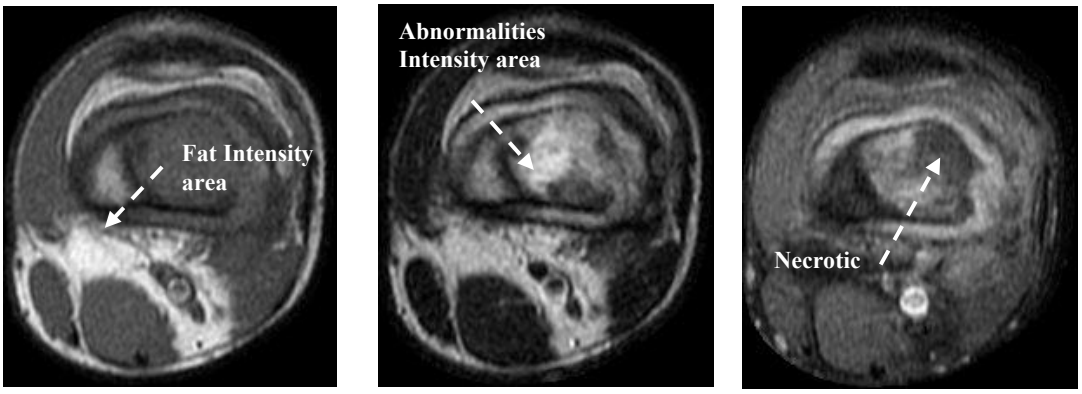

Figure 1.4 (a) T1 Sequence (b) T2 Sequence (c) T1 GADO Sequence

Figure 1.4 (a) displays the T1 sequence, where the high-intensity bright region corresponds to fat. Figure 1.4 (b) illustrates the T2 sequence, highlighting the bright, high-intensity areas that represent abnormalities. Lastly, Figure 1.4 (c) shows the T1 GADO sequence, where the low-intensity dark regions indicate necrotic areas within the abnormal region. Integrating these sequences helps to differentiate between normal tissues, pathological areas, and regions affected by necrosis, providing valuable insight into the extent of tumor involvement and response to treatment.

1.4 MRI Image Segmentation

With advancements in image processing technology, medical images can now be automatically segmented. Medical image segmentation is a vital aspect of clinical practice, enhancing the accuracy of diagnosis, treatment planning, and disease monitoring [15][16][17][18]. By facilitating the precise identification and analysis of medical conditions, these techniques significantly improve radiologists' diagnostic capabilities [19]. These techniques encompass noise reduction, image segmentation, feature extraction, and image enhancement. Noise reduction methods, such as median filtering and Gaussian smoothing, enhance image clarity by eliminating artifacts that can obscure critical diagnostic details. Image segmentation techniques, including thresholding, clustering methods like Fuzzy C-Means (FCMs), and morphological operations, extracting regions of interest, enabling focused examination of specific anatomical structures or abnormalities. Feature extraction algorithms emphasize key image features, such as edges and regions, facilitating the detection and analysis of tumors or lesions.

1.5 Problem Statement

As explained in Section 1.3, manual methods for analyzing MRI images, performed by radiologists, are inherently time-consuming and subjective. Radiologists must integrate multiple MRI sequences, including T1, T2, and T1 GADO sequences, along with data from three planes (sagittal, axial, and coronal), to evaluate necrosis, assess treatment effectiveness, and predict patient outcomes. This volumetric data requires significant effort, making the process labour-intensive and hard to reproduce [9].

Another challenge is related to hardware limitations in MRI imaging, specifically inhomogeneity. This phenomenon refers to variations in image intensity caused by non-uniform magnetic fields from the MRI machine or patient-specific factors such as edema. These intensity inconsistencies distort the scanned area, blur tissue boundaries, and complicate accurate interpretation of MRI images. These variations blur tissue boundaries, complicating the segmentation process and hindering precise analysis of fat and muscle regions, particularly in OS cases.

MR images have been widely used in numerous research and clinical applications. However, MRI segmentation remains a complex and challenging task due to inherent limitations such as image acquisition noise, low contrast between adjacent tissues, and the partial volume effect, where multiple tissue signals are blended into a single pixel due to limited resolution [10]. These challenges complicate the identification of clear boundaries, making accurate region segmentation more difficult.

Traditional image segmentation methods like FCM and Multilevel Thresholding (MT) have been commonly applied to address these difficulties mentioned. FCM is particularly useful for clustering data with overlapping intensities, making it a good choice for medical images where tissue boundaries are often ambiguous. However, FCM is sensitive to noise and computationally intensive, which reduces its efficiency and reliability in real-world clinical applications [12]. Additionally, FCM often fails to distinguish between tissues with closely similar signal intensities, especially in necrotic and viable regions that appear visually alike.

MT, on the other hand, provides a simpler and more intuitive segmentation approach, but it lacks robustness against noise and struggles with detecting fine boundaries between tissues, particularly in complex anatomical structures [20]. These limitations underscore the need for an improved method that can effectively suppress noise while preserving detailed boundary information for more reliable necrosis segmentation in MR images.

1.6 Research Objectives

The primary goal of this study is to develop techniques for extracting tumor necrosis in long leg bones of OS patients using MRI images. This goal will be achieved through the following objectives:

1. To extract fat region on T1 sequence and suppress fat on T2 sequence by using Adaptive Disk Structural Element Morphological (ADSEM) Method.
2. To develop a hybrid Multilevel Thresholding Fuzzy C-Means (MTFCM) method in extracting Osteosarcoma necrosis.
3. To evaluate and compare the performance of the proposed hybrid MTFCM method with existing FCM method.

1.7 Scope And Limitations of The Study

This research is focusing on developing a technique to extract tumor necrosis for OS patient in the long leg bone namely femur and tibia from MRI images. The MRI images used in this study are greyscale and is collected from Hospital University Sains Malaysia (HUSM), Kubang Kerian, Kelantan. The selection of MRI sequences focuses on T1, T2, and T1 GADO, as these are commonly used in diagnosis, offering distinct contrasts that are essential for differentiating normal tissues, tumor regions, and necrosis. T1 sequence helps visualize fat and anatomical structures, T2 sequence emphasizes abnormalities, and T1 GADO sequence highlights areas as necrosis. This study focuses on axial plane images. These images capture cross-sectional slices from the top to the bottom of the patient, providing a detailed view of both bone and soft tissue structures. The axial plane was selected because it offers comprehensive coverage of the femur and tibia in cross-section, which is crucial for accurately visualizing tumor boundaries and assessing the extent of necrosis. The proposed technique is developed and tested in MATLAB version R2019B for the analysis.

1.8 Significance Of Study

This study integrates T1, T2, and T1 GADO sequences to address imaging limitations by utilizing their complementary strengths. This study contributed a hybrid framework, which combine the Adaptive Disk Structure Element Morphological (ADSEM) method with the Multilevel Thresholding Fuzzy C-Means (MTFCM) technique into a single, unified processing pipeline for osteosarcoma necrosis extraction. This hybrid approach resolves intensity inhomogeneity issues, improves necrosis extraction accuracy, ensures consistent results, and increases computational efficiency. The proposed hybrid method explicitly links fat correction, suppression, and necrosis extraction across multiple MRI sequences. The development of tumor necrosis extraction techniques in this study enhances medical diagnosis by enabling the automatic detection and extraction of necrotic regions in MRI images. Accurate identification of necrotic areas is critical for clinicians, as it aids in assessing tumor response to chemotherapy and planning treatment for OS patients. This study introduces a novel computer-aided diagnosis approach based on a hybrid strategy specifically

designed for osteosarcoma necrosis assessment, which has the potential to reduce measurement variability and hospital costs, ultimately improving patient outcomes.

1.9 Thesis Outline

This thesis is organized into five chapters.

Chapter 1 introduces this work, providing an overview of OS, emphasizing its prevalence and the challenges in monitoring treatment. It outlines the problem, objectives, and scope of the study.

Chapter 2 presents a comprehensive review of the relevant literature, exploring existing techniques for MRI image analysis and their applications in medical imaging.

Chapter 3 discusses the methodology, detailing the data collection process and the development of algorithms for fat and necrosis extraction.

Chapter 4 focuses on the experimental results, analyzing the performance of the proposed methods, comparing them with traditional approaches, and discussing their clinical implications.

Chapter 5 concludes the thesis by summarizing the findings and proposing future research directions to enhance MRI analysis in OS diagnosis and treatment evaluation.

CHAPTER 2
LITERATURE REVIEW

2.1 Overview of OS Studies

OS is a type of cancer that originates in the bones. Initially, the cancer cells resemble normal bone cells, but they eventually form tumors that produce immature, abnormal, and diseased bone. This type of cancer is most frequently diagnosed in teenagers, with the average age being 15 years old. A sarcoma is a cancer that develops in connective tissues such as bone, cartilage, or muscle, while "osteo" specifically refers to bones. OS typically affects the long bones of the arms and legs, particularly near the ends of these bones (themetaphyses) and around the knee area, which undergoes the fastest growth during adolescence.

The current OS treatment consists of a combination of systemic chemotherapy and broad surgical resection. The progress of destructive systemic chemotherapies has increased the survival rate. Neoadjuvant chemotherapy is a type of treatment used to shrink tumors. One of the most important predictors of disease outcome is the percent of necrosis following neoadjuvant chemotherapy [4]. Based on both histopathologic and imaging aspects, radiological imaging MRI is often used to diagnose the patients' survival rate [21].

The medical team will evaluate the response of tumor necrosis to chemotherapy. Based on the extent of tumor necrosis, a good prognosis is associated with high levels of necrosis, indicating that the treatment is effectively destroying cancer cells. Conversely, a poor prognosis is linked to low levels of necrosis, suggesting that the chemotherapy is not as effective. The level of necrosis is crucial in determining the survival rate of a patient, as higher necrosis rates are generally correlated with better treatment outcomes and longer survival. This chapter will explain various methods to assess necrosis, discuss existing research on automatic tumor detection, and highlight the significance of accurately assessing tumor necrosis for optimizing treatment strategies.

2.2 Importance of Necrosis Assessment in OS

Necrosis extraction is a crucial aspect of OS diagnosis and treatment evaluation. The presence and extent of necrotic tissue within a tumor provide significant insights into the tumor's aggressiveness, the effectiveness of treatment, and the overall prognosis for the patient. Accurately identifying necrosis is pivotal for several reasons: it allows clinicians to assess the histopathological response to chemotherapy, guides decisions on further treatment planning, and serves as a prognostic indicator for patient outcomes. A higher percentage of tumor necrosis after neoadjuvant chemotherapy is generally associated with a better prognosis, whereas poor necrotic response often indicates resistance to treatment and a higher likelihood of recurrence or metastasis [22].

The degree of tumor necrosis following neoadjuvant chemotherapy is one of the most important prognostic indicators in OS. High levels of necrosis typically correlate with a better response to treatment and a more favorable prognosis. Conversely, low levels of necrosis may indicate that the tumor is less responsive to the current therapeutic regimen, suggesting a need for alternative treatment strategies [23].

Necrosis assessment aids in planning subsequent treatment steps. For instance, if significant necrosis is detected post-chemotherapy, it may justify proceeding with aggressive surgical resection, knowing that the tumor has responded well to the treatment [24]. In contrast, minimal necrosis might prompt a re-evaluation of the chemotherapy protocol before surgical intervention.

Pathologists and radiologists use specific grading systems to evaluate necrosis, primarily based on histological analysis of tumor tissue samples. Necrosis rate and the percentages of necrosis must be investigated and determined by radiologists. Prior to and after neoadjuvant chemotherapy.

Assessing the extent of necrosis following neoadjuvant chemotherapy is crucial because it provides insights into the treatment's effectiveness. The Huvos grading system is one of the most widely used frameworks for evaluating the response of OS to chemotherapy [22]. Table 2.1 shows the Huvos grading system.

Table 2.1
Huvoc Grading System

Grade	Necrosis Rate, %	Response	Classification
I	0-49	Poor	Little or no necrosis
II	50-89	Poor	Areas of necrosis with viable tumor
III	90-99	Good	Scattered foci of viable tumor
IV	100	Good	No viable tumor

The grading system for necrosis in OS categorizes the extent of necrosis observed in response to chemotherapy into four distinct grades, each corresponding to specific necrosis rates and histologic classifications.

Grade I represent a necrosis rate of 0-49%. This grade is considered a poor response to chemotherapy, indicating little or no necrosis within the tumor. The histologic classification reflects the limited effectiveness of the treatment, with substantial viable tumor remaining.

Grade II is assigned to a necrosis rate of 50-89%. This also indicates a poor response to chemotherapy, characterized by partial necrosis. Although some areas of the tumor show the effects of treatment, there are still significant regions of viable cancer cells, indicating a less effective chemotherapy response.

Grade III corresponds to a necrosis rate of 90-99%. This grade indicates a good response to chemotherapy, with most of the tumor cells affected by the treatment. Although there is still some viable tumor cells present, the extent of necrosis is significant, suggesting a more successful therapeutic outcome.

Grade IV represents a necrosis rate of 100%. This is considered a very good response to chemotherapy, indicating complete necrosis of the tumor cells. There are no viable tumor cells remaining, reflecting the highest level of treatment effectiveness and the best prognostic outcome for the patient.

These grades help in stratifying patients into different prognostic categories, guiding subsequent treatment decisions. Assessing the extent of necrosis following neoadjuvant chemotherapy is crucial because it provides insights into the treatment's

effectiveness. Patients showing high rates of tumor necrosis generally have better prognoses and higher survival rates compared to those with lower necrosis rates.

2.3 Necrosis and Medical Imaging

MRI imaging is a widely used and essential tool in the medical field, particularly for investigating a range of diseases, including the diagnosis and assessment of OS. It provides detailed images of both bone and soft tissue, making it highly effective for evaluating tumor size, location, and the extent of disease progression. Its ability to produce high-resolution images without ionizing radiation makes it particularly suitable for repeated patient monitoring. In OS diagnosis, MRI is used to assess the extent of the disease, plan treatment, and monitor the response to therapy, offering superior contrast resolution to detect soft tissue abnormalities.

MRI operates based on the principles of nuclear magnetic resonance (NMR). When a patient is placed inside the MRI machine, a strong magnetic field aligns the protons in the body's water molecules. Radio frequency pulses are then applied to disrupt this alignment, and as the protons realign with the magnetic field, they release energy. This energy is detected and processed by a computer to create detailed cross-sectional images. MRI's role in the management of OS includes diagnosis, treatment planning, and follow-up.

Regular assessment of necrosis through imaging allows clinicians to monitor the effectiveness of ongoing treatment. This dynamic monitoring helps in making timely adjustments to the treatment plan, thereby improving the chances of success.

As explained in section 1.3, interpreting MRI medical images requires radiologists to assess and compare these sequences, as each highlights different tissue properties. Radiologists must correlate T1, T2, and T1 GADO sequences to accurately identify and extract necrotic regions in OS. Each sequence provides unique and complementary information about the tissue characteristics within the tumor, making their combined use essential for precise diagnosis [25]. For example, T1 sequences typically show anatomical structures and fat as high-intensity regions, whereas T2 sequences highlight abnormalities such as tumors, which appear brighter. The T1 GADO sequence, enhanced with gadolinium contrast, helps in identifying areas with compromised blood supply, which is critical for locating necrotic tissue. By analyzing and comparing these different sequences, radiologists can form a comprehensive picture

of the tumor's behaviour and progression, leading to a more accurate diagnosis and effective treatment planning. Table 2.2 shows the difference in appearance in different sequences which are T1 sequence, T2 sequence and T1 GADO sequence [26].

Table 2.2
Tissue Appearance in Different Sequences

Tissue	T1 sequence	T2 sequence	T1 GADO sequence
Fat	Bright	Bright	Dark
Muscle	Dark Gray	Dark Gray	Light Gray
Cortical	Dark	Dark	Dark
Necrotic area	Dark Gray	Bright	Dark

Referring to Table 2.2, T1 sequence images are primarily used for assessing anatomical structures. In this sequence, fat appears bright due to its high signal intensity, making it easily distinguishable from other tissues. Muscle shows up as dark gray, while cortical bone appears dark because of its low signal intensity. Necrotic areas also appear dark, as they have reduced vascular supply and low signal. This sequence is useful for evaluating bone and soft tissues, though necrotic regions may not be as prominent due to their low signal intensity.

T2 sequence images are particularly effective for highlighting fluid-rich tissues. In this sequence, necrotic areas and edema appear bright due to their high fluid content and signal intensity. Fat can also appear bright, but it is typically less intense than fluid, helping distinguish necrosis from fat. Muscle appears as dark gray, and cortical bone remains dark. The brightness of necrotic regions in T2 sequence helps in differentiating them from other structures, but additional techniques may be needed to clearly distinguish necrosis from fat when both appear bright.

In T1 GADO sequences, a gadolinium-based contrast agent is administered, which enhances the visibility of certain tissues. After contrast, fat appears dark, muscle shows up as light gray, and necrotic areas remain dark because necrotic tissue, due to poor blood supply, does not take up the gadolinium. This sequence is valuable for distinguishing viable from non-viable tissue, as the lack of contrast enhancement in necrotic areas helps radiologists assess tumor response and plan surgical interventions. Gadolinium enhances viable, vascularized tissues, making necrotic regions stand out as

hypo-intense areas, correlating with the high signal intensity seen in T2 sequence for necrotic areas, thus providing clear delineation. Figure 2.1 shows the axial plane for the MRI images.

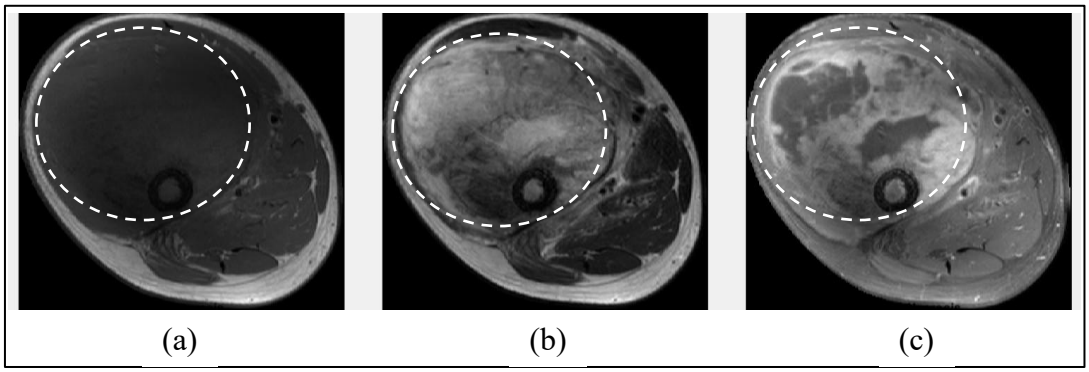

Figure 2.1 (a) T1 Sequence (b) T2 Sequence (c) T1 GADO Sequence

Figure 2.1 (a) shows a T1 sequence image where normal fatty tissue appears bright due to consistent signal intensity. The dotted circle highlights the abnormal region, which exhibits a low signal intensity, indicating a reduction or loss of normal fatty tissue in the bone marrow. The dotted circle in Figure 2.1 (a), (b), and (c) marks the abnormal region across all sequences, aiding in the identification and analysis of abnormalities. Figure 2.1 (b) shows a T2 sequence image, where muscle regions appear darker compared to T1 sequences. However, the abnormal region highlighted by the dotted circle shows higher signal intensity, indicating increased water content. Figure 2.1 (c) shows a T1 GADO sequence, which is sensitive to water signals. In this sequence, fat tissue signals are reduced, and water-rich areas appear bright [7]. The dotted circle highlights the abnormal region, where necrotic tissue exhibits low signal intensity, and abnormal fluid presents higher signal intensity. These comparisons help differentiate tissues based on their signal properties.

In clinical practice, radiologists assess necrotic regions by correlating information from multiple MRI sequences. The T1 sequence provides an anatomical baseline, helping to identify fat and tissue structure. The T2 sequence highlights regions with high signal intensity, which may indicate fluid accumulation and necrosis. Radiologists cross-reference bright areas in the T2 sequence with the T1 sequence to distinguish necrotic tissue from fat. This comprehensive analysis ensures accurate identification of necrotic regions for effective diagnosis and treatment planning.

Overlaying and comparing these sequences allows radiologists to precisely identify and extract necrotic regions. The dark areas in T1 GADO sequence that correspond to bright regions in T2 sequence and low intensity in T1 sequence confirm

the presence of necrosis. The correlation between MRI sequences allows for a more accurate and comprehensive assessment of the tumor's necrotic regions, thereby supporting diagnosis, treatment planning, and monitoring treatment effectiveness.

Table 2.3 provides a representation of MRI image interpretation, demonstrating the appearance of viable tumor as dark gray in T1 sequence, intense on T2 sequence and light gray in T1 GADO sequence. For necrotic region, it appeared as dark gray in T1 sequence, bright in T2 sequence and dark in T1 GADO sequence [26]. For edema, it appeared as dark gray in T1 sequence, intense on T2 sequence and light gray on T1 GADO sequence.

Table 2.3
Appearance of MRI Sequences T1, T2 and T1 GADO

Tissue type	T1 sequence	T2 sequence	T1 GADO sequence
Edema	Dark gray	Intense	Light gray
Necrotic	Dark gray	Bright	Dark
Viable tumor	Dark gray	Intense	Light gray

Manual necrosis assessment by radiologists, though expert-driven, is prone to subjectivity and variability. Automated algorithms and advanced imaging techniques improve necrosis detection by reducing human error, ensuring consistent and reliable diagnoses, and aiding in treatment decisions [21]. Accurate necrosis extraction enables treatments tailored to each patient's condition, optimizing therapy effectiveness while minimizing side effects [22]. By determining the extent of tumor necrosis, clinicians can adjust therapies based on the individual patient's response, aligning treatment with specific medical needs.

2.4 The Challenge of Intensity Inhomogeneity in MRI Imaging

MRI is a critical tool in the diagnosis and treatment monitoring of OS. However, despite its widespread use, MRI technology presents several challenges that researchers have addressed in recent studies. This section discussed the problems faced with MRI images in OS research and the solutions that past researchers have proposed and implemented to address these issues.

MRI utilizes powerful magnets and radio waves to generate detailed images of internal structures, but hardware limitations can introduce issues like intensity inhomogeneity, where uneven image intensity causes some regions to appear brighter or darker. This often stems from imperfections in radio-frequency coils or MRI acquisition sequences, which can obscure important features and complicate accurate analysis. Additionally, MRI inhomogeneity, due to variations in magnetic field strength, poses significant challenges by leading to signal intensity variations that blur tissue boundaries and hinder differentiation between healthy and cancerous tissues. For instance, inconsistent magnetic fields can make it difficult to delineate necrotic from viable tumor tissues. To address these issues, Lee et. al. [27] employed diffusion-weighted MRI and volumetric analysis to predict poor responders to neoadjuvant chemotherapy in OS patients. Their approach focused on improving image clarity and reducing the impact of signal variations using advanced image processing algorithms tailored to adapt to MRI inhomogeneities.

Recent study by Sangeetha Saman et. al. addresses the issue of intensity inhomogeneity in MRI images [28], which poses challenges for accurate brain tumor segmentation. To mitigate this problem, the researchers proposed a multi-stage methodology encompassing pre-processing, segmentation, and post-processing. Pre-processing involved the use of the N4 Insight Segmentation and Registration Toolkit (N4ITK) algorithm for inhomogeneity correction and anisotropic diffusion filtering for noise removal. The segmentation phase introduced an active contour model combining region-scalable fitting (RSF) energy with an optimized Laplacian of Gaussian (OLoG) energy term, designed to smooth homogeneous regions and enhance edges, thereby improving accuracy. Post-processing included morphological operations and thresholding to extract the tumor region. Evaluated on the Brain Tumor Segmentation (BRATS) and J. Cheng data sets, the method showed superior performance over manual segmentation and existing approaches, despite being sensitive to parameter settings and computationally intensive.

Feng et. al. [29] address the challenge of intensity inhomogeneities and noise in brain MR image segmentation using an improved Bias Correction Embedded FCMs (BCEFCM) model. Their method integrates bias correction and noise suppression within the FCM framework, incorporating bilateral filtering for bias smoothness and a spatial constraint term to enhance robustness against noise. This approach demonstrated superior segmentation accuracy compared to other methods, supported by higher

Jaccard similarity coefficients and Fβ scores in experimental evaluations. Despite these advancements, the model's high computational complexity and sensitivity to noise variations highlight areas for future improvement, including enhanced efficiency and broader applicability.

In another study, Feng et. al. presented a novel level set model for image segmentation that effectively addresses intensity inhomogeneities [30]. The proposed Global Inhomogeneous Intensity Clustering (GINC) model introduces an inhomogeneous intensity clustering energy, which leverages global distribution characteristics of image intensities to define the data term energy using membership functions described by the level set function. This method integrates a bias correction mechanism by estimating inhomogeneities through orthogonal primary functions. To ensure the smoothness and stability of the level set contour, the model includes a regularization term and an arc length term. Notably, the model was evaluated using various image types, including synthetic images, natural scene images from public datasets, and medical images such as cardiac X-ray and brain MRI scans. The experimental results demonstrated the model's superior performance in both bias correction and segmentation accuracy compared to existing methods, underscoring its adaptability for segmenting colorful and complex images containing multiple objects.

As explained in Section 1.5, inhomogeneity refers to the uneven distribution of intensity in an image, which can obscure critical diagnostic features and hinder accurate analysis. To address this challenge, Vishal Venkatesh et. al. [31] introduced InhomoNet, a novel deep-learning-based approach specifically designed to correct intensity inhomogeneities in brain MRI images. Their method employs advanced algorithms for image comparison and matching, enabling more accurate and reliable diagnostic results by preserving essential structural details. The study demonstrated InhomoNet's effectiveness using both simulated and real brain MRI datasets. Despite its promising performance, InhomoNet requires substantial computational resources during the training phase, which may limit its practical deployment in resource-constrained environments.

Table 2.4 summarise the used of algorithms in MRI image processing to overcome inhomogeneity:

Table 2.4
Comparison Method to Overcome Inhomogeneity

Methods	Authors	Discussion	Limitation
Diffusion-weighted MRI and volumetric analysis	Lee et. al. [27]	Improved image clarity and reduced signal variation for OS patients, focusing on necrotic and viable tumor differentiation.	Limited to specific use cases, such as OS; may not generalize to other conditions.
N4ITK algorithm and active contour model	Sangeetha Saman et. al. [28]	Combines bias correction, anisotropic filtering, and advanced segmentation techniques like OLoG for better edge detection and noise removal. Evaluated on BRATS dataset.	Sensitive to parameter tuning and computationally intensive.
BCEFCM model	Feng et. al. [29]	Extends to multispectral images with enhanced robustness to noise using spatial constraints and bias correction.	Computational complexity and sensitivity to specific noise remain issues.
Inhomogeneous intensity clustering model	Feng et. al. [30]	Introduces level set functions and bias correction for superior segmentation, applicable to multichannel and multiphase images.	Requires further optimization for noise handling and real-time processing.
InhomoNet (Deep Learning Approach)	Vishal Venkatesh et. al. [31]	Uses advanced deep learning for intensity normalization and diagnostic accuracy in MRI, preserving critical information.	High computational demand, particularly during the training phase.

In summary, recent research has focused on addressing intensity inhomogeneity in MRI images, a critical challenge in medical imaging. Various methods have been developed to mitigate the effects of inhomogeneity, enhancing image clarity and segmentation accuracy. For instance, Lee et. al. utilized diffusion-weighted MRI with volumetric analysis to reduce signal variations, improving diagnostic accuracy in OS patients. Similarly, Feng et. al. proposed an improved BCEFCM model with spatial constraints and bias correction, showing superior segmentation performance but facing challenges with computational complexity. Sangeetha Saman et. al. introduced a multi-stage approach integrating the N4ITK algorithm and active contour models to address inhomogeneity, achieving higher accuracy in tumor segmentation while remaining sensitive to parameter settings. Venkatesh et. al. developed InhomoNet, a deep-learning-based solution that preserves diagnostic data while managing intensity variations, albeit requiring significant computational power. These findings underscore the progress in tackling MRI inhomogeneity, highlighting advancements in bias correction, segmentation precision, and computational techniques, along with the ongoing need for more efficient and robust solutions.

2.5 MRI Image Segmentation Algorithm

Due to the aggressive nature of bone cancer, which can have fatal consequences, precise and thorough analysis by experts is essential. MRI provides quantitative data crucial for diagnosing OS, but the manual assessment of this data is time-consuming and subject to variability. This necessity for speed and accuracy underscores the need for automation through image segmentation. Image segmentation involves partitioning an image into distinct regions, making it easier to analyze and extract specific areas of interest, such as necrotic regions in tumors. The limitations of manual analysis have led to the development of various algorithms in previous studies aimed at extracting regions of interest (ROI) from MRI scans. These algorithms aim to enhance accuracy, efficiency, and objectivity in diagnosing and extracting the necrosis region. There are numerous algorithms utilized in image processing, each with unique strengths and applications.

The development of algorithmic solutions has been instrumental in addressing the limitations of manual necrosis assessment in OS diagnosis and treatment evaluation. In a study by He et. al. [32], the researchers aimed to enhance the prediction of chemotherapy responses in OS patients by analyzing the tumor immune microenvironment. To achieve this, they applied single-sample gene set enrichment analysis (ssGSEA) and the CIBERSORT algorithm to quantify immune cell infiltration from gene expression data. Furthermore, they employed LASSO and binary logistic regression to identify five key immune-related genes (IRGs) that formed the basis of a predictive model. While the study primarily focused on gene expression rather than direct image segmentation, its findings are relevant to improving overall diagnostic strategies by integrating biological markers with imaging data. This approach addresses the problem of subjective and inconsistent manual assessment by offering a more objective and automated method for evaluating treatment responses in osteosarcoma.

N. Tajbakhsh et. al. [14] introduced an integration of a modified entropy-based approach with an upgraded Canny technique for MRI image segmentation. This hybrid approach leveraged entropy for thresholding and the Canny technique for edge detection, yielding more accurate segmentation results. Their findings emphasized the importance of combining multiple techniques to address the limitations of traditional segmentation methods, particularly in medical imaging.

Further advancements in algorithmic solutions for necrosis assessment were explored by D. J. Ho et. al., R. Hao et. al., and H. Mzoughi et. al. [33][34][35], who investigated various integration methods to improve the efficiency and reliability of necrosis detection. These studies underscore the importance of leveraging technology to complement the capabilities of healthcare professionals, ensuring accurate and timely diagnosis, which is crucial for effective treatment planning.

2.5.1 Image Thresholding

Image thresholding is a fundamental technique in image processing used to separate objects from the background by converting grayscale images into binary images based on a selected threshold value [36]. Various thresholding approaches exist, including local, global, average, Otsu thresholding, and multilevel thresholding (MT), each differing in how threshold values are determined and applied.

Local thresholding applies different threshold values to different image regions, making it suitable for images with non-uniform illumination [37]. The threshold for each pixel is computed based on the intensity values of its local neighbourhood, as expressed in equation (1).

$$T(x,y) = \frac{1}{n}\sum_{(x',y')\in N(x,y)} I(x',y') \tag{1}$$

Where:

$T(x,y)$is the threshold value at pixel(x,y)

$N(x,y)$is the neighborhood of (x,y)

$I(x',y')$represents the intensity values of the neighborhood pixels.

(x',y')represents the coordinates of the neighboring pixels of(x,y)

n is the total number of pixels within the neighborhood $N(x,y)$

Global thresholding uses a single threshold value for the entire image, typically derived from the image intensity histogram [38]. This approach is computationally simple and effective for images with uniform lighting, but its performance degrades under uneven illumination, as shown in equation (2).

$$T = \frac{1}{MN}\sum_{x=0}^{M-1}\sum_{y=0}^{N-1} I(x,y) \tag{2}$$

Where:

T is the global threshold value

$M\ and\ N$ are the dimensions of the image

$I(x, y)$ is the intensity value of the pixel at (x, y)

Average thresholding computes the threshold as the mean intensity of all pixels [39]. While straightforward, it lacks adaptability and may perform poorly in images with significant intensity variations. The distinction between global and average thresholding lies in their flexibility, where global thresholding allows customized threshold selection, whereas average thresholding relies solely on mean intensity.

Several studies have applied thresholding in advanced segmentation tasks. Reham R. Mostafa et. al. [40] proposed a hybridized metaheuristic algorithm (ST-AL) incorporating thresholding to improve segmentation accuracy in high-dimensional datasets, achieving reduced computational time but facing potential overfitting issues. The proposed algorithm shows improved convergence and robustness compared to state-of-the-art methods, achieving mean accuracy values between 0.94 and 1.00. Similarly, A. Kamsyakawuni et. al. [41] utilized thresholding within a metaheuristic framework to solve nonlinear equation systems for image segmentation, demonstrating good accuracy and efficiency, although robustness against noise remained a limitation.

Otsu thresholding, introduced by Nobuyuki Otsu in 1979 [42], is an automatic threshold selection method that separates foreground and background by minimizing within-class variance. Its histogram-based formulation makes it suitable for MRI applications, where tissue contrast enhancement is essential for region of interest (ROI) identification. The within-class variance is defined in equation (3).

$$\sigma_w^2(T) = q_1(T)\sigma_1^2(T) + q_2(T)\sigma_2^2(T) \tag{3}$$

Where:

$\sigma_w^2(T)$is the within-class variance

$q_1(T)$ and $q_2(T)$are the probabilities of the two classes separated by threshold

T is the threshold value

$\sigma_1^2(T)$ and $\sigma_2^2(T)$ are the variances of the two classes.

Despite its effectiveness, Otsu thresholding is sensitive to noise and overlapping intensity distributions, limiting its performance in complex MRI data. Than et. al. [43] applied multi-class Otsu thresholding for MRI brain tumor segmentation, integrating

preprocessing and morphological operations to improve segmentation accuracy, achieving 95.56% accuracy on the BRATS 2015 dataset. Leyi Xiao et. al. [44] introduced the ATRIH_Otsu method to enhance noise resistance through adaptive histogram modeling, demonstrating improved segmentation performance, although noise identification challenges remained. Utsav Kumar Malviya et. al. [45] employed modified multilevel Otsu thresholding for automated brain tumor detection, showing effective tumor segmentation through enhanced threshold selection.

2.5.2 Multilevel Thresholding

MT is a widely used image segmentation technique that partitions an image into multiple distinct regions based on intensity values. It operates by analyzing the image histogram to determine optimal threshold values, which divide the intensity range into distinct intervals. Histogram analysis involves examining the distribution of pixel intensities to locate peaks and valleys, which correspond to regions of similar intensity. Pixels are then assigned to specific regions based on their intensity relative to these thresholds. This method is particularly effective for images with distinct intensity distributions, as it simplifies complex images into meaningful segments for further analysis. MT offers several advantages, including computational efficiency and simplicity, as it processes intensity histograms directly without requiring iterative calculations. It is suitable for applications where clear intensity boundaries exist between regions, such as object detection or pattern recognition. However, it may struggle with images that have overlapping intensity ranges or gradual intensity transitions, which can complicate the selection of optimal thresholds [46]. Equation (4) represents the mathematical formula for MT.

$$g(x,y) = \begin{cases} a \; if \; f(x,y) > TH_2 \\ b \; if TH_1 \leq f(x,y) \leq TH_2 \\ c \; if \; f(x,y) \leq TH_1 \end{cases} \tag{4}$$

Where:

$g(x,y)$ is Thresholded Image

TH_1 is Threshold value 1

TH_2 is Threshold value 2

A point (x,y) belongs to

a. To an object class if $f(x,y) > TH_2$

b. To another object class if $TH_1 \leq f(x,y) \leq TH_2$
c. To background if $f(x,y) \leq TH_1$

Esha Baidya Kayal et. al. [47] introduced a method called Simple Linear Iterative Clustering Supervoxels and Otsu Multilevel Thresholding (SLICs+MTh) to address challenges associated with multilevel thresholding. In this study, tibia MRI images were used as the data for segmentation. They noted that multilevel thresholding performance can be affected by tumor tissue heterogeneity, impacting segmentation accuracy in highly variable tumor regions. However, the study emphasized that multilevel thresholding plays a crucial role in non-invasive, automated methods used to evaluate how well a treatment is working. This technique has the potential to improve accuracy when analyzing medical images. The SLICs+MTh technique effectively segmented viable and nonviable tissue in OS. By combining multilevel thresholding with supervoxels, this technique enhances efficiency, automating chemotherapy response assessment. Active tumor, necrosis, and edema were segmented with satisfactory performance (JI: 62–78%, DC: 72–87%, precision: 67–87%, recall: 63–88%), with necrosis areas showing good correlation with hypointense regions in PC-T1W (DC: 74 ± 9%).

MT is a crucial process for image segmentation, significantly improving the extraction process. Wang et al.[48] proposed a modified salps warm algorithm-based MT technique to optimize image segmentation. While MT improves tumor region delineation, increasing the number of thresholds can reduce segmentation accuracy. Its advantage lies in its ability to separate regions within an image more precisely than binary thresholding, which is critical when analyzing complex histology images where tumor, necrotic, and non-tumor tissues coexist. However, optimizing threshold values is necessary to balance accuracy and computational complexity. The performance of MT directly impacts the quality of subsequent feature extraction and classification stages, playing a pivotal role in developing accurate OS classification systems. Despite the challenges, integrating sophisticated algorithms for MT represents significant progress in computer-aided diagnostic tools, enhancing their capability to assist researchers in medical image analysis.

S. Prasath et. al. [49] in their study address the challenge of effective biomedical image segmentation where traditional methods often fail due to noise and artifacts. Their approach utilizes a fractional order Darwinian particle swarm optimization

(FODPSO) combined with MT to enhance segmentation accuracy. The study specifically focuses on dental X-ray images, targeting the segmentation of cystic regions in the jaw. The primary noise type encountered in these images is solitary pixel noise caused by sampling artifacts, which complicates the accurate delineation of cyst boundaries. The performance of their method is reported to be superior in terms of segmentation quality when compared to traditional thresholding methods. However, the computational complexity and the need for optimization of multiple parameters are identified as weaknesses that could be improved in future studies by developing more efficient algorithms or incorporating machine learning techniques to automate parameter tuning.

Another study by Yuanyuan Jiang et. al. that tackled the issue of effective image segmentation, specifically addressing the challenges posed by complex image datasets [50]. They proposed a MT method based on the improved Slime Mould Algorithm (SMA) and symmetric cross-entropy, aiming to enhance segmentation accuracy. This thresholding approach helps to determine optimal thresholds that maximize the distinction between different image regions. The method demonstrated superior performance in terms of segmentation precision and computational efficiency. However, limitations include the potential for increased computational demands with highly complex images and the need for further refinement to improve robustness and applicability across diverse datasets. Future research is suggested to optimize the algorithm for better handling of more varied and intricate image data.

Another study by Deepika Koundal et. al. focuses on the effective segmentation of medical images, specifically for detecting pathological regions such as tumors and cysts, with an emphasis on dental X-rays [51]. The main challenge they address is the need for automated and accurate segmentation in noisy environments without human intervention. Their methodology incorporates a fuzzy-based multi-region thresholding approach, leveraging FCM algorithms to identify initial cluster centroids and integrating local spatial information to refine the segmentation process. This approach is particularly suited to mitigating the impact of speckle noise and other artifacts commonly found in medical images, enhancing the clarity and precision of cystic region identification. Although their technique demonstrates significant improvements in accuracy and automation, it shares computational complexity and sensitivity to initial cluster settings, suggesting opportunities for future refinement to better handle diverse datasets.

In the study by Shubham et. al. [52] ,the researchers addressed the problem of effective image segmentation for colored images by employing a MT technique using Masi entropy. The method involved applying various entropies to satellite and natural images to find optimal threshold values for segmenting the images into distinct regions. The performance of this method demonstrated improved segmentation accuracy and computational efficiency compared to traditional techniques. However, the method has weaknesses such as sensitivity to noise and dependence on the initial parameter settings.

2.5.3 Morphological

Mathematical morphology is a geometric approach to image processing, designed as a powerful tool for analyzing shapes in binary and grayscale images. Developed initially by G. Matheronin 1975 [53], mathematical morphology offers a framework for manipulating and interpreting image structures based on set theory, lattice theory, topology, and random functions. The methodology was first applied to binary images and later extended to grayscale images, providing essential techniques such as dilation, erosion, opening, and closing. These operations are fundamental for tasks such as noise removal, image enhancement, and feature extraction.

Morphological operations have been widely utilized in medical imaging, particularly for region extraction in MRI scans [54]. These operations, based on mathematical morphology, are used to process geometric structures within images and helping to accurately delineate anatomical structures and pathological regions. By effectively separating distinct regions based on their shape and intensity, mathematical morphology enhances the ability to identify and analyze specific areas of interest, such as tumors, thereby improving the precision of medical diagnoses and treatments. Despite their widespread application, previous researchers have encountered several challenges when using morphological methods for region extraction.

One major issue is the susceptibility of morphological operations to noise, which can lead to inaccurate extraction of regions. Noise in MRI images often causes false positives or negatives during the morphological processing stages. To address this challenge, Huang et. al. [55] conducted a study focusing on medical image preprocessing, where they developed an advanced noise reduction and edge enhancement algorithm. The study emphasized the effectiveness of combining median filtering to eliminate salt-and-pepper noise with morphological opening to preserve

structural features while removing small noise artifacts. This hybrid technique was tested on various medical images, including MRI scans, demonstrating its ability to significantly improve region extraction accuracy by reducing noise interference before segmentation. Their approach helped enhance the visibility of tissue boundaries, leading to more reliable results in downstream processing tasks like tumor or necrosis detection.

Another problem is the poor contrast between the ROI and surrounding tissues, which can hinder the effectiveness of morphological operations. This issue is particularly problematic in MRI scans where the contrast can vary significantly. Zhang et.al. [56] proposed an adaptive contrast enhancement method prior to applying morphological operations. Their method dynamically adjusted the contrast levels in the image to enhance the visibility of the ROI, thus improving extraction accuracy.

Morphological operations also struggle with complex anatomical structures, leading to incomplete or inaccurate extraction of regions. Traditional morphological methods are not always capable of capturing the intricacies of complex shapes. To overcome this, M. R. Canales-Fiscal et. al [57] developed a hybrid approach that integrated morphological operations with deep learning algorithms. This approach leveraged the strengths of convolutional neural networks (CNNs) to better handle complex structures while using morphological operations to refine the boundaries of the extracted regions. The MCNN method achieved an AUC of 0.94 for melanoma classification and 0.65 for glaucoma detection, matching or outperforming popular CNN architectures.

2.5.4 Fuzzy C-Means

FCM clustering algorithm is a fundamental tool in image segmentation, particularly in medical imaging, due to its ability to handle uncertain and overlapping pixel intensities. However, various studies highlight challenges and propose solutions related to specific issues such as intensity inhomogeneity, noise sensitivity, computational complexity, and boundary preservation [58]. This method minimizes the following objective function, as shown in equation (5).

$$J_m(U,V) = \sum_{i=1}^{c} \sum_{j=1}^{n} \mu_{ij}^{m} \left\| x_j - v_i \right\|^2 \tag{5}$$

Where:

$J_m(U,V)$ is the objective function to be minimized.

μ_{ij} is the membership value of pixel j to cluster i.

x_j is the feature vector of pixel j.

v_i is the centroid of cluster i.

m is the fuzziness exponent parameter, typically set to 2 in most applications.

Conventional FCM algorithms often struggle with intensity inhomogeneities caused by imperfections in MRI acquisition. M. Ahmed et. al. [59] proposed the Bias-Compensated FCM (BCFCM) algorithm to address this issue. BCFCM incorporates neighboring pixel labels to achieve piecewise-homogeneous labeling, outperforming traditional FCM and expectation-maximization (EM) methods in segmenting MRI data with intensity inconsistencies. Similarly, Balafar M.A. [60] introduced the Adaptive FCM (AFCM) algorithm, which adapts to local intensity variations by modifying the objective function. These approaches significantly enhance segmentation accuracy but require careful parameter tuning, which can be computationally expensive.

FCM clustering algorithms are susceptible to noise, which can disrupt segmentation accuracy. S. Chen et. al. [61] introduced spatial constraint variants, Fuzzy C-Means with Spatial Information 1 (FCM_S1) and Fuzzy C-Means with Spatial Information 2 (FCM_S2), to address this issue. These methods incorporate spatial context to reduce noise influence by including the spatial relationship of neighboring pixels. While these approaches enhance robustness against noise, they may still be vulnerable to outliers, which can affect the segmentation process. Wang et. al. [62] proposed residual-driven FCM methods to further improve robustness by employing residual adjustments to refine cluster centers. This refinement mitigates the impact of noise and outliers, achieving better performance in challenging environments. However, despite these advancements, computational complexity and parameter selection remain significant challenges, requiring further research to optimize these methods.

Distinguishing regions with overlapping intensities, such as necrotic and viable tumor tissues, is a significant challenge in medical image segmentation. Qingsheng Wang et. al. [63] identified this problem and proposed FCM with Spatial Intensity Constraint Membership (FCM_SICM) as a solution. This method incorporates spatial intensity constraints to enhance segmentation accuracy by addressing intensity similarities between regions. While FCM_SICM improves segmentation performance in such challenging cases, it is computationally intensive, limiting its scalability.

Similarly, M.M. Kh et. al. [64] developed an FCM-based approach that integrates edge information and local intensity to address overlapping intensity issues. This method demonstrated superior clustering performance, validated through metrics like the partition coefficient and Davies-Bouldin index. However, it is computationally expensive and sensitive to noise, which restricts its applicability in real-world scenarios.

Patch-based methods, such as Yiming Tang et. al.'s [65] Patch-based Fuzzy Local Similarity C-Means (PFLSCM), use structural similarity indices and weighted distance metrics to enhance accuracy. While these approaches are effective for precise segmentation, they encounter scalability challenges in real-time applications due to high computational demands.

2.5.5 Active Contour

Active contour models, also known as snakes is one of a popular method in image segmentation, introduced by Kass, Witkin, and Terzopoulos in 1988 [66]. These models work by initializing a curve around the object of interest, which is then iteratively deformed to minimize an energy functional. This functional consists of internal energy, which maintains the contour's smoothness; external energy, derived from image data to attract the contour to edges; and constraint energy, incorporating user-defined constraints. The goal is to balance these energies to accurately delineate object boundaries. Despite their effectiveness, active contour models face challenges such as sensitivity to initialization, convergence to local minima, and computational intensity [67]. To address these issues, various improvements have been proposed, such as Gradient Vector Flow (GVF) snakes [67], which improve convergence and handle concave regions better; level set methods, which allow for topological changes; and geodesic active contours, which use geodesic principles for more robust segmentation. These enhancements aim to improve accuracy, robustness, and computational efficiency in various applications, particularly in medical imaging and computer vision.

In the paper by K. Rajesh Babu et. al. [68], the researchers conducted a study on early brain tumor detection using T1 sequence MRI images. The study addresses the critical issue of improving patient survival rates by facilitating accurate and timely tumor detection. The challenge lies in the traditional manual detection process, which is both time-consuming and dependent on expert knowledge. To overcome this, the authors proposed an automated framework incorporating active contour segmentation

techniques, specifically the level set method and the Chan-Vese model. The framework consists of three primary steps: pre-processing to eliminate noise and irrelevant regions, thresholding to isolate the tumor, and segmentation to precisely delineate tumor boundaries. The performance of the method was validated using the Harvard MRI dataset, demonstrating improved accuracy through metrics such as the Dice coefficient, Hausdorff distance, and Jaccard similarity index. The LSM method recorded higher HD values (2.04 and 2.08), while the CV model achieved lower HD values (1.78 and 1.59), indicating superior segmentation performance as HD values closer to zero reflect better accuracy.

In another study, Z. Rguibi et. al. [13] proposed an edge-region-based active contour method for MRI segmentation. This approach integrated edge detection and region information, improving the accuracy of tumor boundary delineation. Their method demonstrated the potential to enhance diagnostic accuracy by providing precise segmentation, particularly in complex tissue structures.

Shahvaran et. al. [69] conducted a study aimed at improving the accuracy and efficiency of brain tumor extraction from multimodal MR images, which combine data from multiple MRI sequences to provide complementary information. Manual delineation of brain tumors is often labor-intensive and prone to human error, making automated approaches essential. To address this, the researchers proposed a method that integrates k-means clustering for initial tumor detection with a morphological region-based active contour model for precise tumor extraction. The model leverages Gaussian distribution to represent local image intensities and Markov random fields to account for spatial correlations among neighboring voxels, ensuring more accurate segmentation. The approach achieved high performance, with mean Dice similarity coefficients of 0.9179 for high-grade tumors and 0.8910 for low-grade tumors. However, the method's reliance on the accurate placement of the initial contour and sensitivity to intensity variations remain areas for further refinement.

A study by Niloufar Alipour et. al. addresses the challenges of brain tumor segmentation in MRI images, specifically focusing on issues such as poor boundaries, noise, and image heterogeneity [70]. The researchers propose a novel region-based fuzzy active contour model that incorporates superpixel segmentation to enhance performance. This model reduces dependence on initial contours and computational costs by using super pixels as basic units. Their method demonstrates superior accuracy compared to existing state-of-the-art models for both real and synthetic brain MR

images. However, the method has a limitation in that it reduces image resolution due to the utilization of super pixels, which could potentially be mitigated by combining the super pixel-based approach with pixel-level segmentation to preserve accuracy.

2.5.6 Integration Method

Segmentation of MRI images, particularly in the presence of complex tissue structures, is a significant hurdle. Traditional methods struggle with accurately delineating tumor boundaries due to overlapping signal intensities from adjacent tissues. Recent studies from Fonseca et. al [71] have proposed integrating edge-region-based active contour methods and entropy-based approaches with modified Canny techniques to enhance MRI segmentation. This combination of algorithms improves the accuracy of feature extraction by effectively distinguishing between regions with similar signal intensities.

L. Atikah et. al. [72] proposed a segmentation approach that integrates K-Means clustering with morphological operations to enhance the segmentation of tumor regions in MRI images. K-Means clustering segments the image based on intensity values, while morphological operations refine the results by removing small artifacts and closing gaps in boundaries. This combination improves the accuracy of segmentation in images with noise and overlapping intensities by addressing limitations of clustering methods alone. The combined use of adaptive thresholding, K-means clustering, and mathematical morphology achieved the highest DSC of 0.76 for corpus callosum segmentation.

K. Hajdowska et. al. [73] developed a hybrid approach combining watershed segmentation and graph-based techniques to improve segmentation accuracy in medical images. The watershed algorithm provides initial segmentation, while graph-based refinement eliminates over-segmentation and ensures boundary precision. This integration addresses challenges in detecting irregularly shaped objects and regions with low-intensity contrast, achieving superior segmentation in volumetric datasets.

Table 2.5 summarise the used of algorithms in MRI image processing: FCM, Morphological Operations, MT, Otsu thresholding and Active Contour. This comparison highlights the advantages and limitations of each algorithm, demonstrating their respective strengths and weaknesses in the context of medical imaging.

Table 2.5
Comparison Table

Methods	Authors	Discussion	Limitation
ST-AL (Hybridized Metaheuristic Algorithm)	Reham R. Mostafa et al.[40]	Incorporates image thresholding techniques to enhance segmentation accuracy in high-dimensional industrial datasets. The proposed algorithm shows improved convergence and robustness compared to state-of-the-art methods, achieving mean accuracy values between 0.94 and 1.00.	Potential for overfitting and need for further optimization to handle larger datasets effectively.
Metaheuristic Algorithm for Non-linear Equation Systems	A.Kamsyakawuniet al.[41]	Employs a metaheuristic algorithm focusing on thresholding techniques for precise segmentation of complex roots.	May struggle with very complex or noisy images, requiring further enhancement for robustness and versatility.
Otsu's Thresholding Method for MRI Brain Tumor Segmentation	Than et al.[43]	Applies Otsu's thresholding method to isolate and describe anatomical structures within MRI images. Experiments on the 2015 BRATS dataset show that class 4 achieved 68.80% sensitivity and 95.56% accuracy.	Susceptible to noise, leading to potential inaccuracies in region extraction.
Adaptive Trapezoid Region Intercept Histogram-based Otsu (ATRIH_Otsu)	Leyi Xiao et al.[44]	Enhances Otsu method with hierarchical threshold model and adaptive filtering for better segmentation accuracy.	Noise identification remains a challenge, suggesting improvements in noise recognition needed.
Modified Multi-level Otsu Thresholding (MLOT)	Utsav Kumar Malviya et al.[45]	Uses modified Otsu thresholding for accurate and automated detection of brain tumors in MRI images.	Increased computational complexity and sensitivity to noise, requiring optimization.
SLICs+MTh (Supervoxels and Otsu Multilevel Thresholding)	Esha Baidya Kayal et al.[47]	Combines multilevel thresholding with supervoxels to enhance segmentation efficiency in tumor evaluation. Active tumor, necrosis, and edema were segmented with satisfactory performance (JI: 62–78%, DC: 72–87%, precision: 67–87%, recall: 63–88%), with necrosis areas showing good correlation with hypointense regions in PC-T1W (DC: 74 ± 9%).	Heterogeneity in tumor tissue can impact segmentation accuracy.
Modified Salp Swarm Algorithm-based Multilevel Thresholding	Wang et al.[48]	Optimizes image segmentation by separating regions within an image more precisely than binary thresholding.	Increasing the number of thresholds can reduce segmentation accuracy, requiring balance between accuracy and computational complexity.
FODPSO (Fractional Order Darwinian Particle Swarm Optimization)	S. Prasathet. al.[49]	Combines FODPSO with multilevel thresholding to enhance biomedical image segmentation accuracy.	Computational complexity and need for optimization of multiple parameters.

Multi-level Thresholding with SMA and Symmetric Cross-Entropy	Yuanyuan Jiang et al.[50]	Uses improved Slime Mould Algorithm and symmetric cross-entropy to enhance segmentation accuracy in complex datasets.	Increased computational demands with highly complex images and need for further refinement to improve robustness.
Fuzzy-based Multi-region Thresholding	Deepika Koundal et al.[51]	Uses fuzzy clustering with local spatial information for accurate segmentation in noisy images.	Sensitivity to initial cluster numbers and computationally complex.
Multilevel Thresholding with Masi Entropy	Shubham et al.[52]	Applies Masi entropy to find optimal threshold values for segmenting-colored images into distinct regions.	Sensitivity to noise and dependence on initial parameter settings.
Morphological Operations with Noise Reduction	Huang et al.[55]	Combines morphological operations with median filtering and morphological opening to mitigate noise in MRI images.	Susceptible to noise, causing inaccuracies in region extraction.
Adaptive Contrast Enhancement with Morphological Operations	Zhang et al.[56]	Dynamically adjusts contrast levels in MRI scans to enhance the visibility of the region of interest.	Poor contrast between regions of interest and surrounding tissues can hinder effectiveness.
Hybrid Approach with Morphological Operations and Deep Learning	M. R. Canales-Fiscal et al.[57]	Integrates morphological operations with CNNs for handling complex structures in MRI images. The MCNN method achieved an AUC of 0.94 for melanoma classification and 0.65 for glaucoma detection, matching or outperforming popular CNN architectures.	High computational cost and complexity.
Modified Morphological Gradient Method	J. Mehena et al.[74]	Combines morphological operations with edge detection algorithms to maintain sharp and accurate boundaries.	Susceptible to noise and false positives during the morphological processing stages.
Parallel Processing for Morphological Operations	K.Thiruvenkadamet al.[75]	Distributes computational load across multiple processors to enhance efficiency of morphological operations.	Computational efficiency can still be a concern with large datasets typical of MRI scans.
Bias-Compensated FCM (BCFCM)	M. Ahmed et al.[59]	Modifies FCM by incorporating the influence of neighbouring pixel labels for accurate MRI segmentation.	Computational complexity and sensitivity to noise.
Adaptive Fuzzy C-means (AFCM)	Balafar, M.A[60]	Adapts to local intensity variations by modifying the objective function of traditional FCM for robust segmentation.	Requires careful parameter tuning and higher computational cost.
FCM Clustering with Spatial Constraints (FCM_S)	S. Chen et al.[61]	Enhances FCM by incorporating spatial information into the clustering process for better segmentation accuracy.	Challenges with noise sensitivity and robustness to outliers.
Residual-driven FCM Clustering	Wang et.al.[62]	Enhances traditional FCM by incorporating residual information to improve segmentation quality in noisy environments.	Requires careful selection of parameters and computationally intensive.
FCMs with Spatial Intensity	Qingsheng Wang et al.[63]	Incorporates spatial and intensity constraints into FCM for better segmentation	Computational complexity, especially for large datasets.

Constraint Membership (FCM_SICM)		accuracy in images with intensity similarities.	
FCM-based Clustering with Edge and Local Information	M.M. Kh et al.[64]	Incorporates edge and local information into FCM-based clustering to enhance segmentation performance.	High computational cost and sensitivity to noise.
PFLSCM (Patch-based Fuzzy Local Similarity C-means)	Yiming Tang et al.[65]	Combines SSIM index and weighted sum distance of image patches for enhanced segmentation accuracy.	High complexity and limited applicability in real-time applications.
Density Peaks and Particle Swarm Optimization with FCM	Xiang-yi Liu et al.[76]	Combines density peaks and particle swarm optimization to improve FCM for segmentation accuracy and efficiency.	Challenges in handling very high-dimensional data.
Active Contour Segmentation with Level Set Method	K. Rajesh Babu et al.[68]	Uses level set method and Chan-Vese model for automated brain tumor detection in MRI images. The LSM method recorded higher HD values (2.04 and 2.08), while the CV model achieved lower HD values (1.78 and 1.59), indicating superior segmentation performance as HD values closer to zero reflect better accuracy.	Time-consuming and expertise-dependent nature of manual tumor detection.
K-means Clustering with Morphological Region-based Active Contour Model	Shahvaran et al.[69]	Combines k-means clustering for initial tumor detection with morphological region-based active contour model. On the BraTS 2013 dataset, the proposed method achieved mean Dice scores of 0.92 for high-grade tumors and 0.89 for low-grade tumors, outperforming other active contour–based approaches.	Dependency on initial contour placement and sensitivity to intensity variations.
Fuzzy Active Contour Model with Super pixel Segmentation	Niloufar Alipour et al.[70]	Uses super pixel segmentation to reduce dependency on initial contours and computational cost in brain tumor segmentation.	Reduced image resolution due to superpixel utilization.

Table 2.5 provides an overview of advanced segmentation methods for addressing challenges in medical imaging, particularly MRI scans. Techniques like modified FCM clustering and MT have been extensively developed to enhance segmentation accuracy, reduce computational costs, and improve robustness against noise and intensity variations. Methods such as FCM_SICM and PFLSCM incorporate spatial and intensity constraints or patch-based analysis to address overlapping intensities and improve segmentation precision. However, computational complexity, sensitivity to noise, and initial parameter dependencies remain common limitations.

Additionally, hybrid approaches, including ST-AL and FODPSO, integrate metaheuristic optimization with segmentation techniques to handle high-dimensional datasets effectively, although they still face scalability challenges. Morphological operations, combined with clustering and deep learning, have also proven effective for noise mitigation and boundary sharpness, though they are computationally demanding. Active contour models and super pixel segmentation further demonstrate advancements in automating tumor detection and reducing dependence on manual processes, yet they face issues like sensitivity to initial placements and resolution reduction.

2.6 Summary

This chapter reviewed the challenges and developments in MRI-based image segmentation, particularly for OS cases. FCM clustering, while widely used for tissue segmentation, was found to have limitations in handling intensity inhomogeneity, overlapping intensities, and sensitivity to noise. Several improved methods and hybrid techniques were discussed to overcome these issues, aiming to enhance segmentation accuracy and reduce manual intervention. The review also emphasized the clinical significance of necrosis extraction in OS, where MRI serves as a key imaging modality due to its ability to visualize tumor structure in detail. Manual interpretation of MRI images, although common, is subjective and time-consuming, prompting the need for automated approaches. Conventional image processing techniques such as thresholding, clustering, and fusion methods were explored, and the integration of these methods was identified as a promising direction to improve the reliability of necrosis extraction. Based on the literature, the development of an integrated segmentation technique that combines multiple MRI sequences and algorithms offers strong potential for supporting OS diagnosis and treatment planning.

CHAPTER 3
RESEARCH METHODOLOGY

3.1 Introduction

The effective diagnosis and treatment of OS necessitate accurate necrosis detection within MRI scans. This section outlines the methodology employed to develop a technique by integrating three MRI sequences to extract necrosis in OS patients. Figure 3.1 shows the integration process between the MRI sequences namely T1 sequences, T2 sequences, and T1 GADO sequences. There are two proposed methods in this study to extract the necrosis. The first proposed method is Adaptive Disk Structural Element Morphological (ADSEM) approach, while the second proposed method is Multilevel Thresholding FCM (MTFCM) method.

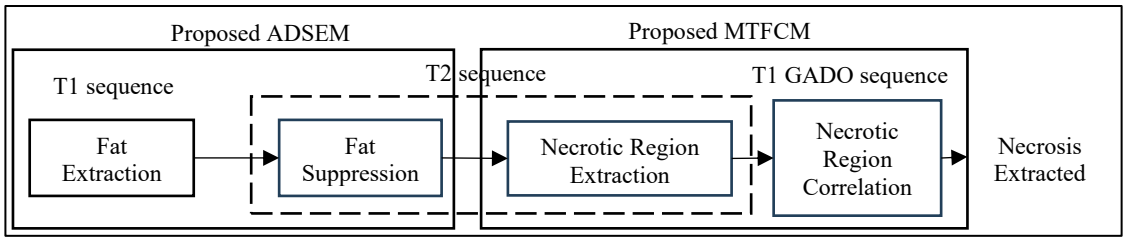

Figure 3.1 Integration Process

Figure 3.1 shows the integration process flow, which includes four main steps: Fat Extraction, Fat Suppression, Necrotic Region Extraction, and Necrotic Region Correlation. Each step uses different MRI sequences and methods to achieve final necrosis extraction.

The first stage is fat extraction, where the T1 sequence is loaded for processing. Fat appears bright and distinct in T1 sequences, allowing for accurate identification and delineation of fat regions. Most of the T1 sequences collected in this study are affected by inhomogeneities. Inhomogeneities refer to variations in signal intensity caused by inconsistencies in the magnetic field or imperfections in the imaging process. To compensate for signal inhomogeneity, an ADSEM method is proposed. The ADSEM method addresses these inhomogeneities within the T1 sequences, ensuring that the fat regions are outlined precisely. Accurately extracting fat is crucial, as its presence can interfere with subsequent steps in identifying necrotic regions.

The second stage is fat suppression, where the process involves isolating fat regions that were extracted in the T1 sequence and then suppressing them in the T2 sequences. Fat suppression is necessary because fat appears bright in T2 sequences, which can cause confusion when distinguishing between abnormal tissues and fat. The fat suppression process is achieved by overlaying the fat regions extracted from the T1 sequence onto the T2 sequences to remove the fat. After fat suppression, the abnormal regions become more prominent, facilitating easier detection and analysis. These abnormal regions may include edema, necrosis, and other abnormalities that consist of fluid-type lesions, making it easier to focus on relevant areas for further analysis.

In the third stage, the proposed method focuses on extracting potential necrotic regions, where the necrotic tissue in the T2 sequence with very hyperintense (VHPR) intensity regions is extracted. After fat suppression, abnormalities in the T2 sequence are highlighted. These abnormal regions may consist of both necrotic and viable tissues. This stage separates potential necrotic tissue from viable tissues, ensuring that only the necrotic regions are retained for further analysis.

In the fourth stage, the proposed MTFCM method correlates the bright region in the T2 sequence with the dark region in the T1 GADO sequence to extract necrosis. As discussed in Section 1.3, the T1 GADO sequence is commonly used in medical imaging to detect abnormal fluids. Necrosis appears as hypointense in the T1 GADO sequence, making it a reliable indicator for identifying necrotic regions.

Figure 3.2 depicts the overall proposed flow chart for this study. The methodology comprises five primary steps which are Data collection, image pre-processing, abnormality extraction, necrosis extraction and performance evaluation.

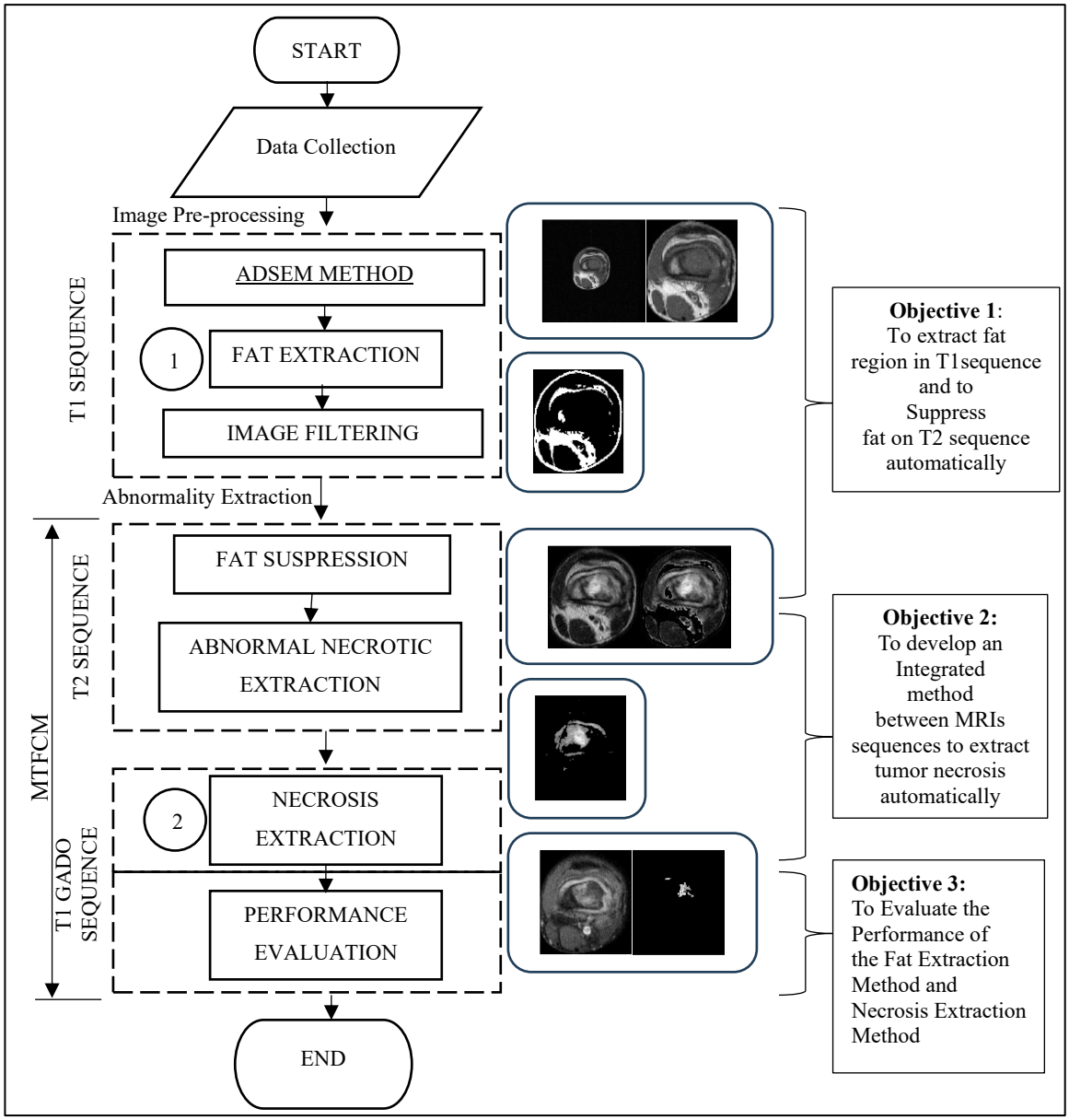

Figure 3.2 The Flow of The Research Methodology

3.2 Data Collection

Data collection in this study was conducted at Hospital Universiti Sains Malaysia (HUSM) in Kubang Kerian, Kelantan. There were thirty-five OS patients in total, with 223 slices in the data collection. All the slices are in axial view of the tibia and femur's diaphysis region. Ethical approval was secured from the Human Research Ethics Committee USM (HREC) under the code USM/JEPem/22060378, ensuring the study's ethical integrity.

The MRI scans were acquired in grayscale format and included three specific sequences: T1 sequences, T2 sequences, and T1 GADO sequences. The axial plane images were collected where the images are slicing through the diaphysis region of the

tibia and femur. Out of the 223 image slices, 122 were from the femur, while 101 were from the tibia. Table 3.1 presents the total number of slices along with their corresponding counts.

Table 3.1
List of Cases With Number of Slices

Case	Number of slices
Femur	122
Tibia	101
Total	223

3.3 Image Pre-processing

In this study, the process begins with image pre-processing. This process is crucial because most of the T1 sequence images in the collected data were suffer from inhomogeneity. Inhomogeneity, as explained in section 2.4 is a type of noise characterized by uneven fat distribution that appears in the images. To address this issue, the ADSEM method is proposed to compensate for the inhomogeneity in T1 sequences. This method corrects variations in intensity, ensuring a consistent and accurate extraction of the fat regions. The image pre-processing process plays a crucial role in mitigating the effects of inhomogeneity and ensuring reliable extraction of fat in the T1 sequence so that the fat can be effectively suppressed in the T2 sequence. Figure 3.3 shows the block diagram for image pre-processing, which consists of three main steps: the proposed ADSEM method, image registration, and fat extraction.

Figure 3.3 Image Pre-Processing Block Diagram

The proposed ADSEM method is employed to compensate for inhomogeneity within the T1 sequences, ensuring uniform intensity across the image. This adjustment ensures that the fat at the outer regions of the image maintains consistent intensity, facilitating more accurate fat extraction and reducing errors in subsequent steps. Image registration aligns the T1 sequences to ensure consistency across different sequences, while fat extraction isolates the fat region to enhance the accuracy of subsequent analyses.

3.3.1 Proposed ADSEM Method

As explained in section 3.1, ADSEM method is proposed to correct intensity inhomogeneity in T1 sequences so that fat region can be extracted effectively. Figure 3.4 shows the flow chart for the proposed ADSEM method.

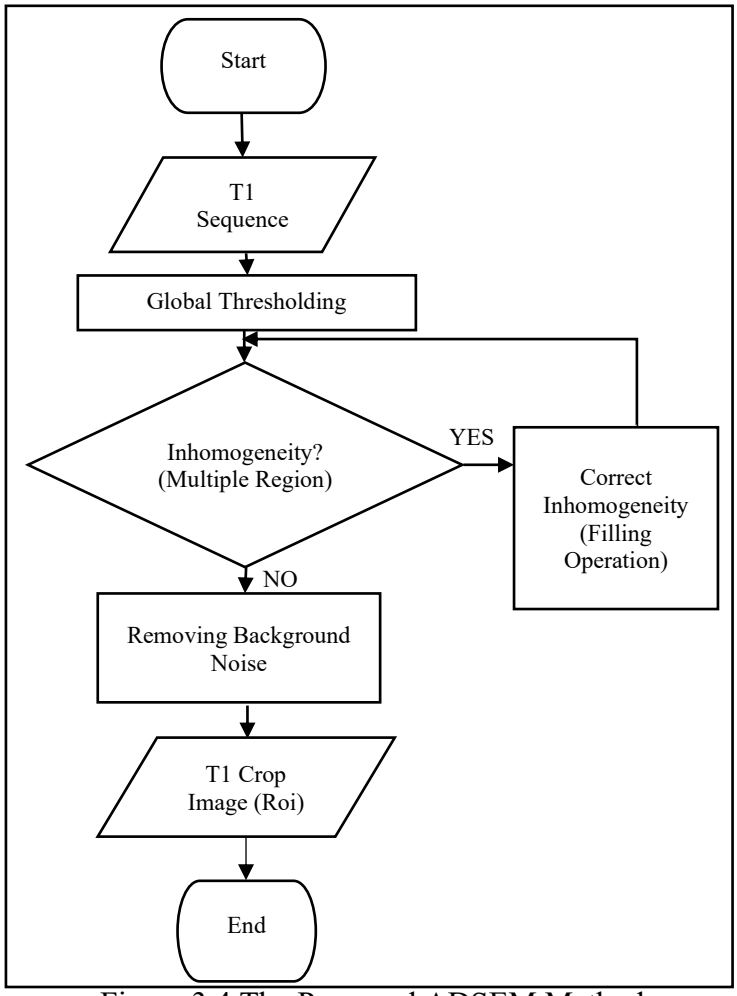

Figure 3.4 The Proposed ADSEM Method

The ADSEM method begins by loading a T1 sequence as input and converting it into a binary image using global thresholding. The rationale for selecting the ADSEM approach is its ability to explicitly address intensity inhomogeneity, which commonly affects T1 MRI sequences and compromises conventional threshold-based fat extraction. This step separates the background (black region) and object (white region) from MRI images. The ROI, which consists of fat and muscle in the T1 sequence, is subsequently analyzed. In an ideal scenario, the outer region of the object, which represents fat, should appear as a single connected region when image intensity is

uniform. However, due to inhomogeneity, global thresholding often fails to entirely separate the outer fat region because of uneven intensity distribution across the image. This uneven intensity leads to incorrect segmentation, causing multiple disconnected fat regions to appear after the global thresholding process.

The selection of ADSEM is motivated by the observation that the presence of multiple disconnected objects after thresholding is a direct indicator of intensity inhomogeneity. When such multiple objects are detected, a filling operation is performed to reconnect regions disrupted by intensity variations. Morphological dilation using a disk-shaped Structuring Element (SE) is then applied to thicken the ROI. The number of objects within the ROI is counted, and this process is repeated until only one connected object is detected. This iterative connectivity-based criterion distinguishes ADSEM from fixed-parameter morphological methods, which lack adaptability to varying inhomogeneity levels.

During the first iteration, the SE size is set to one and is increased progressively in subsequent iterations. This adaptive adjustment of the SE size allows the method to respond dynamically to the severity of inhomogeneity present in each image, ensuring sufficient correction without excessive dilation. The number of iterations corresponds to the SE size, enabling the method to automatically scale its correction process. Once a single connected region is achieved, indicating that inhomogeneity correction is complete, the filling operation concludes. Background noise is then removed by setting background pixel values to zero, and the ROI is cropped based on the connected region to retain only informative areas for further analysis.

The ADSEM method automatically adjusts the size of the SE during processing, compensating for inhomogeneities in the T1 sequences to extract fat. This adaptive disk-based morphological strategy is the primary reason for selecting ADSEM, as it provides a robust, data-driven solution for inhomogeneity correction while preserving anatomical continuity, thereby improving the reliability of subsequent necrosis extraction stages.

3.3.2 Image Registration

Image registration is an important step to align multiple images taken at different times. This process ensures that the corresponding anatomical structures accurately overlap across these images. In this study, image registration is applied to align T1

sequences, T2 sequences, and T1 GADO sequences, ensuring that corresponding structures such as fat, muscle, and lesions are overlap correctly with one another.

In this study, T1 sequences are used as the reference image because they serve as the fundamental sequence for visualizing anatomical structures, providing essential details for accurately extracting the fat region. Affine registration is used as the default setting, providing a balance between correcting geometric distortions and maintaining computational efficiency. By utilizing image registration, the T1, T2, and T1 GADO sequences are aligned. This process ensures accurate alignment across sequences, improving the precision of fat and necrosis extraction processes.

3.3.3 Fat Extraction

Fat extraction is a crucial process in this study. The primary purpose of fat extraction is to eliminate fat regions that may interfere with necrosis identification, as fat and necrotic tissues can exhibit overlapping intensity characteristics in MRI sequences. The accuracy of necrosis extraction is highly dependent on the effectiveness of the fat extraction stage. By isolating and suppressing fat regions, the ROI can be defined more precisely, reducing false positives during necrosis segmentation. Precise fat extraction helps in delineating the ROI more clearly, thus facilitating the accurate detection of necrotic tissue in later stages. To achieve an accurate final fat extraction, two sub-processes are employed: pre-fat extraction and image filtering.

3.3.3.1 Pre-Fat Extraction Process

Figure 3.5 illustrates the block diagram depicting the pre-fat extraction process. The process involves three primary steps. The first step consists of “Create Outline” and “FCM Algorithm”. Second step is integrating process using arithmetic ADD operation. Third step is morphological process and AND operation for pre-fat extraction.

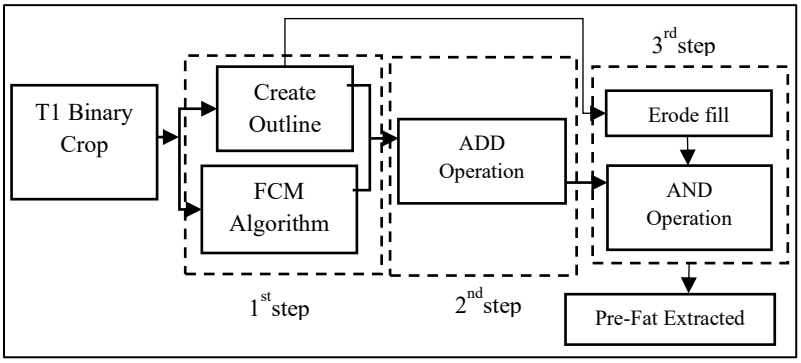

Figure 3.5 Block Diagram for Pre-Fat Extraction Process

As explained in section 3.3.1, the proposed ADSEM method compensates for inhomogeneity by dilating the ROI, ensuring that multiple fat regions are dynamically connected through an iterative dilation process with the size of the SE adjusted automatically. Subsequently, in the "Create Outline" phase, the ROI resulting from the ADSEM outcome undergoes erosion, producing an eroded image. The outline is then created through arithmetic subtraction of the dilated and eroded images. The purpose of creating an outline in binary fat region images is to correct inhomogeneity at the outer region of the MRI image. This step ensures that any multiple disconnected regions at the outer region, which are identified as fat regions, are connected. By creating this outline, the process compensates the intensity variations in the outer areas of the MRI image. Next, the FCM algorithm is applied to cluster the ROI into three regions: high intensity (fat), intermediate intensity (muscle), and low intensity (cortical bone).By applying FCM, the highest intensity representing the fat region is used to extract the pre-fat in T1 sequences.

For the second step, the output of the FCM algorithm, which identifies the fat region, is integrated with the outline generated in the “Create Outline” process using an ADD operation to address gaps caused by inhomogeneity. This integration helps to bridge any discrepancies in the inhomogeneous areas within the ROI.

The third step involves a logical AND operation, which integrates the results from the ADD operation with the eroded fill image from the “Create Outline” process. This step restores the mask to its original dimensions, refining the pre-fat region extraction. Through these combined steps, the “Outline” plus “FCM” method ensures correction of inhomogeneity and precise extraction of pre-fat regions from MRI images.

3.3.3.2 Image Filtering

Due to the similarity in intensity between fat and lesions, the pre-fat region extracted from section 3.3.3.1 may consist of both fat and lesion. Lesions are significant areas as they represent abnormal regions that may contain necrosis. Consequently, the pre-fat region in section 3.3.3.1 needs to be refined to effectively filter out lesions and retain only fat in the T1 sequence. Image filtering is employed in this section to refine the pre-fat region by removing lesions while maintaining fat. Figure 3.6 Illustrates the process used to differentiate fat from lesions in the pre-fat region of the T1 sequence. The image filtering process consists of two parameters: intensity filtering and standard deviation filtering.

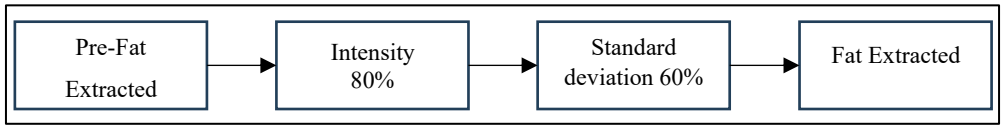

Figure 3.6 Fat Extraction Process From the Pre-Fat Region

The filtering process begins by removing small objects in T1 sequences. In this study, objects with an area of less than 5 pixels are considered too small to be significant and are removed from further analysis. The study specifically uses 8-connectivity for connected region labeling, where each pixel is connected to its eight immediate neighbors in the horizontal, vertical, or diagonal directions. Figure 3.7 shows the labelled matrix identifying connected components using 8-connectivity.

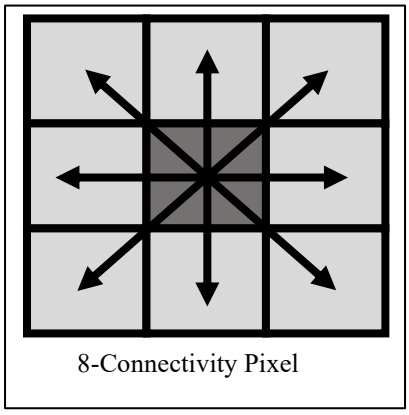

Figure 3.7 Label Matrixes that Label the Connected Components Using 8-Connectivity

Besides, this study analyses the intensity and standard deviation of each labelled region to identify true fat regions. These parameters are considered because fat intensity

is higher than that of other lesions and tissues. The standard deviation measures the consistency of intensity values within each region, helping to filter out non-fat regions such as noise or misclassified areas. By considering these two parameters, the true fat regions are identified and extracted.

Fat and lesions have similar intensity in T1 sequences, however fat has slightly higher intensity than lesions. Based on the histogram intensity distribution depicted in Figure 3.8, the signal intensity of fat in T1 sequences is higher compared to other tissues. The histogram shows that the highest intensity pixels, above 80%, correspond to fat regions, while those below 80% include other tissues such as bone marrow, cortical bone, lesions, and muscle. This 80% threshold value ensures that only high-intensity pixels, representing fat, are segmented, while lower-intensity regions are excluded from fat classification.

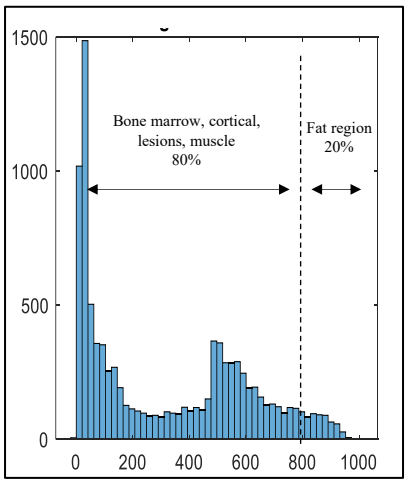

Figure 3.8 The Histogram Intensity Bone Marrow, Cortical, Lesions, Muscle and Fat Region

With this process, regions with intensity values above 80% of the maximum intensity in the T1 sequence are classified as fat, while those below 80% are categorized as non-fat. This segmentation isolates fat regions with intensity above 80%, separating them from other tissues such as lesions, bone marrow, and muscle.

To further refine the fat extraction process, this study employs standard deviation as a key parameter to differentiate fat from non-fat regions. Standard deviation quantifies the variation in intensity values within a region, providing a measure of intensity consistency. Real fat typically exhibits uniform intensity, resulting in a lower standard deviation compared to other tissues such as lesions or viable tumors, which

show greater intensity variations. This characteristic is utilized for analysis in T1 GADO sequences, where real fat does not enhance, while other tissues exhibit varying levels of enhancement. To confirm consistency, the bright fat regions extracted from the T1 sequence are mapped onto the corresponding T1 GADO sequence, and their standard deviation is calculated. In this study, a standard deviation of 60% is applied to the mapped regions. The standard deviation ensures that only consistent, uniform-intensity fat regions are retained, effectively filtering out regions with higher variations, such as lesions and viable tumors.

From the analysis, it is determined that 60% of the standard deviation, when applied to the mapped T1 GADO sequence, is considered as real fat. This value is derived by analyzing the variation in intensity within the bright regions extracted from the T1 sequence, focusing on areas that remain consistent and distinguishable as fat across the T1 and T1 GADO sequences. Specifically, regions in the T1 sequence that are bright due to their high signal intensity are mapped onto the T1 GADO sequence, where fat appears dark due to the suppression effect of gadolinium. By combining the 60% standard deviation in the T1 GADO sequence with the 80% intensity threshold in the T1 sequence, this dual-parameter approach enhances fat extraction by extracting regions that consistently meet these criteria to identify and retain the true fat.

3.4 Abnormality Extraction

Abnormal region extraction is crucial for identifying necrotic tissues in OS treatment. One of the challenges in segmentation is overlapping intensities and noise in medical images. To address these issues, the integration of MT and FCM clustering offers an improve solution. MT simplifies intensity segmentation, while FCM improves precision in identifying unclear boundaries. Together, these methods enable accurate extraction of necrotic regions, forming the basis for the proposed MTFCM method to enhance treatment analysis.

3.4.1 Proposed MTFCM Method

As discussed in Section 3.1, the necrosis extraction process relies on the integration of T1, T2, and T1 GADO sequences, which is essential for necrosis identification. Individually, these sequences face challenges in fully isolating necrotic

regions due to intensity overlaps with other tissues, such as fat and viable tumors. To address these limitations, the proposed MTFCM method integrates MT with FCM clustering, combining the strengths of both techniques to enhance the precision of necrosis extraction. By leveraging the intensity variations and cross-referencing tissue characteristics across all three sequences, the MTFCM method correlates hyperintense regions in T2 with hypo-intense necrotic areas in T1 GADO while excluding fat regions identified in T1. This integration ensures a more robust and accurate necrosis extraction process, overcoming the limitations of individual sequences.

In this study, an integration method between MT and FCM clustering is proposed to extract necrotic regions. Figure 3.9 shows the block diagram for the process from the Proposed ADSEM Method to the Proposed MTFCM Method for necrosis extraction. As discussed in Section 3.3.3, the ADSEM method is utilized in the T1 sequence, where fat extraction is performed after obtaining the output from ADSEM. The ADSEM method serves primarily as a preprocessing step, removing high-intensity fat tissues to reduce irrelevant signals and enhance the accuracy of subsequent stages.

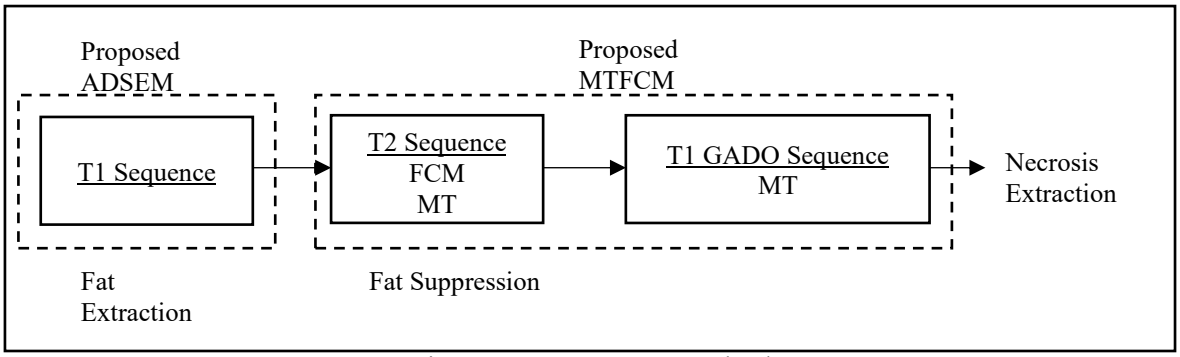

Figure 3.9 MTFCM Method

The extracted real fat from the T1 sequence is then used to suppress the fat in the T2 sequence, enabling the system to highlight regions of abnormality by eliminating unwanted fat and cortical bone signals. Figure 3.9 illustrates the proposed MTFCM method, which integrates FCM clustering and a MT method to correlate the T2 and T1 GADO sequences for necrosis extraction. Necrosis is extracted by leveraging information from the T1, T2, and T1 GADO sequences through the combined use of the ADSEM and MTFCM methods.

3.4.2 Fat Suppression

As explained in Section 2.3, T2 sequences are highly effective in highlighting fluid-rich tissues, particularly necrotic areas and edema, which appear bright due to their high fluid content and signal intensity. However, fat tissue also appears bright on T2 sequences, potentially obscuring these abnormalities. To address this limitation, fat suppression is applied to reduce the fat signal, allowing abnormal regions to be highlighted more clearly. In this stage, the abnormal regions appear bright on the T2 sequence and consist of abnormal fluid, necrotic tissue, edema, and viable tumors. As discussed in section 2.3 and summarized in Table 2.3, each type of abnormality displays different intensity characteristics: edema and viable tumors appear intense, while necrotic regions are bright.

Figure 3.10 illustrates the process of fat suppression and abnormality highlighting within the T1 and T2 sequences.

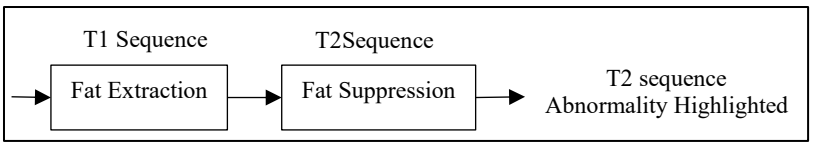

Figure 3.10 Process of Fat Suppression and Abnormality Highlighted

Figure 3.10 illustrates the fat extraction process in the T1 sequence, followed by fat suppression in the T2 sequence, where the abnormality is then highlighted. As explained in Section 3.3.3, the real fat extracted in the T1 sequence is used to suppress the fat in the T2 sequence. Once the fat is suppressed in T2 sequence, the noise from residual fat signals is reduced, enhancing the visibility of muscle tissue structures and potential abnormal areas in the T2 sequence. Due to their high intensity, the abnormal regions are highlighted in T2 sequence.

3.4.3 Pre-Necrotic Extraction

Figure 3.11 illustrates the process of pre-necrosis extraction in the T2 sequence. After the abnormal region is highlighted in the T2 sequence, the next process involves two key steps: extracting the abnormal region using the FCM method and utilizing a two-level MT method to extract the potential necrosis region. The two-level

thresholding technique is applied to the region of the highest intensity extracted by FCM.

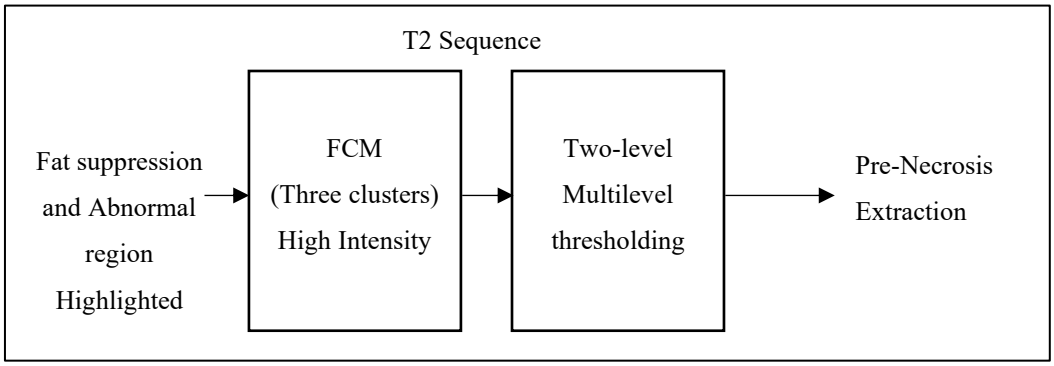

Figure 3.11 The Process of Pre-Necrotic Extraction in T2 Sequence

As discussed in Section 3.4.2, after the fat is suppressed, the abnormal regions are highlighted in the T2 sequence. These highlighted regions consist of abnormal fluid-rich tissues that may include necrosis. To extract these abnormal regions, the MTFCM method first utilizes the FCM algorithm. The FCM algorithm is chosen for its advantages in medical imaging, particularly in scenarios where boundaries between regions are not sharp, ensuring better segmentation of overlapping tissues. The FCM algorithm segments the fat-suppressed T2 sequence into three clusters: high-intensity represent abnormal regions, medium-intensity represent muscle regions, and low-intensity represent cortical bone regions.

As previously discussed in Section 2.3 and shown in Table 2.2 and Table 2.3, both fat and necrotic regions appear bright in the T2 sequence due to their high signal intensity. The high-intensity regions identified by FCM include potential necrotic tissue along with other abnormalities, such as edema and fluid-rich irregularities. Within these variations, potential pre-necrosis is distinguishable as a uniquely high-intensity area.

Even though both fat and necrotic regions appear bright in the T2 sequence, necrotic tissue demonstrates significantly higher signal intensity than fat, as stated in Table 2.3. The use of a two-level multilevel thresholding approach is therefore justified to further discriminate necrotic tissue from other high-intensity abnormalities within the FCM-derived abnormal cluster. The MTFCM algorithm utilizes this distinction by applying a two-level MT technique to enhance the segmentation process. A two-level threshold is selected to provide sufficient separation between background/low-intensity tissues, surrounding abnormal tissues, and the highest-intensity regions corresponding to necrosis, without introducing unnecessary segmentation complexity. This approach isolates the brightest regions—typically representing necrosis—while excluding other

high-intensity abnormalities such as edema. By focusing on these upper intensity levels, the MT narrow down areas that are likely to represent pre-necrotic or necrotic tissue. Compared to single-level thresholding, the two-level approach improves specificity by preventing edema-dominated regions from being misclassified as necrosis. The MT method is particularly beneficial for its speed and simplicity, as it segments images by analyzing and dividing intensity values based on histogram distributions. Figure 3.12 shows the histogram distribution of the T2 sequence after abnormal region extraction.

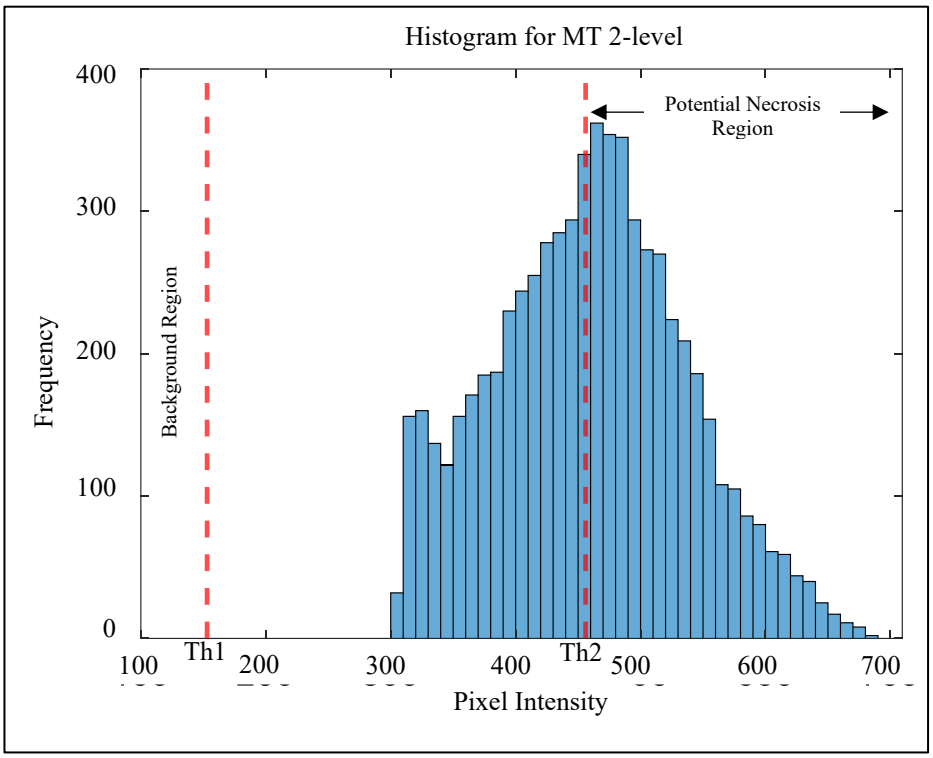

Figure 3.12 Histogram of MT 2-level

The histogram illustrates the distribution of pixel intensities for the T2 sequence after extracting abnormal regions. In the two-level multilevel thresholding strategy, the first threshold separates low-intensity pixels associated with background and non-informative tissues, while the second threshold distinguishes medium-intensity tissues from the highest-intensity pixels. The second threshold marks the boundary for the medium-intensity region, which generally corresponds to surrounding tissues.

As shown in Section 2.3 and Table 2.3, the brightest region corresponds to necrotic tissue, which exhibits very high signal intensity (Bright) in the T2 sequence. A dominant peak near this intensity is highlighted as the "Potential Necrosis Region," suggesting an area with high water content typically associated with necrotic tissues in

the T2 sequence. The presence of this peak in the bright intensity range emphasizes its clinical relevance, as abnormal tissues or necrotic regions commonly exhibit increased signal intensity in T2 sequences. By applying MT, this method isolates the high-intensity region, facilitating the identification of potential necrosis and enabling better analysis of abnormal tissue characteristics.

3.5 Necrosis Extraction

As explained in Section 2.3 in Figure 2.1, the necrotic regions in T1 GADO sequences appear hypo-intense (Dark) due to their poor blood supply, which prevents gadolinium uptake. This characteristic provides a clear contrast between necrotic and viable tissues, as viable tissues are enhanced and appear hyperintense. Fat appears dark, muscle light gray, and necrotic regions distinctly stand out as the darkest areas. This distinct intensity separation forms the primary rationale for adopting a multilevel thresholding strategy in the T1 GADO sequence.

To segment the Dark necrotic region in T1 GADO sequences, a three-level MT method is employed. The three-level approach is selected to explicitly separate background tissues, hypo-intense necrotic regions, and contrast-enhanced viable tissues, which cannot be reliably isolated using a single- or two-level threshold. Figure 3.13 shows the histogram of the segmented three-level MT.

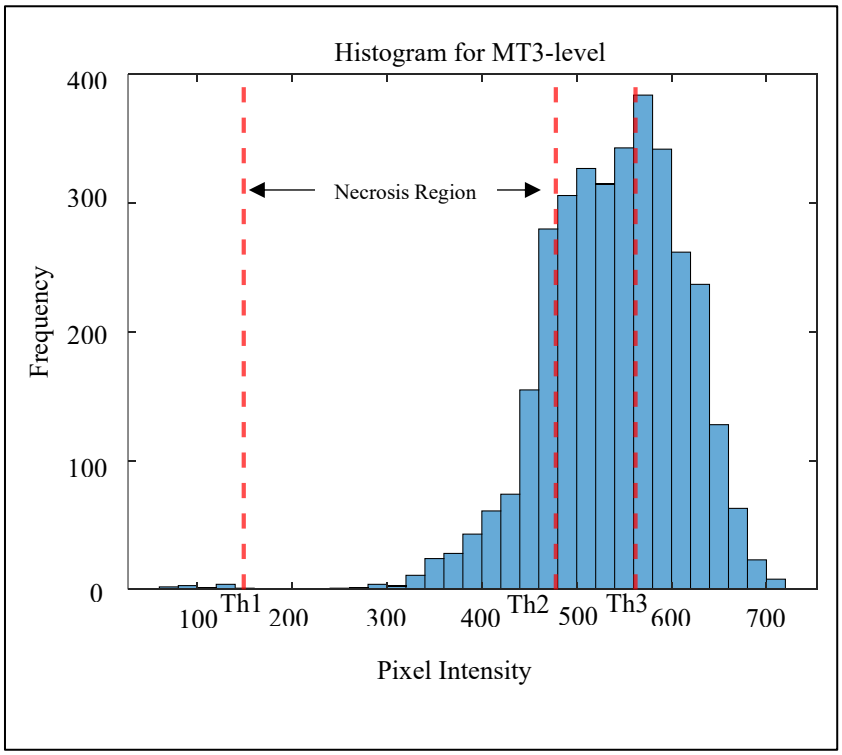

Figure 3.13 Histogram for Three-level MT

The histogram represents the pixel intensity distribution for the T1 GADO sequence to identify and extract the necrosis region. Using a three-level MT method, the first threshold separates background pixels, which are excluded as they hold no diagnostic significance. The second threshold, corresponding to the DARK intensity range, aligns with the necrotic areas in T1 GADO sequences, as indicated in Section 2.3 Table 2.3. This region is marked with arrow in the histogram, signifying its critical role in necrosis extraction. The third threshold is introduced to distinguish contrast-enhanced viable tissues from necrotic regions, ensuring that hyperintense regions influenced by gadolinium uptake are excluded from necrosis classification.

The third threshold separate remaining two regions represent INTENSE and BRIGHT values. These BRIGHT regions have a high possible correlation with normal tissues or areas with enhanced signal intensities due to the gadolinium contrast agent. The two dashed vertical lines at the thresholds segment the histogram, effectively separating the low-intensity necrotic region from the background and higher-intensity regions. A significant concentration of pixel intensities in the low range supports the identification of necrotic tissue, which appears darker in T1 Gado sequences. MT can extract the necrosis region, enabling clear differentiation from normal or enhanced tissues.

As explained in Section 3.4.3 for the T2 sequence, abnormal regions, including necrotic and viable tissues, appear bright due to their high fluid content and signal intensity. This brightness highlights potential necrotic areas as VHPR regions, which are extracted during the pre-necrosis extraction stage.

When these regions are mapped to the T1 GADO sequence, the contrast-enhanced characteristics of viable tissues and the hypo-intense nature of necrotic areas become essential for correlation. Necrotic regions, which appear as the darkest areas in the T1 GADO sequence, align with the highest intensity regions extracted from the T2 sequence. This correlation confirms the complementary nature of the two sequences: the T2 sequence highlights the fluid-rich necrotic areas, while the T1 GADO sequence verifies their necrotic nature through hypo-intensity.

By leveraging this correlation, the MT process segments hypo-intense regions in the T1 GADO sequence, corresponding to necrotic areas. The final step refines this process by aligning the extracted necrotic regions from the T2 sequence with those in the T1 GADO sequence. Figure 3.14 shows the correlation between the pre-necrosis region in the T2 sequence and the potential necrosis region in the T1 GADO sequence.

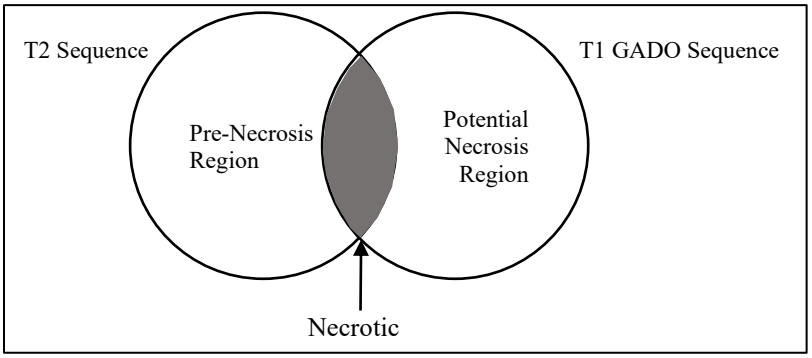

Figure 3.14 The Location of Necrosis in Correlation of Potential Necrotic Region and T1 GADO Sequence

The diagram shows the process of identifying necrotic regions by integrating information from two sources: Pre-necrosis region from T2 sequence and potential necrosis region from T1 GADO sequence. By overlapping these two datasets, the necrotic regions are confirmed as areas that appear abnormal in the T2 sequence but do not enhance in the T1 GADO sequence. Finally, the necrotic tissue is extracted from the T1 GADO sequence.

Figure 3.15 demonstrates the flow of the MTFCM method in the process of necrosis extraction, outlining how necrotic regions are identified. The potential necrotic regions extracted from the T2 sequence in Section 3.4 are correlated with the T1 GADO sequence to locate necrotic areas more precisely. Figure 3.15 illustrates the process in which the proposed MTFCM algorithm correlates the pre-necrosis region in the T2 sequence with the potential necrosis region in the T1 GADO sequence. For necrosis extraction, MTFCM employs a three-level MT approach in T1 GADO to identify necrotic regions. For necrosis extraction, MTFCM employs a three-level MT approach in the T1 GADO sequence to ensure robust separation of background, necrotic, and contrast-enhanced tissues, while avoiding misclassification that may occur with fewer threshold levels. For comparison, FCM with four clusters is applied to extract necrosis.

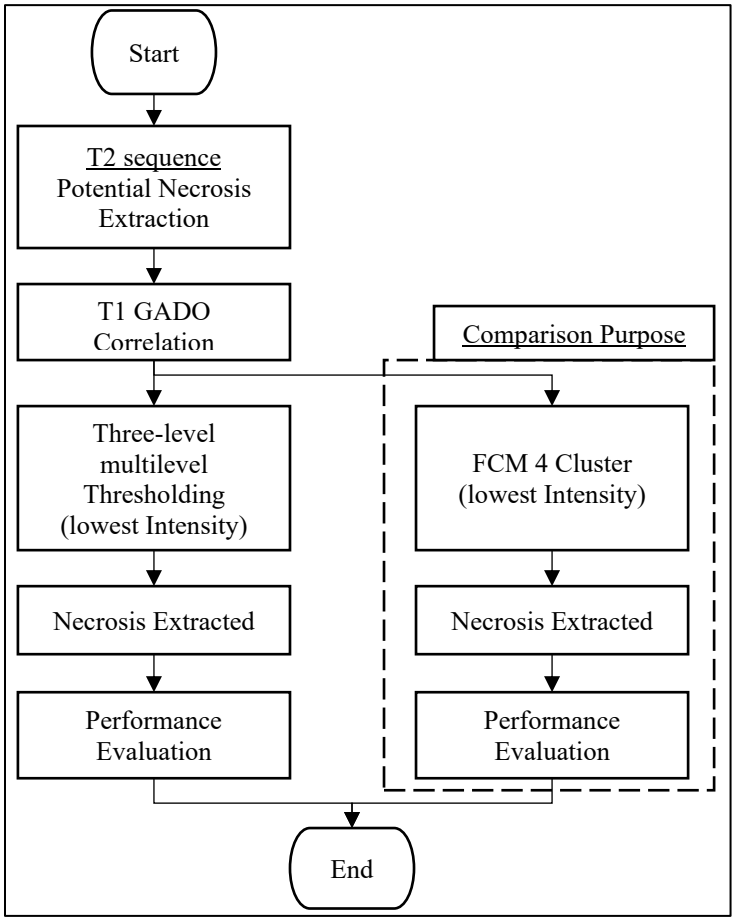

Figure 3.15 The Block Diagram of the Necrosis Extraction Process

Necrosis is extracted using both MT and FCM methods, and a performance evaluation is conducted to assess and compare their effectiveness.

3.6 Performance Evaluation

The performance evaluation of this study is divided into two parts: fat extraction and necrosis extraction. The experiment was conducted on a total of 223 MRI slices. To assess the method's effectiveness, the experimental results were compared with the ground truth. For fat extraction, a quantitative analysis was conducted. The ground truth was manually created based on detail descriptions provided by an experienced radiologist. For necrosis extraction, a qualitative analysis was performed, with the ground truth established by experienced radiologists alongside every slice in the data collection. The experiments were conducted using MATLAB 2019 on a laptop equipped with an Intel(R) Core(TM) i5-7200U CPU @ 2.50GHz and 12GB of RAM.

3.6.1 Classification Metrics

To quantify the performance of the method, this study uses four key metrics from the confusion matrix which are True Positive (TP), True Negative (TN), False Positive (FP), and False Negative (FN). These matrixes are to evaluate the effectiveness of fat and necrosis extraction. A matrix was created by comparing the experimental results with the ground truth to assess the method's accuracy.

Table 3.2 shows the confusion matrix, comprising the four elements: TP, TN, FP, and FN. By using the metrics, the effectiveness of the ADSEM method and the MTFCM method can be evaluated in terms of accuracy and reliability.

Table 3.2
Confusion Matrix

	Actual Necrosis/Fat	**Actual Non-necrosis/Non-fat**
Predicted Necrosis/fat	True Positive (TP)	False Positive (FP)
Predicted Non-necrosis/Non-fat	False Negative (FN)	True Negative (TN)

Where:

- **True Positive (TP):** Instances where the algorithm accurately identified fat/necrosis regions, correctly classifying pixels or regions as fat/necrosis, consistent with the ground truth.
- **True Negative (TN)**: Instances where the algorithm correctly identified non-fat/non-necrosis regions, accurately classifying pixels or regions as non-fat/non-necrosis, aligning with the ground truth data.
- **False Positive (FP)**: Situations where the algorithm erroneously classified pixels or regions as fat/necrosis when they were actually non-fat/non-necrosis according to the ground truth data (over-segmentation).
- **False Negative (FN)**: Instances where the algorithm incorrectly classified pixels or regions as non-fat/non-necrosis when they were actually fat/necrosis as per the ground truth data (under-segmentation).

As explained in Section 3.1, the proposed ADSEM method compensates for inhomogeneity in T1 sequence, enhancing the effectiveness of fat extraction. Similarly, the proposed MTFCM method integrates T2 sequence and T1 GADO sequences to improve the effectiveness of necrosis extraction.

The performance of both proposed ADSEM and MTFCM methods is evaluated using key metrics derived from the confusion matrix, including Accuracy, Precision, Recall, and F1 score.

Accuracy: Calculated as the ratio of correctly classified fat/necrosis pixels to the total

number of pixels in the image, as depicted by the formula Eq.(3).

$$Accuracy = \frac{TP + TN}{TP + FP + TN + FN} \tag{3}$$

Precision: The algorithm's capacity to accurately identify fat/necrosis regions among all the regions classified as necrosis/fat, as illustrated by the formula in Eq.(4).

$$Precision = \frac{TP}{TP + FP} \tag{4}$$

Recall: Reflects the algorithm's proficiency in correctly identifying fat/necrosis regions among all the actual necrosis/fat regions in the ground truth data, as outlined by the formula in Eq.(5).

$$Recall = \frac{TP}{TP + FN} \tag{5}$$

F1 Score: Harmonic mean of precision and recall, offers a balanced metric encompassing both measures, as illustrated by the formula in Eq.(6).

$$F1\ score = \frac{2xPrecisionxRecall}{Precision + Recall} \tag{6}$$

3.6.2 Dice Similarity Coefficient (DSC)

DSC is a statistical tool used to measure the similarity between two sets, often used in image segmentation to assess the overlap between the ground truth and the extracted fat/necrotic regions. It provides a value between 0 and 1, where 1 represents perfect overlap. The formula as in Eq. (10).

$$DSC = \frac{2 \cdot |A \cap B|}{|A| + |B|} \tag{10}$$

Where:

A is the area of fat/necrosis

B is the segmented fat/necrosis area

$|A \cap B|$is the intersection of these areas

3.6.3 Intersection Over Union (IoU):

IoU is another metric used for evaluating the performance of image segmentation. It measures the ratio of the overlap between the extracted fat/necrosis and

the ground truth to the union of both sets. It is particularly useful in assessing the accuracy of the ADSEM and MTFCM model. The formula is illustrated as Eq. (11).

$$IoU = \frac{|A \cap B|}{|A \cup B|} \tag{11}$$

Where:

A is the ground truth of fat/necrosis

B is the predicted of fat/necrosis segmentation

$|A \cap B|$ is the intersection

$|A \cup B|$ is the union of the two regions

3.6.4 Pearson Correlation

Pearson correlation is employed to assess the linear relationship between the extracted necrotic areas and the ground truth necrotic areas provided by radiologists. This statistical measure evaluates the strength and direction of the linear association between the two continuous variables: the necrotic areas extracted by the algorithm and the necrotic areas identified by radiologists. The Pearson correlation coefficient (r) ranges between -1 and 1, where a higher value indicates a stronger positive correlation, reflecting the accuracy of the extraction method as illustrated by the formula in Eq. (12):

- A value of r=1 indicates a perfect positive linear relationship, meaning as the size of the necrotic region extracted increases, the size of the ground truth necrotic region increases proportionally.
- A value of r=-1 represents a perfect negative linear relationship, where an increase in the extracted necrotic region corresponds to a decrease in the ground truth region.
- A value of r=0 implies no linear relationship between the extracted and ground truth necrotic regions.

$$r = \frac{\sum(X_i - \bar{X})(Y_i - \bar{Y})}{\sqrt{\sum(X_i - \bar{X})^2}\sqrt{\sum(Y_i - \bar{Y})^2}} \tag{12}$$

Where:

X_i is the value of the necrotic region extracted by the method for the i-th sample

Y_i is the corresponding value from the ground truth

$\bar{X}$ is the mean of the extracted necrotic regions

$\bar{Y}$ is the mean of the ground truth necrotic regions

3.7 Summary

The purpose of this study is to extract tumor necrosis from MRI images of OS patients. To achieve this, two methods are proposed which are ADSEM and MTFCM. ADSEM is applied during the preprocessing stage to correct intensity inhomogeneity in T1 sequences, enabling accurate fat segmentation. The extracted fat region is then used to suppress fat in the T2 sequence, allowing clearer detection of abnormal fluid-rich areas. In the MTFCM method, both MT and FCM clustering are applied to the fat-suppressed T2 sequence to extract hyperintense regions, which are considered potential necrosis. Meanwhile, in the T1 GADO sequence, MT is used to extract hypo-intense regions representing another set of potential necrosis. Finally, the potential necrosis regions from T2 sequence and T1 GADO sequences are correlated to identify the final necrotic region. This integrated approach combines the speed of MT with the adaptability of FCM, allowing more accurate and automated necrosis extraction.

CHAPTER 4
RESULTS AND DISCUSSION

This chapter presents and discusses the results obtained from the proposed methods outlined in Chapter 3. The evaluation focuses on two key aspects: fat extraction using the proposed ADSEM method and necrosis extraction using the proposed MTFCM method. The proposed tumor necrosis extraction technique is implemented on the collected data, and its performance is evaluated using classification metrics, including Accuracy, Precision, Recall, and F1 Score. Additional assessment methods, such as the DSC, IoU, and Pearson Correlation Coefficient, are also applied. The results are analyzed by comparing the algorithm's outputs with the ground truth provided by radiologists, emphasizing both quantitative and qualitative performance evaluation metrics to determine the accuracy and reliability of these approaches in identifying fat tissues and necrotic regions in OS MRI images.

4.1 Image Pre-processing

As explained in Section 3.3, fat extraction in the T1 sequence is critical to ensure the accuracy of subsequent processing steps, particularly for extracting necrosis regions. Precise fat suppression is important to avoid confusion between fat and abnormal tissues during necrosis extraction. However, most T1 sequences are affected by intensity inhomogeneity, which can obscure the clear distinction between different tissue types. In this study, the ADSEM method is proposed in the image pre-processing step to correct inhomogeneity in T1 sequences to extract fat regions. Figure 4.1 shows a T1 sequence MRI image without inhomogeneity and its corresponding binary image.

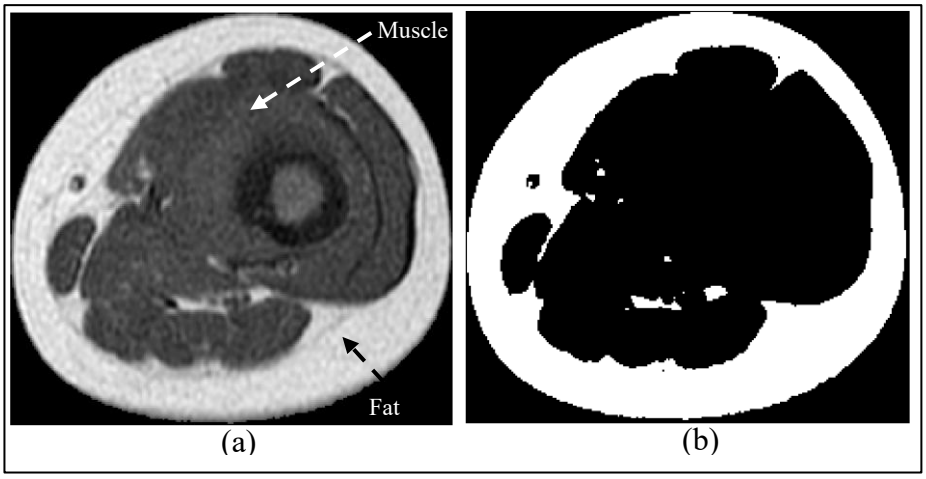

Figure 4.1 (a)T1 Original without Inhomogeneity (b) Binary without Inhomogeneity

In Figure 4.1 (a), the original T1 sequence without intensity inhomogeneity displays a uniform distribution of signal intensity, making it easier to differentiate various tissue types. In T1 sequences, fat appears brighter due to its higher signal intensity, while muscle tissue has a lower intensity and appears darker. Typically, bright signals from fat are observed around the outer edges of the object, as fat tends to surround other structures. Fat covers much of the object, particularly near the skin and between muscle layers. In contrast, muscle tissue is usually encased by fat, with the outer bright regions representing fat and the darker internal areas corresponding to muscle. Figure 4.1 (b) shows the same T1 sequence after being converted into a binary image using global thresholding. Because of the significant difference in signal intensity between fat and other tissues in the T1 sequence, global thresholding effectively isolates fat regions from the background. The clear contrast ensures an accurate binary conversion, precisely delineating fat regions without being affected by intensity inhomogeneity.

In contrast, Figure 4.2 illustrates the MRI image with the present of inhomogeneity and its corresponding binary.

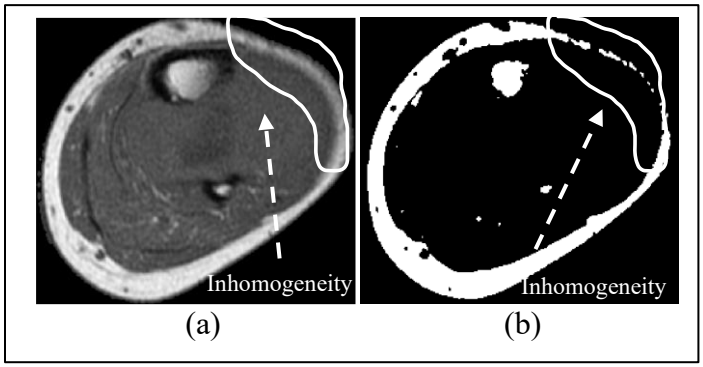

Figure 4.2 (a) T1 Original with Inhomogeneity (b)Binary with Inhomogeneity

Figure 4.2 (a) illustrates the original T1 sequence with the present of inhomogeneity. When inhomogeneity occurs, the intensity levels of the fat, can vary significantly across the image. In the image, the sketch pointed by the arrow indicates regions where intensity inhomogeneity is present. This inhomogeneity causes uneven fat intensity levels within the T1 sequences. Some areas of fat display lower intensity compared to other parts, making their intensity values closer to those of muscle tissue. This inconsistency causes the global thresholding method to incorrectly separate fat and muscle. As a result, regions of fat may be incorrect segmented as muscle, or parts of the muscle may be mistakenly identified as fat, due to the uneven intensity distribution. The regions of inhomogeneity disrupt the uniform segmentation, leading to an incorrect and unreliable binary representation of the fat regions. As shown in the Figure 4.2 (b), these variations prevent the global thresholding from segmenting the fat region effectively. As indicated in the sketch line, the outer fat region appears discontinuously make the fat extraction become incorrect. This is because global thresholding assigns a single intensity value as the threshold, categorizing all pixels above this value as part of the object and those below it as background.

In some regions, fat intensity becomes similar to that of muscle tissue, making it challenging to distinguish between the two during segmentation.

4.1.1 Result of ADSEM Method

In the presence of inhomogeneity, the fat region, which forms the outer layer of the object, becomes disconnected. This disconnection results in a loss of critical information about the fat, making it difficult to segment these regions using the conventional global thresholding method. As explained in Section 4.1, intensity variations caused by inhomogeneity can lead to incorrect segmentations and incomplete

extraction of fat regions. The global thresholding technique struggles with uneven intensity distribution, resulting in mis segmentation and leaving parts of the fat region either unsegmented or incorrectly segmented.

As explained in section 3.3.1, the ADSEM method is proposed to address inhomogeneity. ADSEM dynamically adapts to local intensity variations by utilizing a SE in morphological operations. Figure 4.3 illustrates the graphical flow of the proposed ADSEM method for correcting inhomogeneity. By dynamically adjusting the SE size during processing, ADSEM compensate the effects of inhomogeneity and preserving essential information of fat in T1 sequence for subsequent image processing steps.

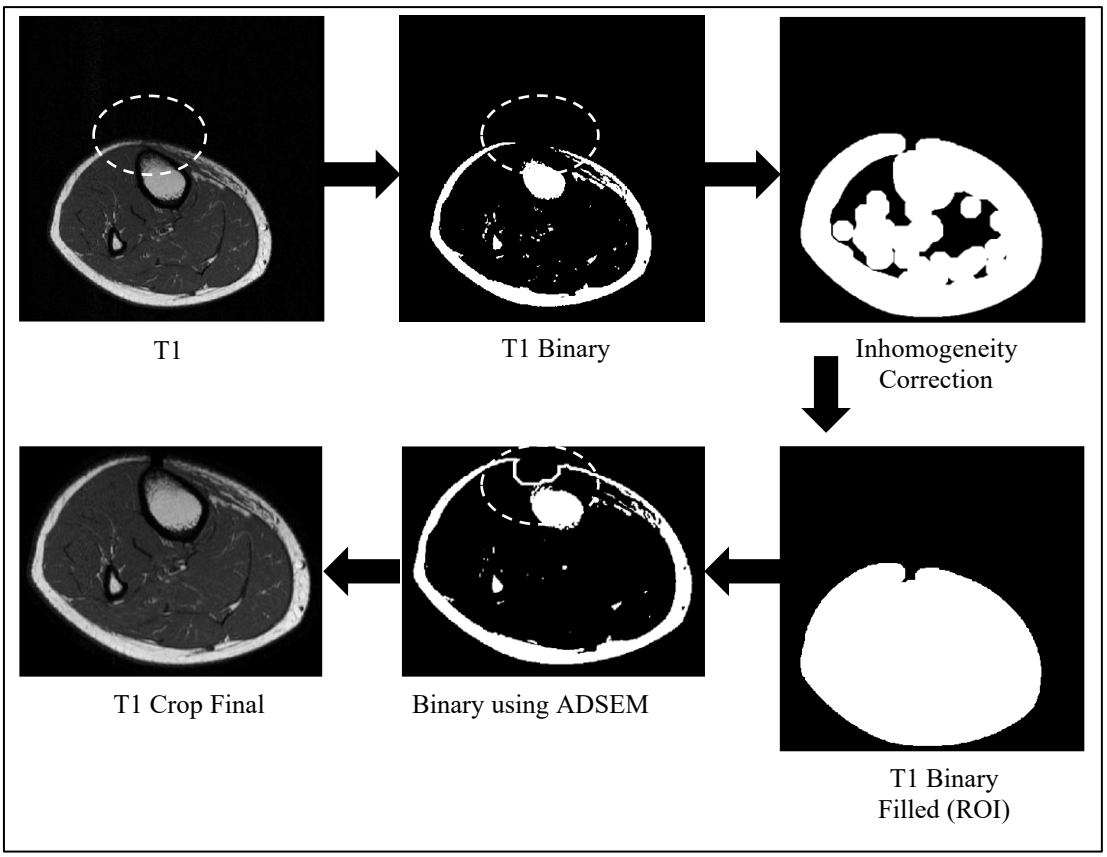

Figure 4.3 Graphical Flow of the Proposed ADSEM

In Figure 4.3, the initial T1 sequence is obtained from data collection that consists of inhomogeneity. The next step is applying global thresholding to convert the T1 sequence into a binary format. Due to inhomogeneity, the fat region outside the structure is discontinued, indicating a loss of fat information in the T1 sequence's binary image, highlighted by the dotted circle. Besides, the presence of inhomogeneity shows the incomplete coverage of the object by fat, causing the algorithm to detect multiple regions within the T1 binary image.

The inhomogeneity correction process involves iteratively applying dilation and filling until the algorithm detects a single connected region in the image, indicating that inhomogeneity has been effectively resolved. As shown in Figure 4.3, this process utilizes morphological dilation with an adaptive disk SE, where the SE size is dynamically adjusted based on the degree of inhomogeneity detected. This adaptive approach enables the algorithm to bridge disconnected regions caused by intensity variations, ensuring a more uniform intensity distribution across the image.

In the T1 sequence's Binary Filled image, the hole-filling process is applied to ensure the continuity of the ROI. The resultant T1 Binary Filled image itself represents the ROI in the T1 sequence. This process is important for eliminating gaps or holes within the segmented fat region, resulting in a complete and connected region. The resulting ROI mask is critical for subsequent steps, as it delineates the regions to be cropped and analyzed further in the necrosis extraction process.

In the binary image using the ADSEM method, the final output shows a fully connected fat region surrounding the structure, as indicated in the circle. To produce this binary image, the process starts by cropping the ADSEM ROI based on the connected region in the image, focusing on the informative area for further analysis. Then, the ROI undergoes morphological erosion using the same SE that was used during the ADSEM process. After erosion, the resulting image is subtracted from the original T1 binary image (before ADSEM), highlighting the outer fat region. This step helps isolate and preserve the outer connected fat layer, ensuring it is accurately identified for use in subsequent processing steps.

Further refinement involves designating the ROI mask as the object while eliminating background noise by setting the corresponding pixels to 0. This step removes irrelevant regions outside the object, as illustrated in the T1 Crop process, labelled as the T1 Crop final in Figure 4.3.

Figure 4.4 presents a comparison of results with and without the application of the ADSEM method for correcting inhomogeneity.

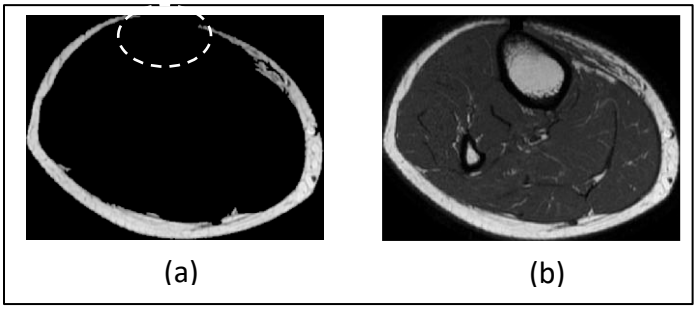

Figure 4.4 (a)T1 Crop Without ADSEM Method (b) T1 Crop Using ADSEM Method

Figure 4.4 (a) illustrates the output from global thresholding method, where the image can be cropped but have lost a lot of information due to discontinue fat region because of inhomogeneity, as indicated by the dotted circle. In contrast, Figure 4.4 (b) shows the T1 sequences can be cropped without having lost of information, and background have been removing to the ROI using the proposed ADSEM method.

4.1.2 Image Registration

As explained in section 3.3.2, image registration is a crucial step in ensuring that all MRI sequences—T1, T2, and T1 GADO sequences—are aligned correctly for accurate analysis and comparison. Incorrectly aligned images can lead to errors in extracting fat tissues and necrotic areas. Misalignment may cause some regions to overlap incorrectly or appear distorted, resulting in inaccurate segmentation and analysis. The T1 sequence original image is used as the reference for image registration. Figure 4.5 illustrates the outcome of image registration, where Figure 4.5(a) and (c) show the T2 and T1 GADO sequences before registration, and Figure 4.5(b) and (d) display the same images after registration.

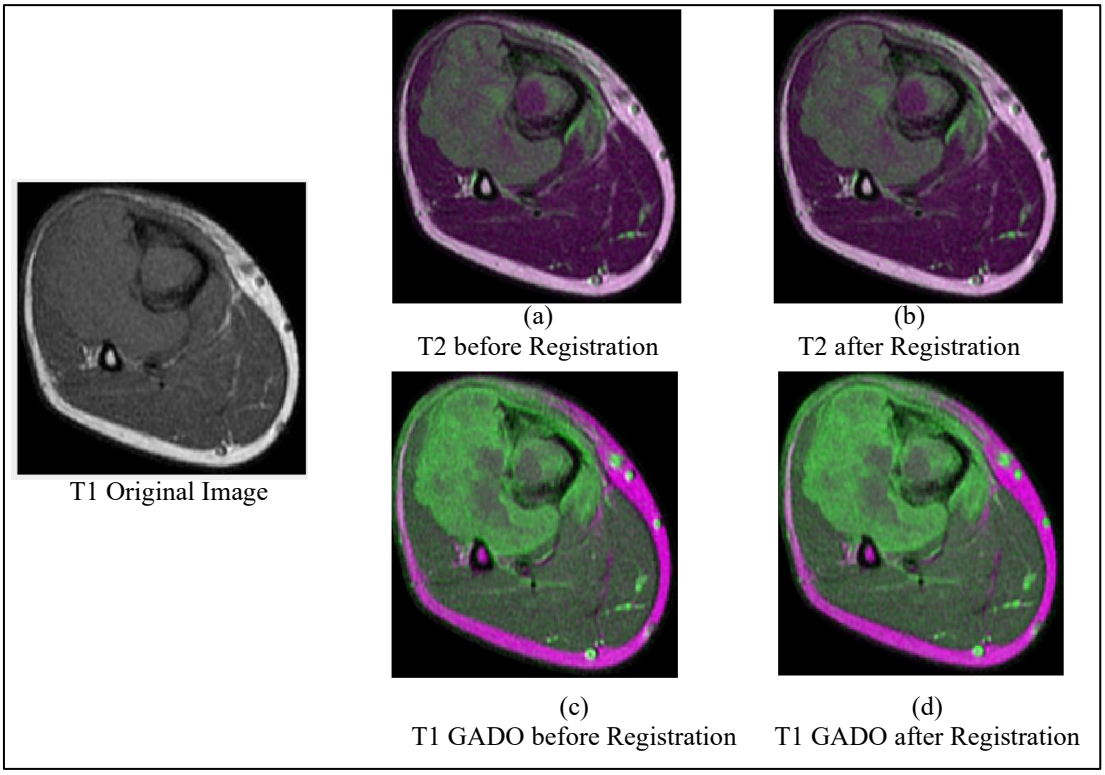

Figure 4.5 The Process of Image Registration

This image registration is to ensure that the anatomical structures are consistently positioned across all sequences, facilitating more accurate detection and comparison of abnormalities.

Figure 4.5 shows no differences between the images before and after registration, indicating that there is minimal or no misalignment between the T1, T2, and T1 GADO sequence images. The red region represents the reference image, which is the T1 sequence, while the green region corresponds to the image being aligned during registration. This outcome suggests that the initial scans were well-aligned.

However, not all the data collected exhibits such high-quality alignment. Figure 4.6 shows that some MRI images in the data collection have poor alignment across sequences.

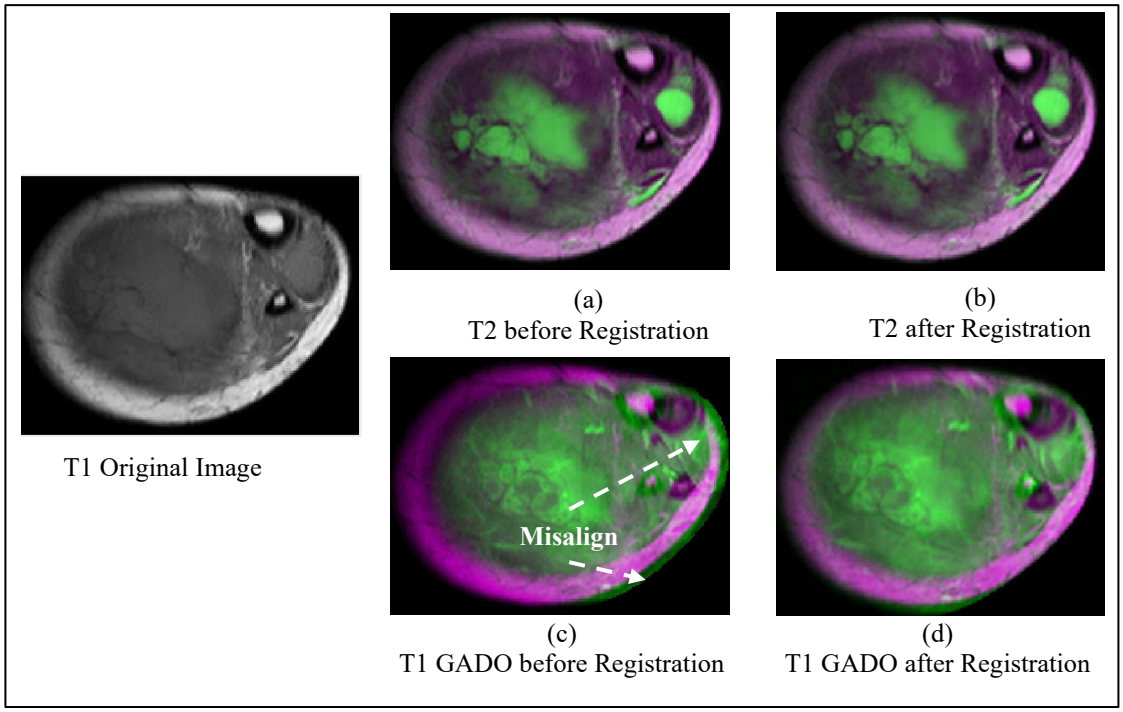

Figure 4.6 Poor Alignment of Image Registration

In Figure 4.6(a) and (b), the T2 sequence shows no misalignment with the T1 reference image, as evidenced by the matching colors before and after registration, indicating a good initial alignment. This is likely because T1 and T2 sequences are acquired within a short time frame, minimizing the chances of movement or positional changes. On the other hand, in Figure 4.6(c), the T1 GADO sequence exhibits a noticeable misalignment when compared to the T1 reference, particularly in the region indicated by the dotted arrow. This misalignment is highly likely due to the additional time required for gadolinium injection before acquiring the T1 GADO images, during which slight patient movement may occur. After the registration process, as shown in Figure 4.6(d), this misalignment is corrected, and both the T1 GADO sequence and T1 sequence are properly aligned. This correction is critical, as any misalignment, especially in T1 GADO sequences, could significantly affect subsequent steps, such as fat extraction and necrosis extraction.

4.1.3 Fat Extraction

As explained in Chapter 3, Section 3.3.3, the fat extraction process plays a critical role in accurately identifying fat regions within the T1 sequences. This process involves two main steps: pre-fat-extraction and image filtering. In the pre-fat-extraction step, the fat regions are primarily extracted by identifying and isolating the highest

intensity regions in the T1 sequence. This step ensures that fat regions are accurately segmented from other tissues, providing a clear foundation for further processing.

The image filtering step then isolates these potential fat regions by applying specific intensity thresholds. As explained in section 3.3.3.2, fat and lesions, which shares lightly similar intensity ranges, are differentiated based on their distinct histogram intensity distribution. This process ensures accurate segmentation by separating fat from lesions and other tissues, addressing the challenges posed by intensity overlaps.

4.1.3.1 Pre-fat Extraction

Figure 4.7 illustrates the visual flow of the result for the pre-fat extraction process, which includes 3 steps; First step consists of two processes which are Create outline and fat region FCM. Second step is arithmetic ADD operation process. Third step consist of two processes which are morphological erode fill process and combining FCM+Outline region with erode fill region using logical AND operation.

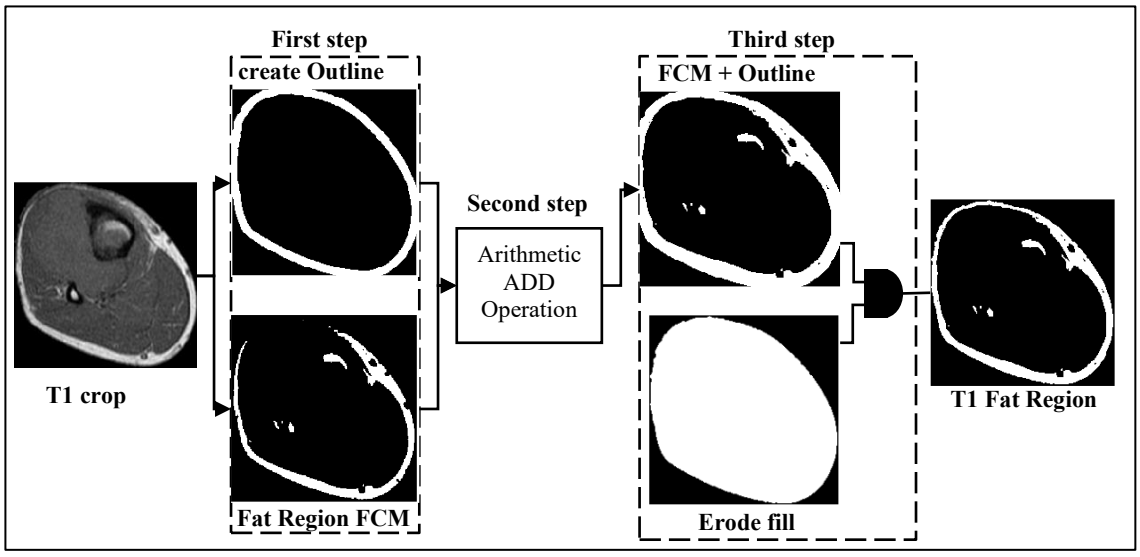

Figure 4.7 Pre-Fat Extraction Process Flow

Figure 4.7 first presents T1 sequences cropped image from ADSEM method used as input for the pre-fat extraction process. The first step involves two sequential operations: creating an outline and applying FCM algorithm on the fat region. The second step involves combining the outcomes from both processes using an arithmetic addition ADD operation.

Figure 4.8 further illustrates the first step process of generating the outline for the fat region.

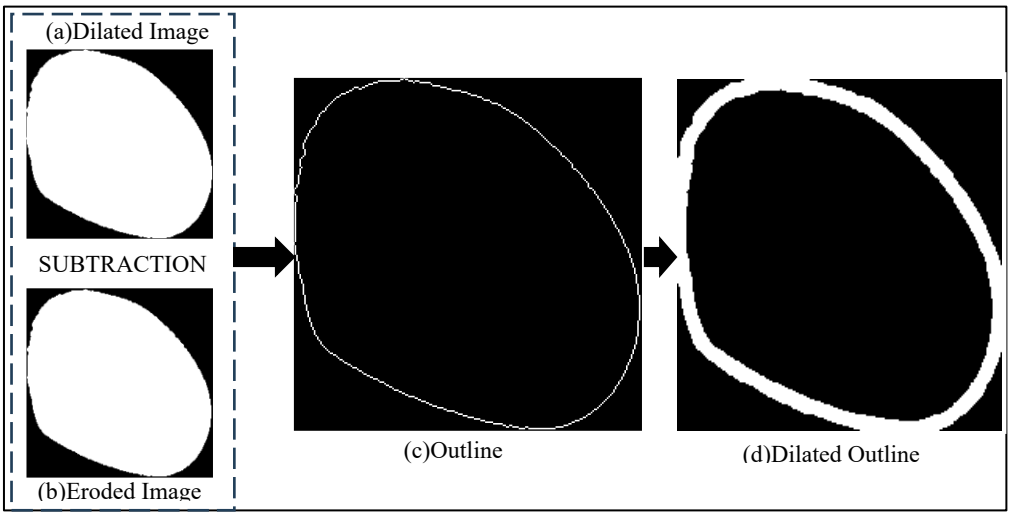

Figure 4.8 Process of Creating Outline

Figure 4.8 (a) shows the dilated image generated from the inhomogeneity correction process using the n-th SE, which is an output of the proposed ADSEM method. Then, using the same n-th SE, the object undergoes erosion, as depicted in Figure 4.8 (b) 'Eroded Image,' shrinking the ROI back to the size of the original object. The SE size is determined adaptively during the ADSEM process, ensuring it is large enough to connect discontinuous regions while avoiding over-dilation. This erosion step refines the object by removing excess boundaries.

The subtraction of the eroded image from the dilated image produces the outline of the ROI, as shown in Figure 4.8(c). This process bridges discontinuities caused by inhomogeneity, ensuring that the fat regions are fully connected. To enhance the outline for integration, it is further thickened using a dilation process. The SE size for this step is selected based on the same SE size used for ADSEM method, ensuring that the outline has adequate thickness for effective merging.

Concurrently, the FCM Algorithm with three clusters is used to extract fat regions from T1 sequences. Figure 4.9 illustrates the output from the FCM algorithm applied to the T1 sequences cropped image, resulting in three distinct clusters: high-intensity regions (representing fat), medium-intensity regions (representing muscle), and low-intensity regions (representing background or other tissue types).

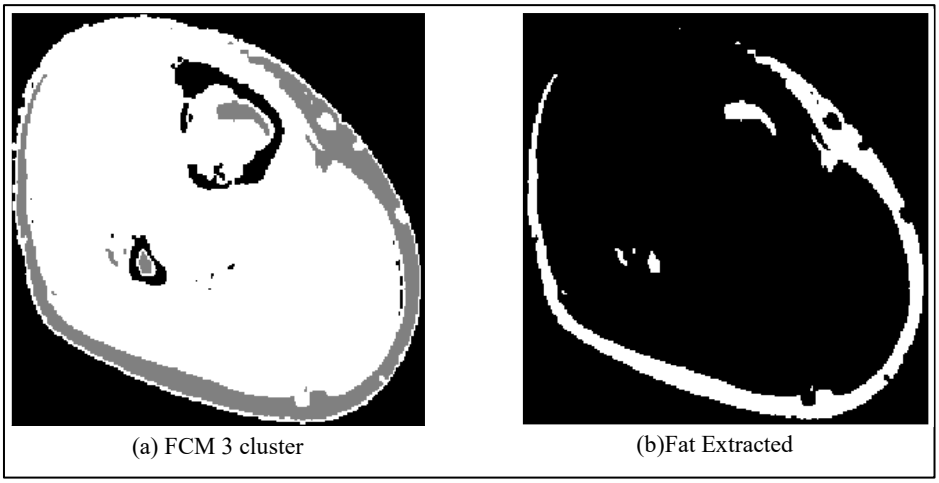

(a) FCM 3 cluster (b)Fat Extracted

Figure 4.9 Result of FCM 3 Clusters

Figure 4.9 (a) shows the initial output from the FCM algorithm, where the high-intensity region represents the fat region. Figure 4.9(b) shows the fat region is extracted.

Second step is including the combination of the identified fat region with the outline created in the "Create Outline" process as in Figure 4.8(d) using an arithmetic ADD operation. Figure 4.10 displays the combined result of Outline and FCM using arithmetic ADD operation.

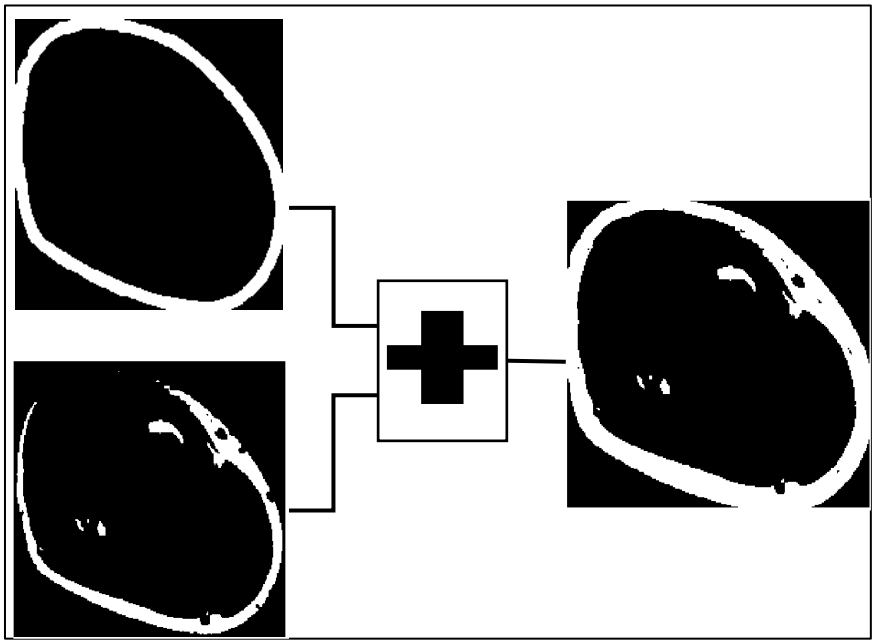

Figure 4.10 The Result of Arithmetic ADD Operation

Figure 4.10 depicts the pre-fat region after combine with the outcome from Figure 4.8 using arithmetic ADD operation. The processes in Figure 4.8 fills the gap between the outline and the FCM-identified fat region, allowing the entire fat region to be represented and preventing any loss of information. This step is crucial for preserving

the integrity of the fat extraction process, allowing all the relevant fat tissue is included for further analysis.

To restore the object to its original size, the image undergoes a logical AND operation with the original size filled binary image to restore it to its original size as shown in Figure 4.11. Third step consist of Logical AND Operation between FCM+Outline region and the eroded fill image from the “Create Outline” process. This step resizes the mask back to its original dimensions, improving the accuracy of pre-fat region extraction. By combining these steps, the FCM+Outline method corrects inhomogeneity and allow extraction of pre-fat regions from MRI images. Figure 4.11 presents the results of the pre-fat extraction process using the ADSEM method.

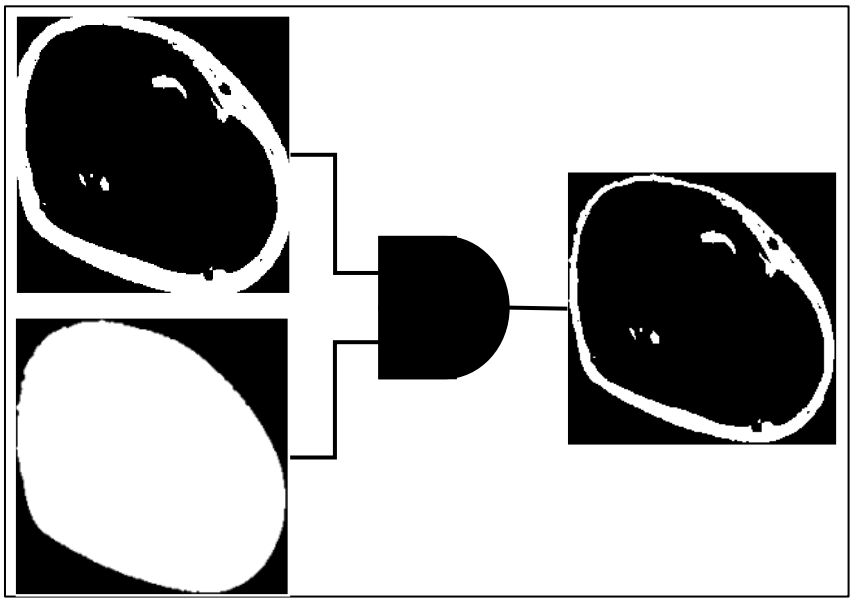

Figure 4.11 Result of Pre-Fat Extraction Process

As shown in Figure 4.11 Result of Pre-Fat Extraction Process, the ADSEM method corrects image inhomogeneity in T1 sequence, ensuring that the extracted pre-fat region fully covers the fat and aligns with the original image.

4.1.3.2 Image Filtering

Image filtering is a crucial process used to refine the extracted fat regions by removing non-fat areas that might have been included due to their similar intensity. As explained in Section 4.1.3.1, the initial pre-fat extraction process may include lesions and other non-fat regions in T1 sequences images, image filtering is applied to isolate

and retain only the true fat regions. This step ensures that only the real fat regions are retained, which is essential for precise necrosis extraction in the next step. As explained in Chapter 3, Section 3.3.3.2, and shown in Figure 3.6, three conditions are applied to isolate true fat regions from the pre-fat regions: (1) excluding regions smaller than 5 pixels, (2) setting an 80% intensity threshold for the fat region in the T1 sequence, and (3)applying a standard deviation filter to retain only consistent fat regions in T1 Gado. These criteria eliminate irrelevant regions and ensure the inclusion of only valid fat areas. Figure 4.12 provides a visual representation of the fat extraction process at different stages, showing both the pre-fat extraction and the final fat extraction after filtrations.

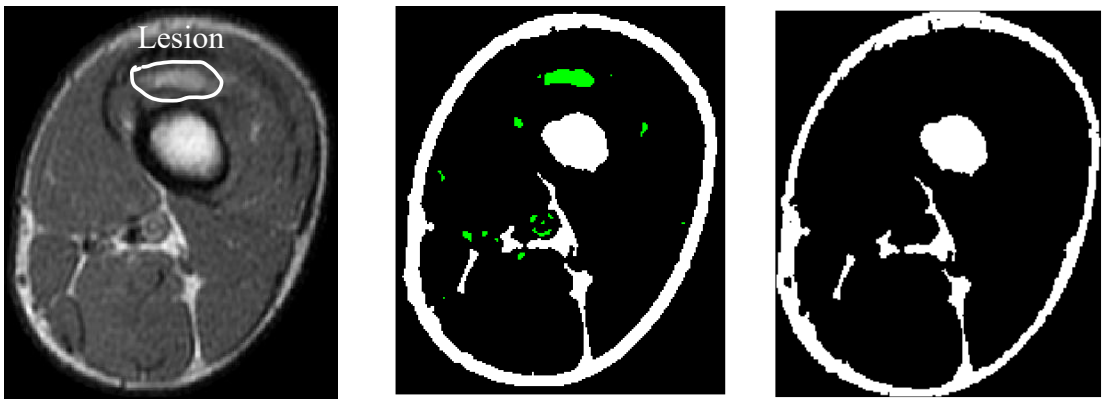

(a)T1 Images (b)Pre-fat image (c)Final Fat after filter

Figure 4.12 The Comparison Between Pre-Fat Region and Final Fat Region After Filtering

Figure 4.12(a) shows the original T1 sequence. The area highlighted with the sketched circle exhibits high intensity similar to fat; due to this intensity similarity, the algorithm has difficulty distinguishing between fat and lesion regions in the pre-fat extraction process. Figure 4.12 (b) shows the pre-fat extracted region, which includes the intended fat areas as well as lesions and non-fat regions, highlighted in green.

Figure 4.12(c) illustrates the final fat extraction after applying image filtering. This process removes small regions, where an area of 5 pixels was set, eliminating regions smaller than this size as they are considered too insignificant for analysis. To distinguish fat from lesions, an 80% intensity threshold based on histogram distribution was applied. This threshold classifies regions with intensity values above 80% of the maximum outer fat intensity as fat, ensuring that only true fat regions are retained.

In addition to intensity filtering, standard deviation filtering was applied, where 60% of the standard deviation from the main fat region, specifically the outer layer, is considered as fat, while the rest is filtered out. By analyzing standard deviation, the algorithm can differentiate true fat regions, which exhibit uniform intensity, from noise or misclassified regions. By employing these filtering techniques, the proposed method removes non-fat regions, thereby enhancing the accuracy of the fat extraction process and ensuring the reliability of further analyses.

4.1.3.3 Performance Evaluation for Fat Extraction

Figure 4.13 presents the results of fat extraction by using the proposed ADSEM method across five slices, displaying the original T1 sequences, ground truth for fat, fat extraction without ADSEM, and the results obtained with the ADSEM method, respectively.

Slice	T1 sequence	Fat Ground Truth	Fat Without ADSEM	Proposed ADSEM
Case 2 Slice 13	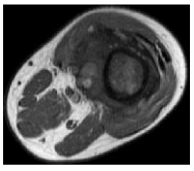		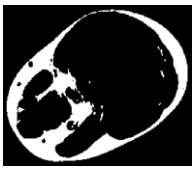	
Case 4 Slice 13	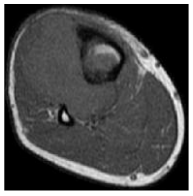			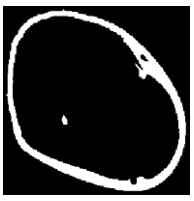
Case 5 Slice 13	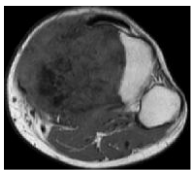	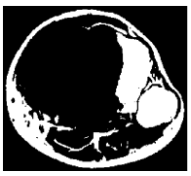	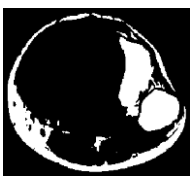	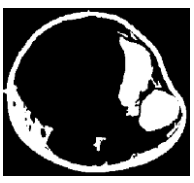
Case 8 Slice 9	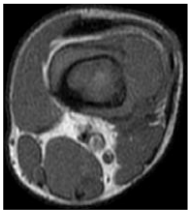	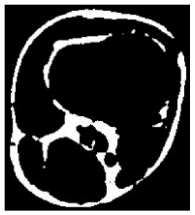		

Case 21 Slice 30	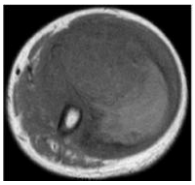	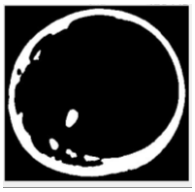		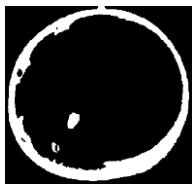

Figure 4.13 Result of Fat Extraction

Figure 4.13 demonstrates that the proposed ADSEM method compensates for inhomogeneity in T1 sequence images, covering the entire fat region and improving fat extraction compared to results without ADSEM.

In Case 2, Slice 13, the ADSEM method produces a refined and complete outline of the fat region, fully covering areas missed in the non-ADSEM extraction. Similarly, in Case 4, Slice 13, ADSEM effectively manages inhomogeneity; without ADSEM, only partial fat extraction is achieved, while ADSEM successfully captures the entire fat region, accommodating intensity variations.

In Case 5, Slice 13, the ADSEM method demonstrates enhanced precision by accurately representing the fat region and excluding adjacent non-fat tissues that the non-ADSEM approach incorrectly includes. Similarly, in Case 8, Slice 9, ADSEM refines extraction boundaries, capturing a continuous, precise outline of the fat region that the non-ADSEM method misses. In Case 21, Slice 30, ADSEM effectively preserves the fat regions and excludes non-fat regions, ensuring the accuracy essential for subsequent analyses.

Figure 4.13 indicates that the ADSEM method is capable of compensating for inhomogeneity in the T1 sequence by defining the boundaries of the ROIs. The ADSEM method corrects inhomogeneity while preserving critical fat information, offering an improved solution for fat extraction essential for subsequent analyses. Table 4.1 presents the performance evaluation of fat extraction across five slices.

Table 4.1
Performance Evaluation for Fat Extraction

Slice	Accuracy	Precision	Recall	F1_score	DSC	IoU
C2 S13	0.9659	0.9077	0.9198	0.9137	0.9137	0.8412
C4 S13	0.9677	0.8386	0.902	0.8691	0.8691	0.7686
C5 S13	0.9492	0.9323	0.8582	0.8937	0.8937	0.8078

C8 S9	0.8812	0.8366	0.6182	0.711	0.8130	0.6849
C21 S30	0.9388	0.9313	0.7474	0.8293	0.8983	0.8153

Table 4.1 shows the performance evaluation analysis of fat extraction techniques. The fat extraction performance across five slices—C2 S13, C4 S13, C5 S13, C8 S9, and C21 S30—is assessed using multiple metrics: Accuracy, Precision, Recall, F1 Score, DSC, and IoU.

Accuracy measures the percentage of correctly identified pixels in the fat region. Among the evaluated slices, Slice C4 S13 achieved the highest accuracy at 0.9677, while Slice C8 S9 had the lowest at 0.8812. The high accuracy in slices such as C4 S13 indicates the method's capability to handle inhomogeneities effectively. The slightly reduced accuracy in C8 S9 reflects the limitations of the ADSEM method in handling severe inhomogeneity, where compensation introduces additional pixels in certain regions, leading to minor over-segmentation and affecting the accuracy.

Precision evaluates the percentage of true fat pixels within the extracted regions, measuring the method's ability to avoid misclassifying non-fat areas as fat. Slices C5 S13 and C21 S30 achieved the highest precision scores of 0.9323 and 0.9313, respectively, indicating minimal inclusion of non-fat regions. Conversely, Slice C8 S9 showed a lower precision of 0.8366. This is not due to misclassification, but rather because the ADSEM method successfully compensated for severe inhomogeneity by connecting disjointed fat regions. While this led to slightly more extracted fat than what was extracted by radiologist-defined ground truth, both the ADSEM result and the ground truth can be considered correct. The difference arises from how inhomogeneity was addressed—ADSEM filled in gaps that were not accounted for in the manual labeling.

Recall measures the model's sensitivity to detect all true fat regions, emphasizing its ability to identify fat without omission. Slice C2 S13 recorded the highest recall score at 0.9198, which means the performance is acceptable in identifying all relevant fat regions. In contrast, Slice C8 S9 had a recall of 0.6182. This lower value is not due to truly missed fat regions, but rather the presence of inhomogeneity in the image. The ADSEM method compensated for the disconnected fat caused by inhomogeneity by reconnecting these regions, resulting in differences from the ground truth, which retained the inhomogeneous gap. Therefore, both the ADSEM output and

the ground truth are valid, and the lower recall reflects this difference in handling inhomogeneity.

The F1 Score, which combines precision and recall, provides a balanced view of the fat extraction method's overall effectiveness. Slice C2 S13 scored the highest F1 score at 0.9137, reflecting its ability to maintain high sensitivity and accurate classification. On the other hand, Slice C8 S9 recorded the lowest F1 score at 0.7110. This is mainly due to its lower recall, influenced by inhomogeneity. Although ADSEM successfully compensated for the disconnected fat regions by reconstructing them, this led to a mismatch with the ground truth created by radiologists, which preserved the inhomogeneous gaps. As a result, the lower F1 score does not necessarily indicate poor performance but highlights differences in how fat continuity was handled.

DSC measures the overlap between the extracted fat regions and the ground truth. Slices C2 S13 and C5 S13 achieved DSC scores of 0.9137 and 0.8937, respectively, demonstrating high alignment with the ground truth. The lowest DSC was observed in Slice C8 S9 at 0.8130. However, this lower score is not necessarily due to extraction inaccuracies. Instead, it reflects the way ADSEM compensated for inhomogeneity by reconstructing disconnected fat regions. While this improved the continuity of fat segmentation, it introduced discrepancies when compared to the ground truth created by radiologists, who preserved the original inhomogeneous appearance. Therefore, both results can be considered correct depending on the interpretation objective—either visual completeness or adherence to the raw image appearance.

IoU provides a measure of overlap between the segmented fat regions and the ground truth. The highest IoU score, 0.8412, was recorded for Slice C2 S13, followed closely by C21 S30 at 0.8153, reflecting precise segmentation. However, Slice C8 S9 achieved the lowest IoU score of 0.6849. This lower score stems not from poor segmentation, but from ADSEM’s correction of inhomogeneity, which reconstructed missing fat regions that were not fully captured in the ground truth. As a result, while the segmentation appears more complete, it differs from the radiologist’s annotation—highlighting a discrepancy due to interpretation style rather than actual performance error.

The analysis of the five slices reveals that the ADSEM method consistently identifies fat regions across most slices. Slices such as C2 S13, C5 S13, and C21 S30 demonstrate robust performance across all metrics. However, the lower performance in

C8 S9 is due to severe inhomogeneity in the T1 sequence image. ADSEM compensated for this by reconnecting disconnected fat regions, which were not fully represented in the radiologist's ground truth. As a result, the segmentation appears more complete, but the metric scores are lower due to differences in annotation rather than actual extraction errors. This highlights the need for better alignment between automated results and ground truth in cases with high inhomogeneity.

Overall, the results validate the strength of the proposed ADSEM method in accurately extracting fat regions, providing a reliable foundation for further segmentation processes while highlighting opportunities for future improvement in challenging cases. Table 4.2 shows the overall performance for fat extraction across 223 images.

Table 4.2
Performance Evaluation for Fat Extraction

Performance	**Accuracy**	**Precision**	**Recall**	**F1 Score**	**DSC**	**IoU**
Average	0.8973	0.8756	0.7076	0.7735	0.8594	0.7727
Median	0.9045	0.9323	0.6926	0.79	0.8975	0.8141
Standard Deviation	0.0447	0.1614	0.0828	0.1111	0.1330	0.1683

Table 4.2 highlights the effectiveness of the ADSEM method for fat extraction across a dataset of 223 MRI slices, The table presents the average, median, and standard deviation values, emphasizing the method's overall effectiveness and consistency in fat extraction.

The average indicates the overall performance of the ADSEM method across all slices. The method achieved an accuracy of 0.8973, demonstrating a consistent ability to correctly classify fat and non-fat pixels. A high precision of 0.8756 reflects the method's effectiveness in minimizing FP and accurately identifying fat regions without including non-fat areas. However, the recall, with a value of 0.7076, highlights challenges in detecting all true fat regions, primarily due to intensity inhomogeneity in the T1 sequence. Inhomogeneity can cause fat signals to appear disconnected or less intense, leading to under-segmentation. The F1 score, combining precision and recall, stands at 0.7735, indicating a balanced approach to identifying true fat regions while minimizing misclassifications. Additionally, the DSC of 0.8594 demonstrates strong

overlap between the segmented and actual fat regions, suggesting effective extraction. Similarly, the IoU score of 0.7727 reflects the segmentation accuracy, showing that most fat regions are correctly segmented despite the presence of intensity inhomogeneities.

The median accuracy of 0.9045 and precision of 0.9323 are higher than their respective averages, emphasizing consistent performance in detecting fat regions without including non-fat areas. However, the median recall, at 0.6926, reflects ongoing challenges in fully capturing all fat regions, particularly in slices affected by intensity inhomogeneity. This inhomogeneity causes some fat pixels to appear disconnected or have lower intensity, making them harder to detect. The F1 score and DSC, with median values of 0.79 and 0.8975, respectively, confirm strong alignment with the ground truth, demonstrating the method's balanced and reliable performance in most slices. Similarly, the median IoU of 0.8141 indicates dependable segmentation across the majority of slices, further validating the method's consistency in preserving true fat regions despite variations in image quality due to inhomogeneity.

The standard deviation highlights the variability in the method's performance across slices. The standard deviation for accuracy is low at 0.0447, indicating consistent performance in distinguishing fat from non-fat regions across slices. However, the higher variability in precision, with a standard deviation of 0.1614, suggests occasional inclusion of non-fat regions, possibly due to intensity inhomogeneities. The standard deviation for recall, at 0.0828, highlights the method’s sensitivity to intensity variations, particularly in challenging slices. Similarly, the F1 score shows moderate variability with a standard deviation of 0.1111, indicating trade-offs between precision and recall in certain cases. Variability in overlap metrics, such as DSC (0.1330) and IoU (0.1683), suggest occasional inconsistencies in segmentation quality, especially in slices with significant intensity variations. These findings indicate that while the method performs well overall, some slices may require further refinement to enhance segmentation reliability.

To sum up, the evaluation in Table 4.2 demonstrates the ADSEM method's reliability and robustness in fat extraction. High accuracy, precision, and overlapping metrics highlight their effectiveness in identifying true fat regions while minimizing errors. However, limitations such as intensity inhomogeneity somehow contribute to lower recall and moderate variability in certain metrics. These challenges present opportunities for further refinement, particularly in capturing all relevant fat pixels in

complex image slices. Overall, the ADSEM method provides a strong foundation for reliable fat region extraction, supporting subsequent segmentation processes effectively.

4.2 Abnormal Extraction

As explained in Chapter 3, Section 3.4.1, the proposed MTFCM method is the integrated method between MT and FCM to extract necrosis. The integration correlates images from T2 and T1 GADO sequences to segment necrotic regions. T2 sequences highlight fluid-rich and hyperintense areas indicative of abnormalities, while T1 GADO sequences provide contrast-enhanced visualization of viable and necrotic tissues.

4.2.1 Result of MTFCM Method

MTFCM serves as an integration method specifically designed to extract necrosis. However, before reaching this step, abnormal region extraction in the T2 sequence is necessary to identify potential necrotic areas. This preliminary step ensures that regions with possible necrosis are detected in the T2 sequence, which are then correlated with T1 GADO for precise necrosis identification.

As explained in section 4.1, this process initiates with fat suppression, wherein the fat region is initially extracted from the T1 sequences. The extracted fat region is subsequently used to suppress the fat signal present in the T2 sequences. The primary aim of this step is to enhance the clarity of visualization for abnormal regions within the T2 sequences by diminishing the fat region's presence. This enables hyperintense areas in the T2 sequences, which may include potential necrosis, to be emphasized for accurate detection and further analysis using the MTFCM method. Figure 4.14 shows the result of the overlayed process into T2 sequences.

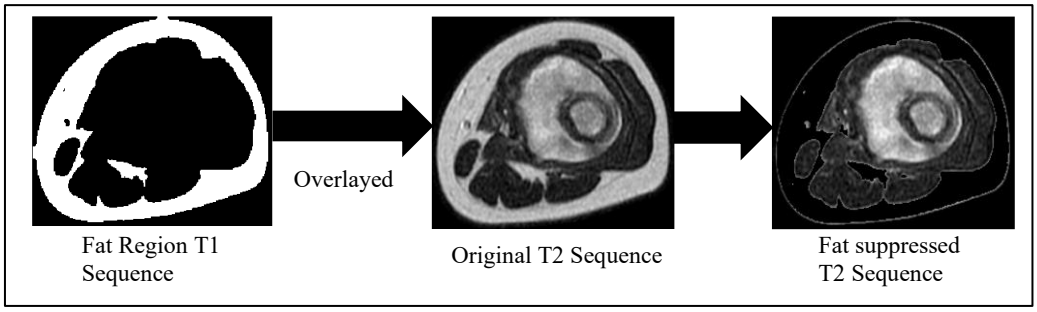

Figure 4.14 The Fat Suppression Process in T2 Sequence

Figure 4.14 illustrates the fat region extracted from the T1 sequences, which is subsequently overlaid onto the original T2 sequences for fat suppression. This step suppresses the fat in the T2 sequence so that the abnormal region is highlighted. After fat suppression, only the abnormal region remains visible. Based on Section 2.3 and Table 2.3, the high-intensity areas in the T2 sequence typically include edema and other abnormalities, with varying intensity levels that may indicate necrotic regions.

Next, the FCM algorithm with three clusters is applied to the fat-suppressed T2 sequence. The three clusters refer to the cortical bone, muscle, and abnormal regions, including potential necrosis regions.

Figure 4.15(a) shows the T2 sequence abnormal region extracted through FCM clustering, categorized into cortical bone, muscle, and abnormal regions. The abnormal region included potential necrosis, which stands out due to its high intensity in the T2 sequence.

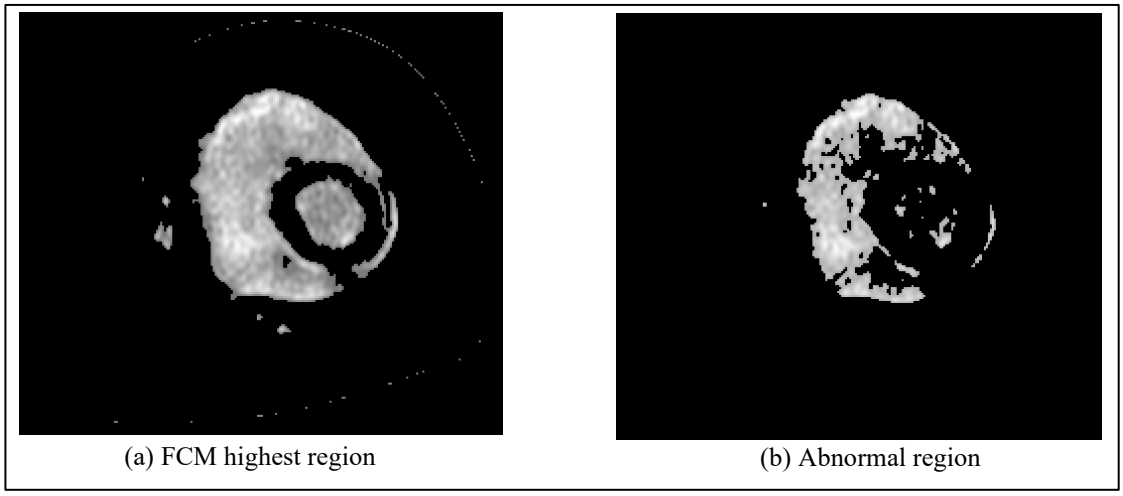

Figure 4.15 The Result of Image Segmentation Process in T2 Sequence..

To refine the segmentation, Figure 4.15(b) demonstrates the use of a two-level MT process, applied to the highest intensity region extracted by FCM. The MT method segments the abnormal region using a high threshold level to extract potential necrotic

areas based on subtle intensity differences. By leveraging MT, the segmentation separating potential necrotic regions from edema or viable tumors.

Thus, the process of identifying potential necrosis regions, initiated by FCM and refined through MT, aims to extract potential necrotic areas from high-intensity tissues in the T2 sequence, leveraging the intensity distinctions as discussed in Table 2.3(Section 2.3).

4.3 Necrosis Extraction

For necrosis extraction, the proposed MTFCM method refines the process by correlating the potential necrotic regions identified in the T2 sequence with the T1 GADO sequence. During this phase, the MTFCM algorithm employs three-level MT to extract necrotic tissue in the T1 GADO sequence.

As explained in section 2.3, Table 2.2, the intensity variations observed in the T1 GADO sequence enable the clear identification of necrotic tissue due to its hypo-intense appearance compared to viable tissues. The three-level MT extracts necrosis by using a low-intermediate threshold to identify the hypo-intense region, which corresponds to necrosis.

Figure 4.16 illustrates this segmentation, showing the necrotic tissue is hypointense and not highlighted, improving clarity and delineation through MT's precise boundary segmentation.

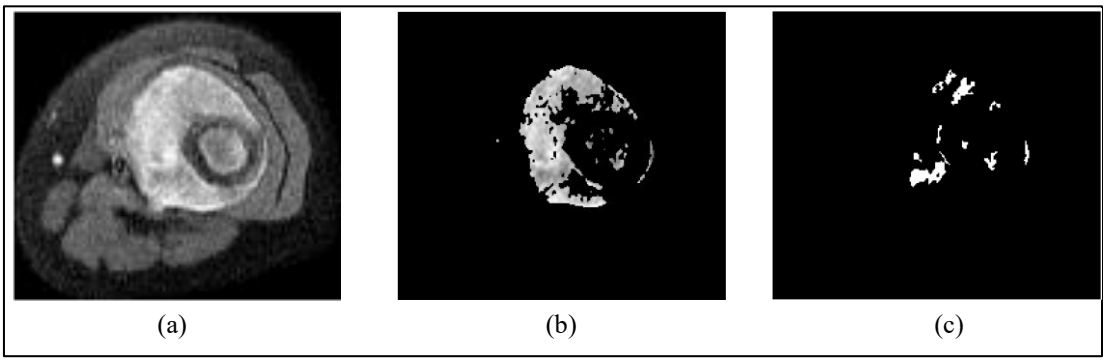

Figure 4.16 (a) T1 GADO Original Sequence (b) Potential Necrosis Region (c) Necrosis Extracted

MT segments necrotic regions based on a low-intermediate pixel intensity distribution, enabling better differentiation of necrotic tissue from surrounding structures. The proposed MTFCM method combines FCM clustering with the MT

approach, leveraging the strengths of both techniques: FCM handles overlapping intensities, while MT enables precise segmentation of distinct regions, such as necrosis.

In Figure 4.16 (a), the original T1 GADO sequence image shows the abnormal region as a hyperintense area. In Figure 4.16(b), the potential necrosis region from section 4.2 abnormal extraction after it is processed with this T1 GADO sequence, revealing that the region consists of both edema (mildly enhanced) and necrosis (with no enhancement). Figure 4.16(c) illustrates the application of MT on the T1 GADO sequences to extract the lowest intensity areas, representing necrotic tissue.

4.4 Performance Evaluation for Necrosis Extraction

As explained in Chapter 3, Section 3.6, the ground truth for necrosis extraction performance evaluation is established by experienced radiologists for each slice in the dataset. The dataset serves as a crucial benchmark for validating the effectiveness of the proposed method. The three-level segmentation in MTFCM extracts potential regions in the T1 GADO sequence, enabling better differentiation of necrotic tissue. To assess performance, this study compares the MTFCM method with a four-cluster FCM approach. The comparison evaluates the accuracy and effectiveness of both methods in distinguishing necrotic regions from other tissues, highlighting their respective strengths and limitations in handling intensity overlaps and segmentation precision.

Figure 4.17 presents a comparative analysis across five slices, displaying the original MRI images in the T1 sequences, T2 sequences, and T1 GADO sequences, alongside the ground truth images, the results of using FCM, and the results obtained using the proposed MTFCM method.

Slice	Original T1	Original T2	Original T1 GADO	Ground Truth	FCM	MTFCM
C2 S13	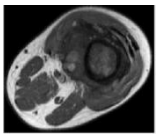	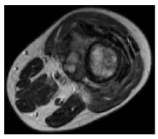	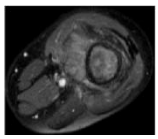		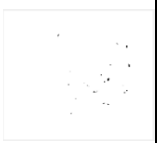	
C9 S18	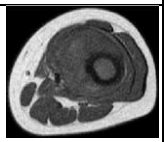	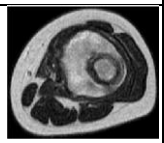	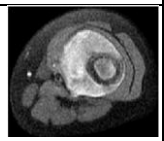		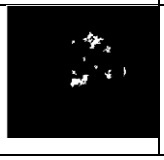	

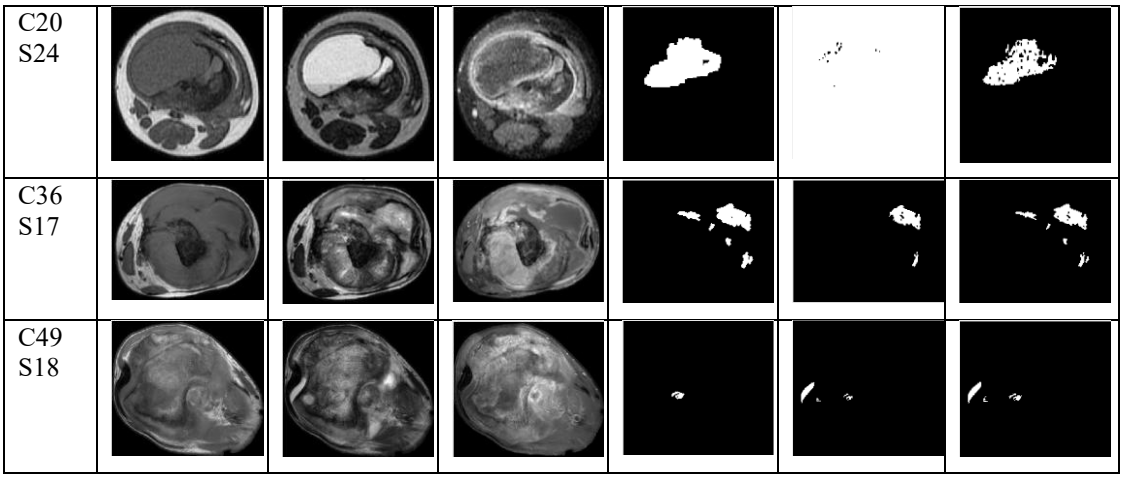

Figure 4.17 The Result of MRI Image Necrosis Extraction

Figure 4.17 illustrates the results of MRI image necrosis extraction for multiple slices using FCM and MTFCM methods compared to the ground truth. Each slice reveals the limitations of FCM and the improved performance of MTFCM.

In slices C2 S13 and C20 S24, FCM shows poor segmentation outcome, leaving gaps and noise. In contrast, MTFCM capturing a more cohesive necrotic region that closely resembles the ground truth. Similarly, in C36 S17, MTFCM successfully extract the necrotic area comprehensively, while FCM omits significant portions.

For slices with faint intensity contrast, such as C36 S17 and C9 S18, FCM struggles to detect the necrotic regions, producing scattered or inaccurate results. MTFCM, however, effectively distinguishes the necrotic tissue from the background, reducing artifacts and enhancing segmentation precision.

Overall, MTFCM outperforms FCM in most of the slices, offering superior segmentation accuracy, reduced noise, and a closer match to the ground truth, making it a more reliable method for necrosis extraction. Table 4.3 presents the detailed performance metrics for five slices in Figure 4.17.

Table 4.3
Performance of 5 Slices Necrosis Extraction

Slices	Method	Accuracy	Precision	Recall	F1_score	DSC	IoU	Process t
C2 S13	FCM	0.2785	0.0164	0.9807	0.0323	0.0239	0.0121	18.1638
	MTFCM	0.9909	0.6091	0.7156	0.6580	0.6580	0.4904	9.2841
C9S18	FCM	0.9907	0.7786	0.6715	0.7211	0.7211	0.5638	14.5419
	MTFCM	0.9924	1.0000	0.5727	0.7283	0.7283	0.5727	8.2485
C20S24	FCM	0.3064	0.1225	0.9924	0.2181	0.1766	0.0969	9.0877
	MTFCM	0.9699	0.9990	0.6918	0.8175	0.8175	0.6913	5.0616
C36S17	FCM	0.9791	1.0000	0.5329	0.6953	0.6953	0.5329	9.2924
	MTFCM	0.9886	1.0000	0.7463	0.8547	0.8547	0.7463	5.9461

C49S18	FCM	0.9926	0.1193	0.2639	0.1643	0.1643	0.0895	36.6713
	MTFCM	0.9926	0.1901	0.5172	0.2780	0.2780	0.1614	17.0068

Overall, MTFCM demonstrates improve performance across most metrics, including accuracy, precision, recall, F1-score, DSC, IoU, and processing time, compared to FCM.

For accuracy, C2 S13 and C20 S24, FCM achieves low accuracy scores of 0.2785 and 0.3064, respectively, compared to MTFCM's 0.9909 and 0.9699. These substantial differences indicate that FCM struggles to extract necrotic regions in these slices likely due to overlapping intensity levels between necrotic, viable tumor, and surrounding tissues. MTFCM, on the other hand, integrates MT and FCM, allowing it to better handle these overlaps by extracting necrotic areas with precision. This integration is particularly beneficial in slices with complex tissue intensity distributions, as seen in C2 S13 and C20 S24, where FCM alone cannot differentiate necrosis from surrounding tissues.

For precision, MTFCM consistently achieves slightly higher precision across most slices, indicating its strength in minimizing FP. However, in C2 S13 and C20 S24, FCM records notably low precision scores of 0.0164 and 0.1225, respectively, while MTFCM achieves 0.6091 and 0.9990. These differences highlight FCM's susceptibility to misclassifying non-necrotic areas as necrotic due to intensity overlaps. MTFCM's MT step adds a process of refinement, effectively filtering out non-necrotic tissues and ensuring more accurate segmentation of necrotic regions, which is evident in its higher precision values.

Recall measures the sensitivity of each method in detecting true necrotic regions. The recall for FCM generally outperforms MTFCM in identifying true necrotic regions, except in C36 S17 and C49 S18. For instance, in C20 S24, FCM achieves a recall of 0.9924 compared to MTFCM's 0.6918, highlighting its sensitivity in detecting necrotic regions. However, this comes at the cost of significant FP, reflected in its lower precision. Conversely, MTFCM excels in C36 S17 with a recall of 0.7463 versus FCM's 0.5329, demonstrating its strength in cases where intensity overlaps are better addressed by MT. The higher recall for FCM across most cases underscores its broad clustering approach, which prioritizes capturing all potential necrotic regions. However, this also increases FP, emphasizing MTFCM's advantage in balancing recall and precision. The

consistent differences illustrate how MTFCM's integration of thresholding improves performance in complex intensity distributions, as seen in C36 S17 and C49 S18.

The F1-score, which balances precision and recall, highlights MTFCM's overall improved performance despite its lower recall in some cases. For instance, in C20 S24 and C36 S17, MTFCM achieves significantly better F1-scores of 0.8175 and 0.8547, compared to FCM's 0.2181 and 0.6953, respectively. These results underscore MTFCM's ability to maintain a balance between accurately identifying necrotic regions and minimizing FP, even when recall alone does not outperform. This balanced approach makes F1-score a more reliable indicator of segmentation effectiveness.

The DSC measures the overlap between the extracted necrotic regions and the ground truth. MTFCM achieves higher DSC scores compared to FCM, such as in C36 S17, where MTFCM records 0.8547 versus FCM's 0.6953. This indicates MTFCM has higher precision in extracting necrotic regions with minimal overlap errors.

The IoU quantifies the accuracy of segmentation overlap. In C36 S17, MTFCM achieves an IoU of 0.7463, outperforming FCM's 0.5329. This improved accuracy highlights MTFCM's effective refinement capabilities through its integration of multilevel thresholding.

Another significant advantage of MTFCM is its faster processing time, completing tasks in half the time or less compared to FCM. For example, in C20 S24, MTFCM completes the segmentation in 5.0616 seconds, whereas FCM takes 9.0877 seconds. This efficiency is due to MTFCM's use of MT, which segments the image based on multiple threshold values, reducing the need for iterative computations. In contrast, FCM relies on repeated clustering iterations, which significantly increases processing time.

The integration of MT and FCM combines the strengths of both techniques. FCM refines ambiguous boundaries between necrotic and non-necrotic tissues, while MT simplifies the input for FCM by segmenting intensity ranges into distinct levels, significantly reducing computational complexity. This integration enhances segmentation performance across high-contrast images which are in T2 sequences and low-contrast images which is T1 GADO sequences, ensuring more accurate and efficient necrosis extraction.

Table 4.4 summarize the performance evaluation results for MTFCM and FCM, including the average for all the matrixes across 223 images.

Table 4.4
Performance Evaluation of All 223 Slices MRI Images

	Mean		Median		Std	
	FCM	MTFCM	FCM	MTFCM	FCM	MTFCM
Accuracy	0.9349	0.9903	0.9926	0.9930	0.1951	0.0095
Precision	0.7537	0.8562	0.9193	0.9579	0.3246	0.2194
Recall	0.6319	0.6230	0.6471	0.6367	0.2007	0.1403
F1 Score	0.6548	0.7157	0.7275	0.7448	0.2208	0.1400
DSC	0.6245	0.7061	0.7231	0.7377	0.2576	0.1618
IoU	0.4966	0.5659	0.5663	0.5844	0.2317	0.1650
Processing Time	16.8310	8.4316	14.6165	6.9324	9.0170	4.2284

Table 4.4 shows that MTFCM consistently outperforms FCM across most performance metrics for necrosis extraction. For accuracy, MTFCM achieves a mean accuracy of 99.03%, compared to FCM's 93.49%, indicating that MTFCM aligns closely with the ground truth and effectively identifies necrotic regions while minimizing errors. FCM's lower accuracy, coupled with its higher standard deviation of 0.1951 compared to MTFCM's 0.0095, suggests that FCM is more prone to inconsistencies across different slices. The lower variability in MTFCM highlights its reliability.

Additionally, the median accuracy of MTFCM which is 99.30% is slightly higher than FCM which is 99.26%, reinforcing its stability across multiple slices. This suggests that MTFCM maintains high segmentation precision in most cases, whereas FCM exhibits greater variation. Similar trends are observed in other metrics, such as precision, F1-score, DSC, and IoU, where MTFCM consistently achieves higher median values, confirming its robustness in necrosis extraction.

For precision, MTFCM has a better mean precision of 85.62%, compared to FCM's 75.37%. This higher precision indicates that MTFCM is more effective in segmenting necrotic regions, particularly around borders where the intensity contrast between necrotic and viable tissue is subtle. By reducing FP, MTFCM improved the

identification of necrotic areas, minimizing the inclusion of adjacent healthy tissue. The slightly higher standard deviation in FCM's precision reflects its tendency to over-segment, potentially resulting in more FP and less accurate segmentation. Additionally, the median precision of MTFCM (95.79%) is higher than FCM (91.93%), further confirming its reliability in consistently segmenting necrotic regions with fewer FP. The narrower range of precision values in MTFCM suggests that it performs more uniformly across different slices, whereas FCM shows greater variability, leading to inconsistent segmentation quality.

For recall, Table 4.4 shows that MTFCM shows a slightly lower mean recall of 62.30% compared to FCM's 63.19%. This small difference reflects MTFCM's focus on minimizing FP rather than capturing every possible region. While this approach ensures more precise segmentation, it may occasionally miss smaller or less distinct necrotic regions that FCM could detect. This trade-off can be beneficial in medical imaging, where FP might lead to unnecessary interventions.

Furthermore, the lower recall in MTFCM could be attributed to the challenges posed by overlapping intensity levels between necrotic and viable tissues. The median recall values for MTFCM (63.67%) and FCM (64.71%) show a similar trend, reinforcing that while MTFCM slightly underperforms in recall, it maintains consistency. However, FCM has a higher standard deviation (0.2007) compared to MTFCM (0.1403), indicating that FCM exhibits more variability across different slices.

For F1 score, which balances precision and recall, Table 4.4 shows that MTFCM achieves a higher mean F1 score of 71.57%, compared to FCM's 65.48%, confirming that MTFCM provides a better overall segmentation performance. Additionally, the median F1 score of MTFCM (0.7448) is slightly higher than FCM's (0.7275), with a narrower interquartile range, indicating greater stability. The lower standard deviation in MTFCM's F1 score (0.1400) compared to FCM (0.2208) further supports its consistency across different slices, making it a more reliable method for necrosis extraction.

For the DSC, Table 4.4 shows the MTFCM achieves 70.61%, outperforming FCM's 62.45%. This higher DSC indicates MTFCM's ability to produce a closer overlap with the ground truth, ensuring more precise necrotic region extraction. MTFCM's lower standard deviation (0.1618) compared to FCM (0.2576) in DSC further highlights its consistency across different imaging conditions.

Regarding IoU, Table 4.4 shows that MTFCM records 56.59%, significantly higher than FCM's 49.66%. This improvement demonstrates MTFCM's accuracy in capturing the true extent of necrotic regions. FCM's higher variability in IoU underscores its less reliable segmentation boundaries in diverse cases. Figure 4.18 shows the boxplot comparison for both methods.

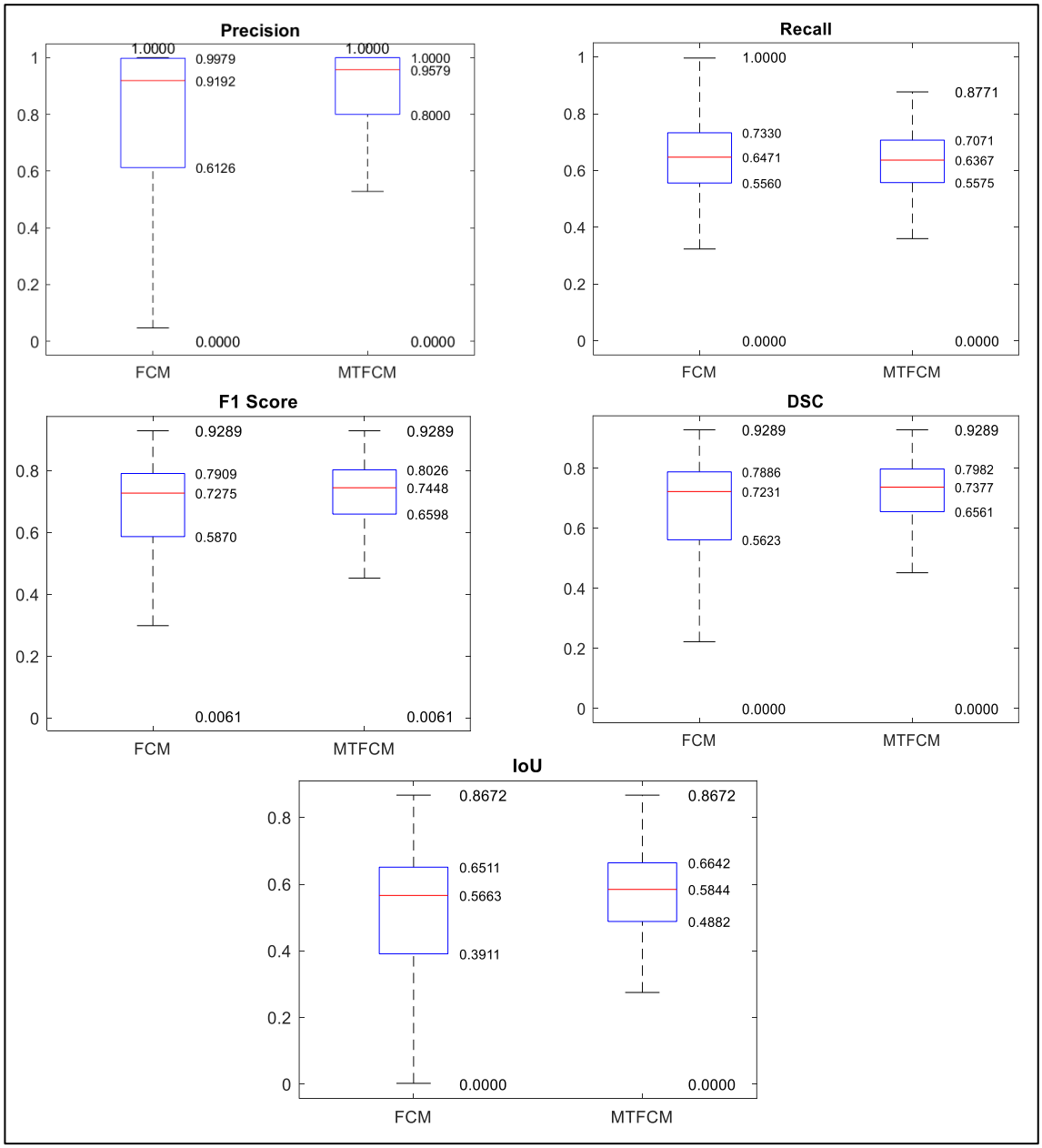

Figure 4.18 Box Plot Analysis

In the precision boxplot, MTFCM demonstrates a narrower interquartile range (IQR) with a median close to 1.000, indicating that its precision values are clustered tightly around the high end, showing exceptional consistency. The upper quartile of MTFCM is also near 1.000, and the lower quartile remains high, indicating that MTFCM rarely dips below a very high precision level. This narrow spread means that

MTFCM consistently avoids FP, which is crucial in necrosis extraction where FP can lead to overestimating the necrotic area.

In contrast, FCM shows a much wider IQR in its precision values, with a significant dip in the lower quartile down to 0.6126. This wider spread and lower precision median (around 0.9192) indicate that FCM is less reliable and has a higher chance of misclassifying non-necrotic tissue as necrotic, leading to more variability and lower accuracy in necrosis detection.

For recall boxplot, MTFCM has a relatively stable median around 0.7071, with an IQR that is narrower compared to FCM. This means that MTFCM's recall values are more consistent, even if the median is slightly lower than FCM's. The upper quartile of MTFCM hovers around 0.8771, while the lower quartile is at 0.5575. This distribution suggests that MTFCM is selective in detecting necrotic areas, which is a trade-off for achieving higher precision. Its recall scores do not reach the extreme maximum of 1.000 like FCM, but this controlled range actually improves reliability by avoiding over-segmentation.

FCM, on the other hand, has a wider recall range with a median closer to 0.7330, suggesting that it occasionally achieves high recall at the expense of precision. Its upper quartile reaches 1.000, but the lower quartile dips to 0.5560, indicating variability and a tendency to capture more regions, potentially including non-necrotic areas. This higher recall but wider spread could lead to FP, which MTFCM mitigates by maintaining a more balanced approach.

Boxplot for the F1 Score shows lower quartile for MTFCM is at 0.6598, while the upper quartile reaches 0.8026. This compact distribution around a higher median show that MTFCM balances precision and recall more consistently across images, delivering reliable segmentation results. FCM has a slightly wider IQR and a lower minimum F1 score 0.5870, which suggests that FCM's balance between precision and recall is less consistent, occasionally dipping in performance. The F1 score distribution's wider spread for FCM implies that it may sometimes struggle to maintain a stable performance, whereas MTFCM's tighter clustering indicates a more dependable overall segmentation quality.

The DSC boxplot for MTFCM reveals a higher and more consistent performance. MTFCM has a median DSC of about 0.7377, with an IQR that spans from around 0.6561 to 0.7982. This indicates that MTFCM achieves a higher overlap with the ground truth compared to FCM in a more stable and predictable manner. The upper

quartile for MTFCM approaches 0.7982, and the lower quartile stays above 0.6561, showing that even in less ideal cases, MTFCM maintains a solid overlap with the actual necrotic regions.

FCM, in contrast, has a slightly lower DSC median at around 0.7231 and a broader range, with the lower quartile extending down to 0.5623. This wider spread implies that FCM occasionally fails to capture the necrotic regions accurately, which reduces its reliability in boundary alignment. The higher consistency of MTFCM, as indicated by the narrower IQR and higher median DSC, suggests that it's better at achieving precise segmentation boundaries, critical in medical imaging where accurate boundary delineation is necessary

In the boxplot of IoU, MTFCM shows median is around 0.5844, with the upper quartile at 0.6642 and the lower quartile at 0.4882. This distribution suggests that MTFCM maintains a higher overlap with the necrotic area, providing a more comprehensive segmentation than FCM. The narrower IQR for MTFCM reflects its ability to consistently capture a high proportion of the target area without excessive overlap errors.

On the other hand, FCM has a slightly lower median IoU at around 0.5663, with a wider spread that includes lower values down to 0.3911 in the lower quartile. This indicates that FCM may sometimes fail to capture the entire necrotic region, leaving gaps that reduce the effectiveness of segmentation. MTFCM's higher median and compact distribution make it more dependable for capturing the true necrotic area, which is critical for accurate medical analysis.

Lastly, MTFCM offers a significant advantage in terms of processing speed, with an average time of 8.43 seconds per slice, compared to FCM's 16.83 seconds. This efficiency makes MTFCM a more practical choice for large datasets or real-time analysis, where speed is essential. The quicker processing time of MTFCM showcasing its optimized algorithm for medical imaging.

Overall, when compared to FCM, MTFCM proves to be the better method across multiple performance metrics. It achieves higher accuracy, improved precision, better overlap with the ground truth as indicated by higher DSC and IoU values, and significantly faster processing times. These advantages make MTFCM more reliable for extracting necrotic regions in medical imaging.

While MTFCM shows slightly lower recall than FCM, this trade-off is acceptable because MTFCM focuses on reducing FP, which improves the overall

reliability of segmentation. Recall refers to the proportion of actual necrotic pixels (TP) that are correctly identified, while precision reflects how many of the identified necrotic pixels are correct (TP / (TP + FP)). A lower recall in MTFCM means that some true necrotic regions may be missed (FN), but by minimizing FP, MTFCM avoids misclassifying surrounding non-necrotic tissues as necrosis. This emphasis on higher precision is especially important in clinical applications, where overestimating necrosis could lead to unnecessary concern or overtreatment.

4.5 Pearson Correlation

The Pearson correlation coefficient was calculated using the equation provided in Chapter 3, Section 3.6.4. Figure 4.19 shows the visual view of the Pearson correlation.

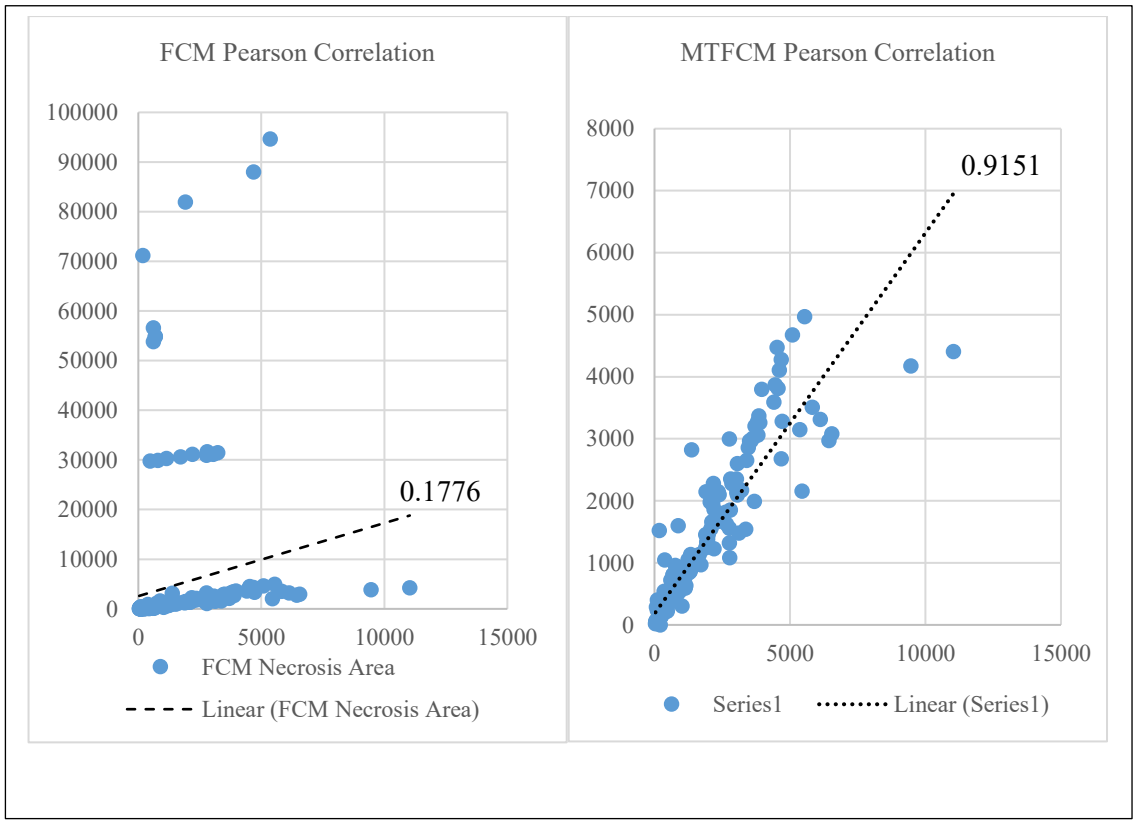

Figure 4.19 Pearson Correlation Between FCM and MTFCM

The analysis reveals that MTFCM achieves a high correlation of 0.9151, indicating a strong linear relationship with the radiologists' ground truth, highlighting its reliability and accuracy in segmenting necrotic regions. In contrast, FCM demonstrates a weak correlation of 0.1776, reflecting its inconsistency and poor alignment with the ground truth. This significant difference in Pearson correlation

confirms that MTFCM provides a more dependable and precise segmentation of necrosis compared to the traditional FCM method.

4.6 Summary

This chapter presented the results of the proposed methods for necrosis extraction from MRI images, focusing on addressing intensity inhomogeneity and enhancing segmentation accuracy. First, the proposed ADSEM method was applied to the T1 sequence to compensate for inhomogeneity. Through adaptive morphological operations using a dynamically sized structural element, the method successfully corrected uneven signal distribution. This correction allowed for accurate fat extraction, ensuring that fat regions were consistently identified across slices.

The quantitative evaluation of the ADSEM method demonstrated high reliability in managing inhomogeneity. The method achieved a mean accuracy of 96.22%, precision of 91.83%, and DSC of 0.7515, confirming its effectiveness in fat region segmentation and its robustness across varying image qualities.

Next, the proposed MTFCM method was introduced, integrating information from the T2 and T1 GADO sequences to extract necrotic tissue. The T2 sequence highlights fluid-rich abnormal regions, while the T1 GADO sequence helps confirm necrosis as hypo-intense areas. MTFCM correlates hyperintense regions in T2 with corresponding hypo-intense regions in T1 GADO, excluding fat regions previously extracted from T1, to isolate necrosis with high precision.

The qualitative evaluation of MTFCM confirmed good alignment with radiologist-defined ground truth. Additionally, quantitative results showed that MTFCM significantly outperformed the traditional FCM approach. MTFCM achieved a mean accuracy of 99.03%, precision of 85.62%, F1 score of 0.7157, and DSC of 0.7061. It also demonstrated improved efficiency, with a reduced mean processing time of 8.43 seconds, compared to 16.83 seconds for FCM.

Overall, while some challenges remain, such as overlapping intensities between necrotic and viable tissues and occasional variations due to image quality, the MTFCM method offers a reliable and efficient approach for necrosis extraction in OS patients. The combined use of ADSEM for preprocessing and MTFCM for segmentation supports more accurate diagnosis and treatment planning.

CHAPTER 5
CONCLUSION

5.1 Conclusion

A tumor necrosis extraction technique for OS in long bones using MRI images has been successfully developed in this study. An ADSEM method was proposed and applied to compensate for intensity inhomogeneity in the T1 sequence, enabling accurate extraction of fat regions. These extracted fat regions were then used to automatically suppress fat in the T2 sequence, enhancing the visibility of abnormal fluid-rich regions. Then, an integrated method known as MTFCM was developed, combining MT and FCM clustering to extract necrotic tissue by correlating hyperintense regions in the T2 sequence with hypo-intense regions in the T1 GADO sequence, while excluding fat identified in the T1 sequence. The performance of both ADSEM and MTFCM methods were evaluated. The ADSEM method demonstrated high accuracy and consistency in fat extraction, while the MTFCM method outperformed conventional FCM with a mean accuracy of 99.03%, precision of 85.62%, and reduced processing time of 8.43 seconds. From a clinical perspective, the proposed automated framework reduces reliance on manual interpretation, minimizes inter-observer variability, and supports objective assessment of tumor necrosis, which is a critical indicator for chemotherapy response and surgical planning in osteosarcoma patients. Overall, this study provides a reliable, automated solution for tumor necrosis detection from MRI images, with strong potential to assist radiologists and clinicians in improving diagnostic confidence and treatment decision-making for OS patients.

5.2 Limitations of The Study

Despite the success of the proposed MTFCM method, several limitations were identified in this study. One of the challenges is the presence of noise, such as salt-and-pepper artifacts in MRI images, which disrupts intensity consistency and impacts segmentation accuracy, particularly when small noise artifacts are misclassified as part of the necrotic region. Additionally, the proposed method is specifically designed for necrosis extraction in long bone regions such as the femur and tibia, and its applicability

to other anatomical sites remains untested. While the MT component significantly reduces computational time compared to traditional FCM, its reliance on histogram-based thresholds may not effectively capture subtle spatial variations, especially in highly complex imaging scenarios. Furthermore, the method was developed and validated using grayscale MRI images collected from a single institution (HUSM), which may limit its generalizability across broader clinical datasets with different imaging protocols or anatomical variations. These limitations highlight the need for further validation and refinement before large-scale clinical deployment.

5.3 Suggestion For Future Work

To further improve the accuracy and robustness of the proposed method, several enhancements can be considered for future research. A key actionable direction is the integration of noise-robust preprocessing techniques, such as adaptive median or hybrid morphological filtering, to mitigate salt-and-pepper noise commonly observed in clinical MRI datasets. Incorporating adaptive thresholding mechanisms that dynamically adjust based on tissue characteristics could further enhance segmentation accuracy and adaptability to different datasets. Another important translational pathway is the integration of the proposed MTFCM framework with deep learning models, such as CNNs, where MTFCM outputs can be used as pre-segmentation or region-proposal inputs to improve learning efficiency and interpretability. Additionally, expanding the study to include 3D MRI data rather than relying solely on 2D slices would provide volumetric necrosis assessment, which is more clinically meaningful for tumor staging and treatment monitoring.

The proposed method could also be extended to investigate necrosis in other skeletal regions beyond long bones to broaden its applicability. To support clinical translation, future work should include multi-center validation using heterogeneous datasets acquired from different MRI scanners and imaging protocols. Lastly, the development of a user-friendly clinical decision support interface that integrates the proposed method into routine radiology workflows could facilitate adoption in real clinical environments. By addressing these areas, the proposed method can be further refined to provide a more effective, scalable, and clinically relevant solution for automated necrosis extraction in osteosarcoma diagnosis and treatment planning.

REFERENCES

[1] S. K. Lee, W. H. Jee, C. K. Jung, S. A. Im, N. G. Chung, and Y. G. Chung, "Prediction of poor responders to neoadjuvant chemotherapy in patients with osteosarcoma: Additive Value of Diffusion-Weighted MRI including Volumetric Analysis to Standard MRI at 3T," *PLoS One*, vol. 15, no. 3, 2020, doi: 10.1371/journal.pone.0229983.

[2] B. A. Lindsey, J. E. Markel, and E. S. Kleinerman, "Osteosarcoma Overview," *Rheumatol. Ther.*, vol. 4, no. 1, pp. 25–43, Jun. 2017, doi: 10.1007/s40744-016-0050-2.

[3] Y. H. Ng, Y. C. Chai, N. Mazli, N. F. Jaafar, and S. Ibrahim, "Outcome of Endoprosthesis used in Limb Salvage Surgery in a Malaysian Orthopaedic Oncology Centre.," *Malaysian Orthop. J.*, vol. 18, no. 1, pp. 60–65, Mar. 2024, doi: 10.5704/MOJ.2403.008.

[4] A. Fonseca *et al.*, "Radiological assessment and outcome of local disease progression after neoadjuvant chemotherapy in children and adolescents with localized osteosarcoma," *J. Clin. Med.*, vol. 9, no. 12, pp. 1–8, Dec. 2020, doi: 10.3390/jcm9124070.

[5] Y. Zhang *et al.*, "Progress in the chemotherapeutic treatment of osteosarcoma," *Oncology Letters*, vol. 16, no. 5. Spandidos Publications, pp. 6228–6237, Nov. 01, 2018. doi: 10.3892/ol.2018.9434.

[6] B. K. K. Fields *et al.*, "Predicting Soft Tissue Sarcoma Response to Neoadjuvant Chemotherapy Using an MRI-Based Delta-Radiomics Approach," *Mol. Imaging Biol.*, vol. 25, no. 4, pp. 776–787, 2023, doi: 10.1007/s11307-023-01803-y.

[7] L. He, H. Yang, and J. Huang, "The tumor immune microenvironment and immune-related signature predict the chemotherapy response in patients with osteosarcoma," *BMC Cancer*, vol. 21, no. 1, pp. 1–13, 2021, doi: 10.1186/s12885-021-08328-z.

[8] C. Kim, L. E. Davis, C. M. Albert, B. Samuels, J. L. Roberts, and M. J. Wagner, "Osteosarcoma in Pediatric and Adult Populations: Are Adults Just Big Kids?," *Cancers*, vol. 15, no. 20. 2023. doi: 10.3390/cancers15205044.

[9] H. C. Beird *et al.*, "Osteosarcoma," *Nat. Rev. Dis. Prim.*, vol. 8, no. 1, p. 77, 2022, doi: 10.1038/s41572-022-00409-y.

[10] E. de la M. del Fémur, “Morphology study of the proximal femur in Malay population,” *Int. J. Morphol*, vol. 29, no. 4, pp. 1321–1325, 2011.

[11] M. Bernstein *et al.*, “Ewing’s Sarcoma Family of Tumors: Current Management,” *Oncologist*, vol. 11, no. 5, pp. 503–519, May 2006, doi: 10.1634/theoncologist.11-5-503.

[12] Y. Yoshioka, D. Siu, and T. D. Cooke, “The anatomy and functional axes of the femur.,” *JBJS*, vol. 69, no. 6, pp. 873–880, 1987.

[13] F. Jafari *et al.*, “Osteosarcoma: A comprehensive review of management and treatment strategies,” *Ann. Diagn. Pathol.*, vol. 49, p. 151654, 2020.

[14] W. Zhu, L. Zhu, Y. Bao, X. Zhong, Y. Chen, and Q. Wu, “Clinical evaluation of neoadjuvant chemotherapy for osteosarcoma,” *J. B.U.ON.*, vol. 24, no. 3, pp. 1181–1185, 2019.

[15] Z. Rguibi, H. Abdelmajid, and D. Zitouni, “Deep Learning in Medical Imaging: A Review,” 2022, pp. 131–144. doi: 10.1201/9781003269793-15.

[16] N. Tajbakhsh, L. Jeyaseelan, Q. Li, J. N. Chiang, Z. Wu, and X. Ding, “Embracing imperfect datasets: A review of deep learning solutions for medical image segmentation.,” *Med. Image Anal.*, vol. 63, p. 101693, Jul. 2020, doi: 10.1016/j.media.2020.101693.

[17] G. Qi, Z. Zhu, K. Li, and H. Xiao, “Advancements and Challenges in Medical Image Segmentation: A Comprehensive Survey,” *Sensors AI*, no. SE-None, Mar. 2025, [Online]. Available: https://www.sciltp.com/journals/sai/article/view/658

[18] Y. Gu, “The Evolution of U-Net Architectures in Medical Image Segmentation,” *ITM Web Conf.*, vol. 73, 2025, [Online]. Available: https://doi.org/10.1051/itmconf/20257302019

[19] X. Jiang, “Trends and Techniques in Medical Image Segmentation for Disease Detection,” *ITM Web Conf.*, vol. 73, 2025, [Online]. Available: https://doi.org/10.1051/itmconf/20257302030

[20] A. Priya, R. K. Agrawal, and B. Rana, “Fusion-based Multilevel Thresholding For Image Segmentation Using Evolutionary Algorithm,” in *2022 IEEE 9th Uttar Pradesh Section International Conference on Electrical, Electronics and Computer Engineering (UPCON)*, 2022, pp. 1–7. doi: 10.1109/UPCON56432.2022.9986438.

[21] C. Thévenin-Lemoine *et al.*, “Planning for bone excision in ewing sarcoma

post-Chemotherapy MRI more accurate than pre-Chemotherapy MRI assessment," *J. Bone Jt. Surg. - Am. Vol.*, vol. 100, no. 1, pp. 13–20, 2018, doi: 10.2106/JBJS.16.01461.

[22] S. Jetley *et al.*, "Tumor histopathological response to neoadjuvant chemotherapy in bone sarcomas: A single-institutional experience," *Int. J. Heal. Allied Sci.*, vol. 9, no. 3, p. 240, 2020, doi: 10.4103/ijhas.ijhas_119_19.

[23] S. Xin and G. Wei, "Prognostic factors in osteosarcoma: A study level meta-analysis and systematic review of current practice," *J. Bone Oncol.*, vol. 21, no. February, p. 100281, 2020, doi: 10.1016/j.jbo.2020.100281.

[24] J. Zhong *et al.*, "Automated prediction of the neoadjuvant chemotherapy response in osteosarcoma with deep learning and an MRI-based radiomics nomogram," *Eur. Radiol.*, vol. 32, no. 9, pp. 6196–6206, 2022, doi: 10.1007/s00330-022-08735-1.

[25] E. J. Inarejos Clemente *et al.*, "Multiparametric MRI evaluation of bone sarcomas in children," *Insights Imaging*, vol. 13, no. 1, p. 33, 2022.

[26] R. Mandava, O. M. d. Alia, B. C. Wei, D. Ramachandram, M. E. Aziz, and I. L. Shuaib, "Osteosarcoma segmentation in MRI using dynamic harmony search based clustering," *Proc. 2010 Int. Conf. Soft Comput. Pattern Recognition, SoCPaR 2010*, no. September 2014, pp. 423–429, 2010, doi: 10.1109/SOCPAR.2010.5686624.

[27] S. K. Lee, W.-H. Jee, C. K. Jung, S. A. Im, N.-G. Chung, and Y.-G. Chung, "Prediction of poor responders to neoadjuvant chemotherapy in patients with osteosarcoma: additive value of diffusion-weighted MRI including volumetric analysis to standard MRI at 3T," *PLoS One*, vol. 15, no. 3, p. e0229983, 2020.

[28] S. Saman and S. J. Narayanan, "Active contour model driven by optimized energy functionals for MR brain tumor segmentation with intensity inhomogeneity correction," *Multimed. Tools Appl.*, vol. 80, no. 14, pp. 21925–21954, 2021, doi: 10.1007/s11042-021-10738-x.

[29] C. Feng, W. Li, J. Hu, K. Yu, and D. Zhao, "BCEFCM_S: Bias correction embedded fuzzy c-means with spatial constraint to segment multiple spectral images with intensity inhomogeneities and noises," *Signal Processing*, vol. 168, p. 107347, 2020, doi: https://doi.org/10.1016/j.sigpro.2019.107347.

[30] C. Feng, J. Yang, C. Lou, W. Li, K. Yu, and D. Zhao, "A Global Inhomogeneous Intensity Clustering-(GINC-) Based Active Contour Model for

Image Segmentation and Bias Correction," *Comput. Math. Methods Med.*, vol. 2020, no. 1, p. 7595174, 2020.

[31] V. Venkatesh, N. Sharma, and M. Singh, "Intensity inhomogeneity correction of MRI images using InhomoNet," *Comput. Med. Imaging Graph.*, vol. 84, Sep. 2020, doi: 10.1016/j.compmedimag.2020.101748.

[32] L. He, H. Yang, and J. Huang, "The tumor immune microenvironment and immune-related signature predict the chemotherapy response in patients with osteosarcoma," *BMC Cancer*, vol. 21, no. 1, p. 581, 2021, doi: 10.1186/s12885-021-08328-z.

[33] D. J. Ho *et al.*, "Deep Interactive Learning: An Efficient Labeling Approach for Deep Learning-Based Osteosarcoma Treatment Response Assessment," *Lect. Notes Comput. Sci. (including Subser. Lect. Notes Artif. Intell. Lect. Notes Bioinformatics)*, vol. 12265 LNCS, pp. 540–549, 2020, doi: 10.1007/978-3-030-59722-1_52.

[34] R. Hao, K. Namdar, L. Liu, M. A. Haider, and F. Khalvati, "A Comprehensive Study of Data Augmentation Strategies for Prostate Cancer Detection in Diffusion-Weighted MRI Using Convolutional Neural Networks," *J. Digit. Imaging*, vol. 34, no. 4, pp. 862–876, 2021, doi: 10.1007/s10278-021-00478-7.

[35] H. Mzoughi *et al.*, "Deep Multi-Scale 3D Convolutional Neural Network (CNN) for MRI Gliomas Brain Tumor Classification," *J. Digit. Imaging*, vol. 33, no. 4, pp. 903–915, 2020, doi: 10.1007/s10278-020-00347-9.

[36] S. Jardim, J. António, and C. Mora, "Image thresholding approaches for medical image segmentation - short literature review," *Procedia Comput. Sci.*, vol. 219, pp. 1485–1492, 2023, doi: https://doi.org/10.1016/j.procs.2023.01.439.

[37] C. S. Rao and K. Karunakara, "A comprehensive review on brain tumor segmentation and classification of MRI images," *Multimed. Tools Appl.*, vol. 80, no. 12, pp. 17611–17643, 2021, doi: 10.1007/s11042-020-10443-1.

[38] M. K. Naik, R. Panda, L. Samantaray, and A. Abraham, "A novel threshold score based multiclass segmentation technique for brain magnetic resonance images using adaptive opposition slime mold algorithm," *Int. J. Imaging Syst. Technol.*, vol. 32, no. 4, pp. 1397–1413, 2022.

[39] A. S U and A. Abraham, "A Review on state-of-the-art techniques for image segmentation and classification for brain MR images," *Curr. Med. Imaging*,

vol. 19, no. 3, pp. 243–270, 2023.

[40] R. R. Mostafa, N. E. El-Attar, S. F. Sabbeh, A. Vidyarthi, and F. A. Hashim, "ST-AL: a hybridized search based metaheuristic computational algorithm towards optimization of high dimensional industrial datasets," *Soft Comput.*, vol. 27, no. 18, pp. 13553–13581, 2023, doi: 10.1007/s00500-022-07115-7.

[41] A. Kamsyakawuni, M. P. Sari, A. Riski, and K. A. Santoso, "Metaheuristic algorithm approach to solve non-linear equations system with complex roots," *J. Phys. Conf. Ser.*, vol. 1494, no. 1, p. 12001, 2020, doi: 10.1088/1742-6596/1494/1/012001.

[42] N. Otsu, "A Threshold Selection Method from Gray-Level Histograms," *IEEE Trans. Syst. Man. Cybern.*, vol. 9, no. 1, pp. 62–66, 1979, doi: 10.1109/TSMC.1979.4310076.

[43] M. T. Nyo, F. Mebarek-Oudina, S. S. Hlaing, and N. A. Khan, "Otsu's thresholding technique for MRI image brain tumor segmentation," *Multimed. Tools Appl.*, vol. 81, no. 30, pp. 43837–43849, 2022, doi: 10.1007/s11042-022-13215-1.

[44] L. Xiao, C. Fan, H. Ouyang, A. F. Abate, and S. Wan, "Adaptive trapezoid region intercept histogram based Otsu method for brain MR image segmentation," *J. Ambient Intell. Humaniz. Comput.*, vol. 13, no. 4, pp. 2161–2176, 2022, doi: 10.1007/s12652-021-02976-6.

[45] U. K. Malviya, "Tumor Detection in MRI Images using Modified Multi-level Otsu Thresholding (MLOT) and Cross-Correlation of Principle Components," in *2020 Fourth International Conference on Computing Methodologies and Communication (ICCMC)*, 2020, pp. 126–131. doi: 10.1109/ICCMC48092.2020.ICCMC-00026.

[46] M. Xu *et al.*, "Research on Fast Multi-Threshold Image Segmentation Technique Using Histogram Analysis," *Electronics*, vol. 12, no. 21. 2023. doi: 10.3390/electronics12214446.

[47] E. Baidya Kayal, D. Kandasamy, R. Sharma, M. C. Sharma, S. Bakhshi, and A. Mehndiratta, "SLIC-supervoxels-based response evaluation of osteosarcoma treated with neoadjuvant chemotherapy using multi-parametric MR imaging," *Eur. Radiol.*, vol. 30, no. 6, pp. 3125–3136, Jun. 2020, doi: 10.1007/s00330-019-06647-1.

[48] S. Wang, H. Jia, and X. Peng, "Modified salp swarm algorithm based

multilevel thresholding for color image segmentation," *Math. Biosci. Eng.*, vol. 17, no. 1, pp. 700–724, 2020, doi: 10.3934/mbe.2020036.

[49] S. Prasath and D. K. Rani, "Cystic Region Detection Using Hybrid Fuzzybased Multi-Region Normalization," *Int. J. Eng. Manuf.*, vol. 12, no. 1, pp. 29–36, 2022, doi: 10.5815/ijem.2022.01.03.

[50] Y. Jiang, D. Zhang, W. Zhu, and L. Wang, "Multi-Level Thresholding Image Segmentation Based on Improved Slime Mould Algorithm and Symmetric Cross-Entropy," *Entropy*, vol. 25, no. 1. 2023. doi: 10.3390/e25010178.

[51] D. Koundal, V. Kadyan, P. Dutta, V. Anand, S. Aggarwal, and S. Gupta, "1 - Computational techniques in biomedical image analysis: overview," D. Koundal and S. B. T.-A. in C. T. for B. I. A. Gupta, Eds., Academic Press, 2020, pp. 3–31. doi: https://doi.org/10.1016/B978-0-12-820024-7.00001-3.

[52] M. Vanitha, "Automatic Osteosarcoma Classification System Based Multilayer Grid XG Boost Architecture," 2022.

[53] J. F. C. Kingman, "G. Matheron, random sets and integral geometry," 1975.

[54] P. Rangne, P. R. M. Bhombe, and P. A. S. Welankiwar, "Brain Tumor Extraction from MRI Images Using MATLAB," *Int. J. Innov. Sci. Res. Technol.*, vol. 5, no. 9, pp. 436–439, 2020, doi: 10.38124/ijisrt20sep102.

[55] S. C. Huang *et al.*, "An advanced noise reduction and edge enhancement algorithm," *Sensors*, vol. 21, no. 16, pp. 1–12, 2021, doi: 10.3390/s21165391.

[56] L. Fan, F. Zhang, H. Fan, and C. Zhang, "Brief review of image denoising techniques," *Vis. Comput. Ind. Biomed. Art*, vol. 2, no. 1, p. 7, 2019, doi: 10.1186/s42492-019-0016-7.

[57] M. R. Canales-Fiscal and J. G. Tamez-Peña, "Hybrid morphological-convolutional neural networks for computer-aided diagnosis.," *Front. Artif. Intell.*, vol. 6, p. 1253183, 2023, doi: 10.3389/frai.2023.1253183.

[58] L. Hua, Y. Gu, X. Gu, J. Xue, and T. Ni, "A Novel Brain MRI Image Segmentation Method Using an Improved Multi-View Fuzzy c-Means Clustering Algorithm," *Front. Neurosci.*, vol. 15, Mar. 2021, doi: 10.3389/fnins.2021.662674.

[59] M. N. Ahmed, S. M. Yamany, N. Mohamed, A. A. Farag, and T. Moriarty, "A modified fuzzy C-means algorithm for bias field estimation and segmentation of MRI data," *IEEE Trans. Med. Imaging*, vol. 21, no. 3, pp. 193–199, 2002, doi: 10.1109/42.996338.

[60] M. A. Balafar, “Fuzzy C-mean based brain MRI segmentation algorithms,” *Artif. Intell. Rev.*, vol. 41, no. 3, pp. 441–449, 2014, doi: 10.1007/s10462-012-9318-2.

[61] S. Chen and D. Zhang, “Robust image segmentation using FCM with spatial constraints based on new kernel-induced distance measure,” *IEEE Trans. Syst. Man, Cybern. Part B Cybern.*, vol. 34, no. 4, pp. 1907–1916, 2004, doi: 10.1109/TSMCB.2004.831165.

[62] C. Wang, W. Pedrycz, Z. Li, and M. Zhou, “Residual-driven Fuzzy C-Means Clustering for Image Segmentation,” *IEEE/CAA J. Autom. Sin.*, vol. 8, no. 4, pp. 876–889, 2021, doi: 10.1109/JAS.2020.1003420.

[63] Q. Wang, X. Wang, C. Fang, and W. Yang, “Robust fuzzy c-means clustering algorithm with adaptive spatial & intensity constraint and membership linking for noise image segmentation,” *Appl. Soft Comput.*, vol. 92, p. 106318, 2020, doi: https://doi.org/10.1016/j.asoc.2020.106318.

[64] M. Mohammdian-khoshnoud, A. R. Soltanian, A. Dehghan, and M. Farhadian, “Optimization of fuzzy c-means (FCM) clustering in cytology image segmentation using the gray wolf algorithm,” *BMC Mol. Cell Biol.*, vol. 23, no. 1, p. 9, 2022, doi: 10.1186/s12860-022-00408-7.

[65] Y. Tang, F. Ren, and W. Pedrycz, “Fuzzy C-Means clustering through SSIM and patch for image segmentation,” *Appl. Soft Comput. J.*, vol. 87, p. 105928, 2020, doi: 10.1016/j.asoc.2019.105928.

[66] M. Kass, A. Witkin, and D. Terzopoulos, “Snakes: Active contour models,” *Int. J. Comput. Vis.*, vol. 1, no. 4, pp. 321–331, 1988, doi: 10.1007/BF00133570.

[67] C. Xu and J. L. Prince, “Snakes, shapes, and gradient vector flow,” *IEEE Trans. Image Process.*, vol. 7, no. 3, pp. 359–369, 1998, doi: 10.1109/83.661186.

[68] Kr. Babu, Ksony, Nd. Indira, K. Vara Prasad, and S. Shameem, “An Effective Brain Tumor Detection from T1w MR Images Using Active Contour Segmentation Techniques,” *J. Phys. Conf. Ser.*, vol. 1804, no. 1, p. 12174, 2021, doi: 10.1088/1742-6596/1804/1/012174.

[69] Z. Shahvaran, K. Kazemi, M. Fouladivanda, M. S. Helfroush, O. Godefroy, and A. Aarabi, “Morphological active contour model for automatic brain tumor extraction from multimodal magnetic resonance images,” *J. Neurosci. Methods*, vol. 362, p. 109296, 2021, doi: https://doi.org/10.1016/j.jneumeth.2021.109296.

[70] N. Alipour and R. Hasanzadeh, “Superpixel-based brain tumor segmentation in MR images using an extended local fuzzy active contour model,” *Multimed. Tools Appl.*, vol. 80, pp. 1–25, Mar. 2021, doi: 10.1007/s11042-020-10122-1.

[71] A. Fonseca *et al.*, “Radiological Assessment and Outcome of Local Disease Progression after Neoadjuvant Chemotherapy in Children and Adolescents with Localized Osteosarcoma.,” *J. Clin. Med.*, vol. 9, no. 12, Dec. 2020, doi: 10.3390/jcm9124070.

[72] L. Atikah, N. A. Hasanah, R. Sarno, A. Fajar, and D. Rahmawati, “Brain Segmentation using Adaptive Thresholding, K-Means Clustering and Mathematical Morphology in MRI Data,” in *2020 International Seminar on Application for Technology of Information and Communication (iSemantic)*, 2020, pp. 161–167. doi: 10.1109/iSemantic50169.2020.9234303.

[73] K. Hajdowska, S. Student, and D. Borys, “Graph based method for cell segmentation and detection in live-cell fluorescence microscope imaging,” *Biomed. Signal Process. Control*, vol. 71, p. 103071, 2022.

[74] J. Mehena, “Medical Image Edge Detection Using Modified Morphological Edge Detection Approach,” *Int. J. Comput. Sci. Eng.*, vol. 7, Jun. 2019, doi: 10.26438/ijcse/v7i6.523528.

[75] K. Thiruvenkadam, S. Padmanaban, and S. Karuppanagounder, *Morphological Operations by Parallel Processing using GPU-CUDA Model*. 2015.

[76] X. Liu, J. Fan, and Z. Chen, “Improved fuzzy C-means algorithm based on density peak,” *Int. J. Mach. Learn. Cybern.*, vol. 11, Mar. 2020, doi: 10.1007/s13042-019-00993-8.

APPENDICES

APPENDIX

Jawatankuasa Etika
Penyelidikan Manusia USM (JEPeM)

Human Research Ethics Committee USM (HREC)

Universiti Sains Malaysia
Kampus Kesihatan
16150 Kubang Kerian, Kelantan, Malaysia.
Tel. : +609 - 767 3000/2354/2362
Fax. : + 609 - 767 2351
Email : jepem@usm.my
Laman Web : www.jepem.kk.usm.my
www.usm.my

5th December 2022

Mr. Mohamad Haizan Othman
Universiti Teknologi MARA (UiTM)
Cawangan Pulau Pinang
13500 Permatang Pauh
Pulau Pinang.

JEPeM Code : USM/JEPeM/22060378
Protocol Title: Formulation of Region-Edge Based Feature Extraction Method for Tumor Necrosis Extraction from Osteosarcoma MRI Images.

Dear Mr.,

We wish to inform you that your study protocol has been reviewed and is hereby granted approval for implementation by the Jawatankuasa Etika Penyelidikan Manusia Universiti Sains Malaysia (JEPeM-USM). Your study has been assigned study protocol code **USM/JEPeM/22060378**, which should be used for all communications to JEPeM-USM in relation to this study. This ethical approval is valid from **5th December 2022** until **4th December 2023.**

Study Site: Biomedical Laboratory, Universiti Teknologi MARA, Cawangan Pulau Pinang and Hospital Universiti Sains Malaysia.

The following researchers are also involved in this study:

1. Assoc. Prof. Dr. Mohd Ezane Aziz
2. Ir. Dr. Nor Salwa Binti Damanhuri
3. Dr. Belinda Chong Chiew Meng
4. Dr. Afaf Rozan Binti Mohd Radzol
5. Assoc. Prof. Dr. Khoo Bee Ee

The following documents have been approved for use in the study.

1. Research Proposal

The list of JEPeM-USM members present during the full board meeting reviewing your protocol is attached.

While the study is in progress, we request you to submit to us the following documents:

1. Application for renewal of ethical approval 60 days before the expiration date of this approval through submission of **JEPeM-USM FORM 3(B) 2019: Continuing Review Application Form.**
2. Any changes in the protocol, especially those that may adversely affect the safety of the participants during the conduct of the trial including changes in personnel, must be submitted or reported using **JEPeM-USM FORM 3(A) 2019: Study Protocol Amendment Submission Form.**
3. Revisions in the informed consent form using the **JEPeM-USM FORM 3(A) 2019: Study Protocol Amendment Submission Form.**
4. Reports of adverse events including from other study sites (national, international) using the **JEPeM-USM FORM 3(G) 2019: Adverse Events Report.**
5. Notice of early termination of the study and reasons for such using **JEPeM-USM FORM 3(E) 2019.**
6. Any event which may have ethical significance.

JEPeM
JAWATANKUASA ETIKA PENYELIDIKAN MANUSIA

7. Any information which is needed by the JEPeM-USM to do ongoing review.
8. Notice of time of completion of the study using **JEPeM-USM FORM 3(C) 2019: Final Report Form.**

Please note that forms may be downloaded from the JEPeM-USM website: **www.jepem.kk.usm.my**

JEPeM-USM is in compliance with the Declaration of Helsinki, International Conference on Harmonization (ICH) Guidelines, Good Clinical Practice (GCP) Standards, Council for International Organizations of Medical Sciences (CIOMS) Guidelines, World Health Organization (WHO) Standards and Operational Guidance for Ethics Review of Health-Related Research and Surveying and Evaluating Ethical Review Practices, EC/IRB Standard Operating Procedures (SOPs), and Local Regulations and Standards in Ethical Review.

Thank you.

"WAWASAN KEMAKMURAN BERSAMA 2030"

"BERKHIDMAT UNTUK NEGARA"

Sincerely,

ASSOC. PROF. DR. NAZRI MUSTAFFA
Deputy Chairperson
Jawatankuasa Etika Penyelidikan (Manusia) JEPeM
Universiti Sains Malaysia

AUTHOR'S PROFILE

Mohamad Haizan Othman obtained his Bachelor of Engineering (Hons.) in Electrical and Electronic in 2021 from University Technology Mara Permatang Pauh Branch, Penang. His final year project focused on developing an automated system for water quality monitoring in the prawn industry using LabView and IoT technology. His interest in biomedical imaging and image processing has grown through his postgraduate research, aiming to contribute innovative solutions that improve medical diagnostics and healthcare outcomes.

LIST OF JOURNAL PUBLICATION:

1. **Othman, M. H**., Meng, B. C. C., Damanhuri, N. S., Aziz, M. E., & Othman, N. A. (2024). Automated Inhomogeneity Correction and Fat Extraction in T1-weighted MRI of Long Bones: An Adaptive Disk Structure Element Morphological (ADSEM) Approach for Improved Osteosarcoma Diagnosis and Analysis. *International Journal of Intelligent Engineering & Systems*, *17*(1).
2. M. S. Muhammad Shukor, Belinda Chong Chiew Meng, N. S. Damanhuri, N. A. Othman, **M. H. Othman**, and M. E. Aziz, "MRI T1-Weighted Fat Segmentation Based on Active Contour for Osteosarcoma Patients", *J. Adv. Res. Appl. Sci. Eng. Tech.*, vol. 49, no. 2, pp. 1–14, Aug. 2024.

LIST OF PROCEEDING PUBLICATION:

1. **Othman, M. H**., Meng, B. C. C., Damanhuri, N. S., Aziz, M. E., & Othman, N. A. (2022, October). MRI Thigh Sequences in Determining the Tumor Size Using Fuzzy C-Means for Patients with Osteosarcoma. In *2022 IEEE 12th International Conference on Control System, Computing and Engineering (ICCSCE)* (pp. 125-130). IEEE.
2. Rusli, A. H. T., Meng, B. C. C., Damanhuri, N. S., Othman, N. A., **Othman, M. H**., & Zaidi, W. F. A. W. (2022, October). Potato leaf disease classification using image processing and artificial neural network. In *2022 IEEE 12th International Conference on Control System, Computing and Engineering (ICCSCE)* (pp. 107-112). IEEE.
3. Damanhuri, N. S., **Othman, M. H**., Othman, N. A., Meng, B. C. C., Abdullah, M. H., & Salleh, N. A. M. (2024). Automated System of Water Quality Monitoring for Prawn Industry via Labview And Internet of Things. *International Journal of Intelligent Engineering & Systems*, *17*(3).

LIST OF COPYRIGHT:

1. Automated Tumor Necrosis Assessment Method for MRI Osteosarcoma Patients, 12 April 2023.

LIST OF AWARDS:

1. Penang International Invention, Innovation and Design (PIID) 2023 for Automatic Muscle and Fat Segmentation in the Thigh for T1 Weighted MRI for Osteosarcoma Patients – Silver award.

LAMPIRAN

BIL	JUDUL BAHAN
1	MULTILEVEL THRESHOLDING FUZZY C-MEANS (MTFCM) HYBRID METHOD FOR OSTEOSARCOMA NECROSIS EXTRACTION IN MAGNETIC RESONANCE IMAGING